Simulation of Radiation Driven Instabilities

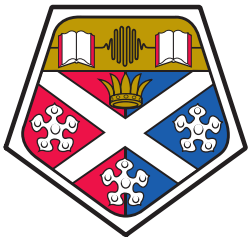

University of Strathclyde

David McLellan

2024

For my late wife, Emma, you gave me inspiration and direction to make the most of every day, my son Ewan, I'm very proud, thank you for supporting student dad. My parents John and Morag, I've always been supported to take opportunities and do my best and my sister, Julie for generosity of spirit and making sure everyones always ok and all of you for making sure there's plenty of fun times along the way.

I would like to acknowledge my supervisor, Dr Gordon Robb, for having no issue in taking on my various peculiarities as a PhD student; a 20 year gap in academic career, a switch from experimental to theoretical postgraduate physics, a rare part-time arrangement and limited programming experience at the start of this endeavour. It was a pleasure and education to work with EQOP, CNQO and Strathclyde Physics as well as working with ColOpt colleagues in the University of Milan and Université de Côte D'Azur. I thought there was a possibility of achieving a postgrad qualification as I tried to encourage and enable those with that ambition in my time as a high school teacher. I am delighted to have been enabled and supported in that ambition myself.

This thesis is the result of the author's original research. It has been composed by the author and has not been previously submitted for examination which has led to the award of a degree.

Signed: 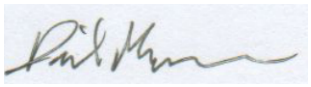

Date: 14 October 2024

Abstract

This research seeks to extend the understanding of optomechanical collective effects particularly using modelling based on coherent scattering of light by cold atoms in free space. We develop a microscopic model and use simulations where we will vary the properties of the pump field including the use of structured light and bandwidth modulation looking for distinctive behaviours in measurable outputs. Modelling is developed based on a weak classical input light field and multiple two level atomic states with minimal population of the excited states. Firstly we will seek to build and validate a model based on coupled dipole theory with stationary atoms in regimes where we would expect to see established collective effects such as superradiance.

We will then look to couple equations of motion based on cooperative optomechanical forces such that we incorporate centre of mass motion into our modelling. We can proceed to investigate established cooperative effects such as Collective Atomic Recoil Lasing, (CARL) and optical binding and extend our understanding of these by adding to existing models or varying key parameters of the cold atomic cloud or pump field. An investigation of optical binding of multiple cold atoms using our model is presented. Our results show the existence of stable and metastable configurations of atoms, and the occurrence of regular 'breathing' in a 2D atomic lattice due to optical forces arising from cooperative scattering.

As well as the familiar homogeneous plane wave fixed frequency light we will be considering orbital angular momentum in our pump field and looking to use modulated partially coherent pump fields more consistent with broadband signals found in nature.

Firstly we focus on CARL where previous work has been generally focused on pattern formation due to mutual light field, atomic cloud interaction involving linear momentum transfer. We look to investigate similar pattern formation or 'bunching' specifically resulting from orbital angular momentum (OAM) in chapter 4.We find that the light-matter coupling allows for the superradiant transfer of the atoms between the discrete OAM states. Tuning the ring parameters and the azimuthal mode number of the pump light, specific angular momentum states can be populated. Further to this we go on to investigate the effects of amplitude modulation of the light field signal with a view to extending the frequency range of the light field and extend prior work indicating enhancement of cooperative effects in the case of phase modulation in the case of CARL in chapter 5. We successfully demonstrate enhancement of measurable cooperative effects in our case corresponding to the resulting temperature increase in the atomic cloud.

Nobody ever figures out what life is all about, and it doesn't matter. Explore the world. Nearly everything is really interesting if you go into it deeply enough.

— Richard P. Feynman

Contents

1 Introduction

1.1 Light Matter Interactions

One of the earliest recorded examples of evidence of forces associated with light fields was the observation that a comet's tail always points away from the sun as a result of observations by Johannes Kepler in the seventeenth century. Further work to demonstrate these anticipated interaction forces consistent with Maxwells electromagnetic theory of light were published in the early twentieth century by Nichols et al. [1] and Lebedev [2]. The forces considered were extremely small and it was not until the development of the laser that available intensity gradients allowed the investigation of the acceleration and trapping of particles under strong light fields particularly progressing with work such as Ashkin's in the 1970s [3]. The following sections in the introduction will be used to give an overview of relevant phenomena in this field concerning scattering, optical forces and cooperative effects.

1.1.1 Scattering

In this work we consider semi-classical model of the light-matter interaction, where the internal atomic dynamics (coherence, population) is described quantum mechanically or microscopically, but the optical fields and the atomic centre-of-mass motion are described classically or in macroscopic terms.

The process of scattering of electromagnetic radiation (which we shall refer to as light generally) by matter is fundamental to this research and will be described further in

this section. The scattering of light results in the dispersion of modes in the incoming light field into other available modes potentially in different directions in an elastic or inelastic interaction.

The majority of early studies of light transport and scattering in the natural world dating from the early 20th century [4] considered a dense environment of scatterers. These environments can be considered as multiple scattering regimes, in which case the light field progressing through such a distribution would tend to be incoherent and follow a diffusive path. We will generally consider a coherent single scattering regime in this work, however, several useful general concepts in light matter interaction will be described further here and in section 1.2.

In response to a light field matter can display optical polarisation, $\mathbf{P}$ in terms of constituent charged particles responding to an electric field, $\mathbf{E}$, resulting in a transient polarisation effect proportional to the size of the field and the susceptibility of the material, $\chi^{(n)}(\omega)$, which is related to the refractive index, n, as discussed in section 1.2 . For example when subject to electromagnetic radiation different types of matter which could include clouds of atoms will generally have an inherent polarisability,

$$\mathbf{P} = \varepsilon_0\Big(\chi^{(1)}(\omega)\mathbf{E} + \chi^{(2)}(\omega)\mathbf{E}^2 + \chi^{(3)}(\omega)\mathbf{E}^3 + ...\Big), \tag{1.1}$$

where ε_0 is the vacuum permettivity.

When we refer to linear optics the polarisation effect responds linearly to the electric field of the light involving only the first order term of the susceptibility tensor. It is only for very high intensities of electric field (where the electric field strength is

comparable to the atomic electric fields) that higher order terms become significant and related non-linear optical responses will occur introducing new and harmonic frequency responses.

1.2 Transport of Light Through Atomic Media

We will consider a plane wave monochromatic light field interacting with a simple 2 level atom. We will assign wavenumber, k to this field and introduce the detuning, $\Delta_0 = \omega_0 - \omega_a$ which is the frequency difference between the light field, ω_0 and the resonant 2 level atomic transition, ω_a. We will add some detail to the description of the transport of light through a multiple scattering environment which will introduce some useful concepts. We can consider a macroscopic model taking into account wavelength and phase dependency. If we consider the complex susceptibility $\chi(\omega)$ [5] which will be familiar from the common formula for the refractive index of a homogeneous medium, $n^2(\omega) = 1 + \chi(\omega)$. This describes a measure of the dephasing of a wavefront across a given medium, considering the length of travel across the medium, L, the induced phase shift, $\phi(\omega)$, and transmitted intensity, $T(\omega)$, will be [6],

$$\phi(\omega) = \mathrm{Re}(\chi(\omega))kL/2, \tag{1.2}$$

$$T(\omega) = \exp[-\mathrm{Im}(\chi(\omega))kL]. \tag{1.3}$$

Equation 1.3 is often referred to as the Beer-Lambert law describing optical field at-

tenuation. This provides a variable we will make further use of, the optical thickness, b, which corresponds to the negative of the argument of the exponential in equation 1.3, which in the case of considering an atomic distribution of atomic dipoles with an interaction cross section of $\sigma_{sc}(\Delta_0)$,

$$\mathrm{b}(\omega) = \mathrm{Im}(\chi(\omega)kL) = \mathrm{N}\sigma_{sc}(\Delta_0)L, \tag{1.4}$$

[7] where N is the atomic density. The scattering cross section, σ_{sc} at detuning, Δ_0 is related to the resonance cross section, σ_0, by,

$$\sigma_{sc}(\Delta_0) = \frac{\sigma_0}{1 + 4\Delta_0^2/\Gamma^2}. \tag{1.5}$$

It is worth confirming as implied by equation 1.5 that the optical thickness also diminishes rapidly with increasing Δ_0 by an inverse square relationship (where detuning is increased to values much larger than the linewidth) as follows,

$$\mathrm{b}(\Delta_0) = \frac{\mathrm{b}_0}{1 + 4\Delta_0^2/\Gamma^2}. \tag{1.6}$$

The optical thickness is clearly important in terms of the nature of the scattering interaction between a pump field and a medium and is commonly referred to in cold atom research around cooperative effects. If we use the approximation $\sigma_0 \approx 1/k^2$ the resonant optical thickness, b_0, following from equation 1.4 can be given as,

$$\mathrm{b}_0 \approx \frac{N}{(k\mathrm{R})^2}, \tag{1.7}$$

where N is the number of atoms, which is commonly used, though there may be a difference of a factor of 3 depending on whether the scalar or vectorial model is being considered which is further described in section 1.6. The relevance of the optical thickness, $\mathrm{b}(\Delta_0)$ and the quantitative dependency on it for our simulations are explained along with other assumptions in section 2.1.

1.3 Single Scattering

When we refer to a single scattering environment this can be understood as the most likely outcome being a single scattering event for each wavefront that passes through a distribution. This has implications for our model and related assumptions discussed here which we will elaborate on in 2.1. A dilute distribution of particles will provide such an environment and is representative of the cold atom clouds we will base the modelling on in this research. We consider the atoms as point scatterers consistent with Rayleigh scattering [8], where particles are much smaller than the wavelength of the light field. The frequency of the light field will determine the interaction strength, therefore the scattering length determining the likely distance between scattering events and whether we have a single or multiple scattering environment. The interaction strength depends on the light field frequency relative to resonances where there is a permanent or induced dipole moment for atomic scatterers. The interaction can be elastic or inelastic depending on whether the frequency of the scattered light field is the same as the incoming field or whether there has been

some removal of electromagnetic energy into non-radiative states. Where Rayleigh scattering events occur independently for an unpolarised light field this results in isotropic scattering (we will discuss examples of cooperative effects in the next section 1.5.

For comparison where the scattering particle is on the scale of the light field wavelength, this is known as the Mie [9] scattering regime, for the example of a uniform spherical scatterer the intensity of the scattered light field would be anisotropic usually favouring forward and backward scattering as shown in figure 1.1.

In the case where a scattering particle is much larger than the wavelength of the light field, this would usually be described as geometrical optics. Therefore the standard macroscopic laws of reflection and refraction as described in [10] would be sufficient to describe the resulting intensity and direction of the light field for such interactions.

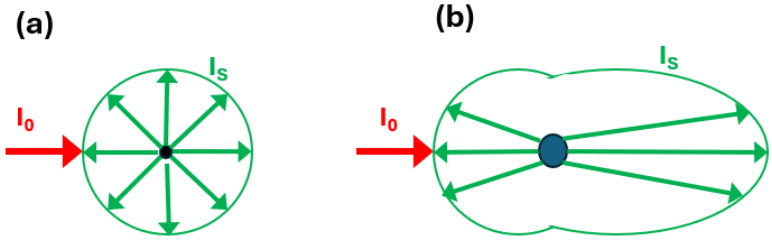

Figure 1.1: Incoming light field with intensity I_0 and scattered light field intensity indicated by size of arrows shown for (a) point scatterer (Rayleigh scattering) and (b) wavelength scale uniform scatterer (Mie scattering)

1.4 Optical Forces

Returning to our plane wave monochromatic light field interacting with a simple 2 level atom we can give an overview of the principles involved in light induced forces used in the course of this research. We have introduced optical polarisation, **P** and susceptibility, $\chi^{(n)}(\omega)$. At a low density of atoms which we will define in relation to the light field wavelength as $\mathrm{N}k^{-3} < 1$, where the susceptibility is related to the individual atomic polarisability, $\alpha(\omega)$ by $\chi^{(1)}(\omega) = \mathrm{N}\alpha(\omega)$ [6]. We also work within a regime of a linear first order polarisation response to the light field (the criteria for which will be described further in 2.1). We can now consider the individual dynamic atomic response to the light field in terms of the induced dipole moment which we will label, **d**, where, $\mathbf{d} = \alpha(\omega)\mathbf{E}$.

Now we can define the dynamic interaction between the light field and the induced dipole responsible for the optically induced forces we are interested in. Where we have 2 level atoms in a light field with a small detuning compared to the transition frequency this interaction potential is responsible for mixing of the 2 states of the 2 level atom in terms of populations and atomic coherences with a dependency on the Rabi frequency, Ω_0 which represents the oscillation rate between ground and excited states in a 2 level atom in a constant monochromatic light field. The Rabi frequency plays an important role in the Couple Dipole Model (CDM) described in section 1.6, is introduced further in our boundary conditions and assumptions 2.1 and is key to our model development in section 2.2.

The induced dipole single atom interaction potential can be described as [11],

$$U_{diplole} = -\frac{1}{2}\langle \mathbf{d} \cdot \mathbf{E} \rangle = -\frac{1}{2\epsilon_0 c}\mathrm{Re}[\alpha(\omega)]I, \tag{1.8}$$

where the angular brackets here and throughout represent a time average, we are considering the real part of the complex atomic polarisability and I is the light field intensity which we define as, $I = \epsilon_0 c|\mathbf{E}|^2/2$. The real component of the polarisability is associated with the dispersive part of the interaction also known as the in-phase dipole oscillation. Whereas the imaginary part is associated with the absorptive part of the interaction also referred to as the out-of-phase dipole oscillation.

We can see from equation 1.8 that potential gradients and thus optical forces due to the light field interaction with a single neutral atom (with a frequency dependent polarisibility) are possible where there are variations in the light field intensity. For example where we have a coherent light field in a single scattering environment producing interference patterns.

Therefore the resulting dipole force is,

$$\mathbf{F}_{diplole} = -\nabla U_{diplole}. \tag{1.9}$$

For our single atom model in a monochromatic light field there is another distinct interaction force known as the scattering force or radiation pressure. This is the principle force used in laser cooling or optical molasses which is defined in detail in [12].

We will use a simplified explanation here, we will assume the light field is of a res-

onant frequency with the 2 level atom (or close to resonance as there is a natural linewidth related to the power absorption or emission from a given oscillating dipole or our 2 level atom). There will be absorption and spontaneous emission of photons described by the familiar Einstein A and B coefficients for absorption and spontaneous emission, these concepts are explained in further detail in [13].

The atom will experience a recoil momentum change in the absorption process and later a second momentum kick in the emission process. Each absorbed photon gives the atom a kick in the direction of the light field and the spontaneously emitted photons will give a kick in a random direction for each absorption. We will consider that over many absorption emission sequences that the second momentum kick in each cycle averages to zero (resulting in slowed atoms exhibiting a diffusive motion pattern similar to Brownian motion [14]). This infers that the resulting force experienced by the atom will be a product of the photon momentum, $\hbar k$ (where we again have wavenumber k assigned to the light field) and the photon scattering rate, $\Gamma_{scatter}$ equating to one cycle of photon absorption and emission.

$$\mathbf{F}_{scatter} = \hbar \mathbf{k} \Gamma_{Scatter}. \tag{1.10}$$

The relative scaling of the dipole force, the scattering force, the detuning and the Rabi frequency is an important consideration with regards to observing cooperative phenomena in different regimes. There is further explanation of this and a full derivation in section 4.1 with equation 4.6 indicating the relative scaling of optical forces in particular with detuning. This will be relevant in the parameter choices made in relation to particular phenomena where the relative proportion of these

forces is important. In summary the key relationships are,

$$|\mathbf{F}_{dipole}| \propto \frac{I}{\Delta_0}, \tag{1.11}$$

$$|\mathbf{F}_{scatter}| \propto \frac{I}{\Delta_0^2}. \tag{1.12}$$

1.5 Cooperative Effects

In the natural world there are various fascinating examples of unexpected and often awe inspiring group behaviours with a large collection of interacting individual elements showing pattern formation or self-synchronisation due to driven interactions between neighbouring individuals. This reinforcement of large scale observable coordination within groups can be seen in ripples in the sand or dune formation in the desert, large scale murmurations in flocks of starlings or regular light patterns evolving from initially random individual flashing from large groups of fireflies [15].

Relevant to this research we will focus on the example of the scattering of a light field by a cloud of cold atoms, the mechanics of this interaction are described earlier in this section, here we will consider the intensity distribution of the scattered light field. Where we have a coherent light field and we are in a single scattering regime detailed further in 1.1.1 and 2.1, there is the possibility of interactions between individual scatterers leading to observable cooperative effects.

The definition of cooperativity itself in this particular scenario is worthwhile here, a

good starting point is the position that the term cooperativity should be 'reserved for effects that could not be explained by the mean field approach of traditional optics' [16]. This can be demonstrated using the coupled dipole model, (CDM), to calculate the mutual evolution of the atomic distribution and resultant field properties (calculation of which is detailed further in section 1.6).

In order to help with this definition there are experimental observables that are generally extensive, i.e. that increase proportionally with the number of atoms, the amount of scattered light in a multiple scattering regime would fall into this category. There are also intensive observables for our cloud of atoms which are generally independent of the number of atoms which would be the case for susceptibility, $\chi^{(n)}(\omega)$ 1.1.1. It is useful to make the assertion that if an extensive property under certain conditions is no longer proportional to the number of atoms or if an intensive property became dependent on the number of atoms (in reproducible circumstances with the same findings for repeated observations), then consistent with other research in the field [6] we would take this as a good indication of cooperative effects being responsible.

Where there is no interaction or a weak interaction between individual scatterers in simple terms the scattered light field intensity will be proportional to the number of scatterers. However in the case of a strong interaction in a similar fashion to the examples from nature described above there can be correlation in the scattered field due to evolving synchronisation of coherent scattering. A significant result in this case is that the scattered field intensity can evolve in proportion to the number of scatterers with a power law larger than one.

Several terms exist describing this phenomena for which we will give a brief overview

here. Where we have a scattered intensity distribution showing an intensity pattern favouring particular directions with a relationship of, $I_{scatter} \propto N^{\gamma}$, where $\gamma > 1$, this is generally termed superradiance [17]. Where a cloud of independently excited cold 2 level atoms emit radiation due to relaxation to the ground state a collective evolution to cooperative enhanced emission patterns as described can be observed, in this case labelled as superfluorescence by Bonifacio [18]. Where a probe field propagates through a gain medium which has not reached the threshold for amplification by stimulated emission required for lasing, conditions for superradiant intensity profiles also occur and in these circumstances this is labelled amplified spontaneous emission [19].

1.5.1 Superradiance, Subradiance and the Collective Lamb Shift

We will return to the particular case of the cooperative scattering of a light field by a cloud of cold 2 level atoms resulting in superradiant behaviour as described in the previous section. Additionally considering areas of lower intensity scattered field in particular directions due to cooperatively induced reduced scattering rate known as subradiance [20] and cooperative resonance shifts also known as the collective Lamb shift [21] in the linear optics regime. We will take a closer look at the nature of these phenomena which have generated more interest in recent years with the study of different varying densities, materials, geometries and weak fields approaching single quanta of energy interaction regimes termed as single photon superradiance [22].

Initial studies by Dicke [23] suggested that cooperative effects in special cases of light matter interaction such as superradiance would only occur with clouds of atoms on a scale of a wavelength or less where $\mathrm{N}k^{-3} \gg 1$, again using the atomic density,

N and radiation field wavenumber of k. In recent years it has been established theoretically and experimentally that the weak field regime (further defined in section 2.1) allows for the study of coherent cooperative effects in dilute larger cold atom clouds. Significantly this provides more opportunity for experimentally reproducible modelling [24].

Superradiance emerging from a cloud of strongly coupled cold atoms will result in absorbed light being emitted in a shorter timescale and hence a higher intensity than it would be based on the standard spontaneous emission time of a single atom. This is a coherent light mediated effect with a dependency on the relative positions of atoms within the cloud, resulting in a collective decay rate, $\Gamma_{Cooperative}$ [25]. This has a dependence on the optical thickness, b(Δ_0) and a geometry dependent numerical structure factor in the order of 1 that we shall label, ζ_{Shape},

$$\Gamma_{Cooperative} = \zeta_{Shape}\frac{N}{(k\mathrm{R})^2}\Gamma, \tag{1.13}$$

where N is again the number of atoms for a distribution approximating to a 2 dimensional profile of R^2 in the dimensions transverse to the light field propagation direction. In optimal conditions for superradiance revealed by experimental results [26] this corresponds to $\gamma = 2$, for $I_{scatter} \propto \mathrm{N}^{\gamma}$ and values of $\Gamma_{Cooperative} \approxeq 2.5\Gamma$.

It is perhaps helpful to also consider the scattering rate in terms used in 1.4 in terms of dipole interaction potential and atomic polarisibility. In this case we can define the scattering rate to be the power absorbed by the atom divided by the energy of an emitted photon which would give us,

$$\Gamma_{Scatter} = \frac{\langle \dot{\mathbf{d}} \cdot \mathbf{E} \rangle}{\hbar \omega_a} = \frac{1}{\hbar \epsilon_0 c} \mathrm{Im}[\alpha(\omega)] I. \tag{1.14}$$

We can see that the very nature of the strong field-dipole and dipole-dipole interactions consistent with the described nature of cooperative effects can in this case lead to the development of a macroscopic dipole response. If we look at equation 1.14 we can see that the individual induced dipole term will be subject to the development of the macroscopic dipole response resulting in deviation from the standard single atom values.

Subradiance is a coherent cooperative effect which can be considered as a result of destructive interference. Due to the related extended time taken for scattered radiation to propagate from a distribution it can be easily confused with a simpler radiation trapping effect in a multiple scattering regime. Again taking into consideration the induced dipole response of the atoms to the light field there are cases where dipoles will be oscillating in-phase with each other corresponding with a superradiant response and there will also be cases where dipole are oscillating out of phase with each other leading to a subradiant response. Investigation of these states has proven difficult experimentally [20] due to these states being very fragile and potentially being disrupted by various non-radiative decay mechanisms.

We will make use of the Dicke model [27] which considers cold atomic cloud samples which are less than a wavelength of the light field. In-phase symmetric superposition of induced dipole states results in superradiant behaviour and out-of-phase antisymmetric superpositions of such states correspond to subradiant behaviour.

In spite of the difficulties subradiant behaviour has been observed experimentally in

line with the Dicke model for 2 ions [28] and a subradiant decay rate in one radiation mode for $N \gg 2$ atoms [29].

We now know as a result of this and further research that in the dilute larger scale environment in the case of $N \gg 2$ atoms long range dipole-dipole interactions will induce superradiant and subradiant effects. It has also been found that collective states due to long range interaction can be suppressed by short range interactions [30]. Therefore in a departure from the small and dense atomic cloud geometry of Dicke's original study but using the model concepts and later results, a large and dilute atomic sample would be more favourable for the observation of the described subradiant states.

Returning to the collective lamb shift whereby an observable shift can be observed from the single atom transition frequency due to a cooperative contribution to the Lamb shift. This effect which occurs under the same conditions as superradiance and subradiance, first theorised by Lamb [31] is described as an energy shift to the transition atomic levels related to interaction between the atom and vacuum electromagnetic field modes. Again due to coherent dipole dipole interaction there is a cooperative contribution which can be identified using the CDM which will be described in detail in following sections. The resultant collective dipole response of the atomic cloud has a real component describing the cumulative cooperative decay rate and an imaginary cumulative term describing the cooperative Lamb shift which will be described in section 2.2 with reference to equation 2.13.

1.6 The Coupled Dipole Model (CDM) with Stationary Atoms

Our area of interest requires a representation of a cold atomic distribution in a weak coherent homogeneous pump field. It would be helpful here to illustrate a simplified model of an electromagnetic coherent pump field interacting with a distribution of cold atoms which for our purposes represent point dipoles this is shown in figure 1.2. This will enable modelling effects taking account of the scattered radiation field and coupled forces acting on the atomic ensemble. Classical analogies have been developed [32] with a view to deriving a set of coupled differential equations for the time development of atomic dipole amplitudes (atomic coherences, generally referred to as β) equivalent to those established via a fully quantum model which will be developed in chapter 2.

For our atomic cloud we have a system of N two level atoms (treated as point dipoles in our modelling) with amplitude β_j, position r_j, initial condition $\beta_j(0) = 0$ and spontaneous decay rate, Γ or linewidth of the atomic transition, where ω_a again represents the atomic transition frequency. $\mathbf{k_0}$ is the pump field wave vector and $k_0 = 2\pi/\lambda_0$ is the wavenumber. It is important to point out that this methodology is representative of a scalar model of interaction which is valid for our simulations following assumptions described in 2.1. This means that polarisation characteristics of the field are ignored and near field dipole-dipole interaction terms are ignored which with our assumptions 2.1 do not have a material effect on the measurable outcomes we are looking to explore further. At this point we are considering a cloud of stationary cold atoms from which our microscopic model will be able to provide data which can be used to determine scattered field profile and related information

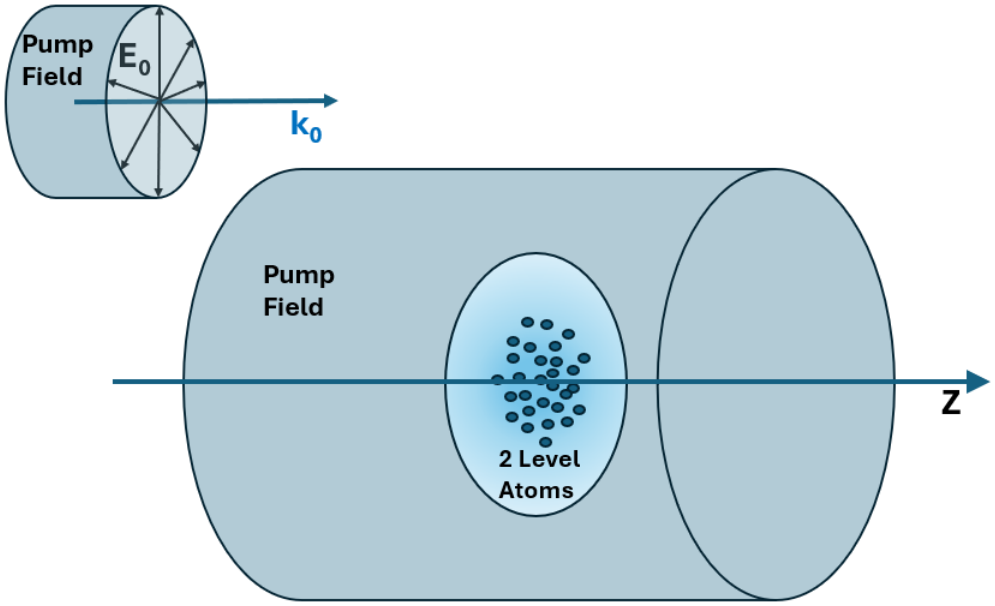

Figure 1.2: Simplified diagram of pump field aligned along Z axis, unpolarised in the transverse XY plane, interacting with a cold atom distribution which can be 2D or 3D.

about collective state lifetime of the scattered field.

1.7 Collective Atomic Recoil Lasing (CARL) and Cooperative Centre of Mass Motion

Collective Atomic Recoil Lasing (CARL) was based on theory developed by Bonifacio et al. [33]. This is an opto-mechanical phenomena based on collective effects in cold atomic systems. This is described by simultaneous evolution with mutual feedback of optical fields and density of the atomic distribution. The initial model for CARL

was based on a strong optical pump field interacting with a cloud of 2 level cold atoms, resulting in a scattered field usually in a direction influenced by available cavity mode directions or potentially geometry of the distribution. Where the atomic cloud has a principle axis similar to a 3D cigar shape or a 2D ellipse the scattering modes along this axis will dominate as has been demonstrated experimentally using a Bose-Einstein condensate showing the emergence of 'end-fire' modes [34].

In the case of a typical cavity example of CARL the scattered field is counter-propagating to the pump field. Initially this field corresponds to Rayleigh scattering from individual atoms, where we have long coherence time or enhanced interaction time e.g. within a cavity there will be interference between pump and backscattered or probe field creating a varying potential field. Where there is a potential gradient cold atoms are displaced to locations of minimum interaction potential which results in a grating effect of atomic distribution corresponding with a period of half the wavelength of the pump field as shown in figure 1.4.

The theory has since been confirmed experimentally [35] and further investigations involve for example multimode CARL in free space [36]. A feature fundamental to CARL is the preferred direction of the scattered field which can be influenced by the shape of the atomic distribution particularly if there is a principal axis or by available modes in a cavity. At a microscopic level the exchange of linear momentum between the pump field and atomic distribution also leads to atomic grouping in momentum space due to preferred scattering direction which will be revisited in later sections considering CARL involving the exchange of orbital angular momentum with the pump field rather than linear momentum.

We will need to extend our model to incorporate atomic centre of mass motion

based on the optical forces described in 1.4 in order to model bound states, pattern formation and CARL in different regimes.

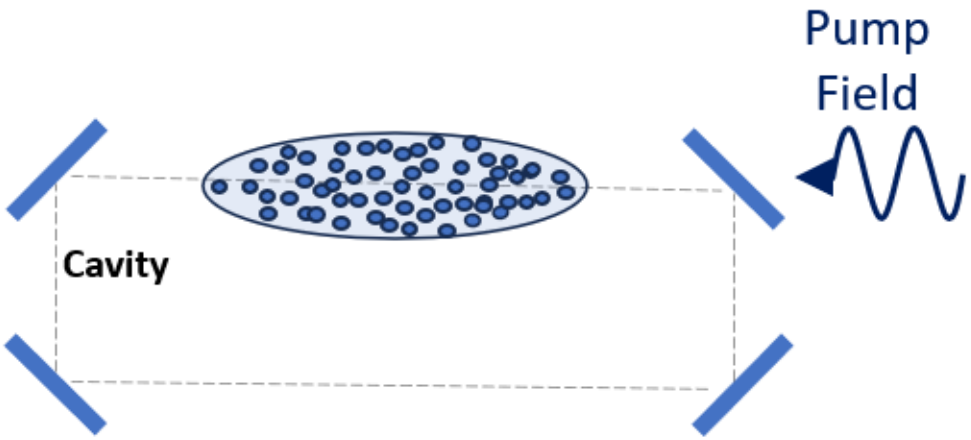

Figure 1.3: CARL evolution initial state at t=0 showing pump and initially random 2D elliptical distributed cloud of atoms.

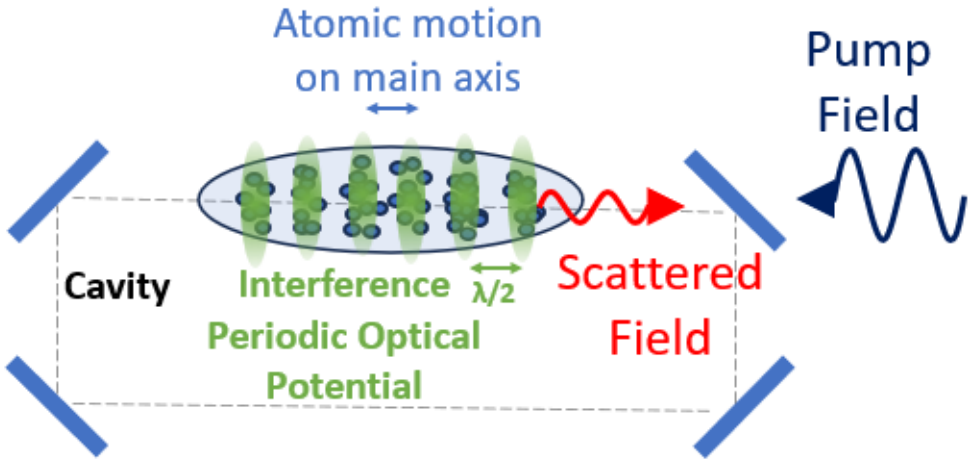

Figure 1.4: CARL evolution at t>0 showing pump, probe (scattered) field and resulting pattern from atomic motion induced by CARL. The initially random 2D elliptical distributed cloud of atoms tends towards the grating formation corresponding to resultant optical field interference giving rise to potential gradients.

1.8 Cold Atom Physics in Relation to Broadband and Astrophysical Phenomena

Experimental studies of interactions involving light and atomic gases are usually relatively modest in scale, typically involving gases with dimensions in the regions of mm to cm. However features of these interactions occur on much lager spatial scales in astrophysical situations. An example of this is the similarity in character of a cloud of cold atoms scattering a light field in a magneto-optical trap (MOT) commonly used in cold-atom experiments and a star. Although vastly different in size, both rely on a balance between radiation pressure forces and opposing, compressing forces. In the MOT, the compressing force is produced by the magnetic trap, whereas in the star the compressing force is produced by gravitational attraction.

Laboratory analogues of astrophysical radiative phenomena have been proposed e.g. "photon bubbles". Photon bubbles in astrophysics arise when a stellar atmosphere with uniform luminosity across its surface becomes unstable. The result of this instability is a stellar surface with highly non-uniform density and non-uniform luminosity. Laboratory analogues of similar instabilities have been predicted by Mendonca et al [37] and experimentally observed by Giampaoli et al [38].

Another example of interactions with relevance to astrophysics are those involving broadband or thermal radiation sources which can also be described as blackbody radiation. In astrophysics, such sources are far more common than coherent, laser-like radiation. Theoretical studies by Sonnleitner et al [39] have predicted that a body emitting blackbody radiation can exert an attractive force on a nearby mass, and that this attractive force can dominate the force of gravitational attraction. The

existence of this temperature and spatially dependent attractive force was confirmed experimentally by Haslinger et al [40] using Caesium atoms detecting this force with atomic interferometry.

Again in the stellar example huge light field intensities are considered in order to have a significant impact on the surrounding high energy particles. This is more consistent with a multiple scattering regime the conditions for which are described earlier in the Introduction and further within model assumptions 2.1. In this non-coherent regime at larger optical thickness it is possible to investigate the coupling of field intensity to density in cold atom fields with a view to observing similar oscillations and structures as to those described in the stellar regime. Without going into detail the multiple scattering environment can be described by diffusion equations similar to energy transport via Brownian motion [14]. For areas of high electromagnetic radiation intensity the multiple scattering sometimes also referred to as radiation trapping can be considered to generate a coulomb like repulsive force on the atomic media which has previously been demonstrated experimentally [41].

We think these examples show mechanisms by which there can be a reasonable comparison between effects observed using cold atom physics and larger scale natural and astrophysical phenomena with thermal rather than monochromatic radiation.

1.9 Thesis outline

This thesis consists of six chapters. Following this introduction which serves to provide context, chapter 2 presents a technical overview of developing and validating our model considering signature cooperative effects from a stationary atomic cloud

using the Couple Dipole Model (CDM). In particular we describe the phenomena of superradiance using data generated from simulations to evaluate scattered field intensities. In chapter 3 we couple the model to centre of mass motion resulting from light matter interaction forces with a more detailed derivation of a microscopic model. This allows us to look at the phenomenon of optical binding [42] taking the opportunity extend the atom numbers involved. This is the basis for the code developed for our model used throughout [43].

Chapter 4 describes superradiant CARL considering a light field with Orbital Angular Momentum (OAM) [44] extending work done on CARL. This work also considered azimuthal pattern formation measured by optical magnetisation, M described further in 4.2.2 also described as bunching in cold atom distributions considering OAM transfer rather than with light fields solely carrying linear momentum. Further to this we took the opportunity to investigate if OAM could be transferred form a first trapped atomic ring using a plane wave pump field to a second trapped atomic ring.

Chapter 5 describes a model of interactions where the optical field is no longer perfectly coherent but instead is partially coherent. Enhancement of cooperative effects in particular cases under pump field modulation was investigated.

Chapter 6 summarises our results and conclusions with reference to opportunities to apply to current research and potential for extension and continuing development of ideas.

2 Cooperative Scattering of Light by a Gas of Stationary Atoms

In this chapter we describe cooperative effects in light matter interaction with theoretical and experimental precedent. We seek to construct a microscopic model to allow further investigation of light matter cooperative phenomena. We will derive a set of equations based on the CDM [45] from which we can determine behaviour of the scattered field and look for signature cooperative behaviours. We will also describe the required conditions and assumptions that are necessary or provide optimal conditions for these phenomena.

2.1 Boundary Conditions and Model Assumptions

Further to the introduction and initial description of light matter interactions and cooperative effects that we are interested in there are certain criteria applicable to both the light field and the atomic distribution which are required for the CDM regime. We will specify here particular assumptions that will be applied throughout this research to the fully cooperative model based on coupled dipole theory which we will use for running simulations. Where any additional parameters or slight variations to these conditions are applied that will be specified in the particular section concerned.

- The light field is considered to be monochromatic and time harmonic with negligible amplitude variation in the region in which the model operates.

- The atoms are considered to be point dipoles with thermal velocities v satisfying the frozen model approximation $k_0 v \ll \Gamma$, where Γ is the two level atom (dipole) transition linewidth.

- The model operates in the weak driving or low excitation regime. This is described where the saturation parameter, $s \ll 1$, where,

$$s = \frac{2\Omega_0^2}{(\Gamma^2 + 4\Delta_0^2)}. \tag{2.1}$$

  Where we introduce the Rabi term which has a determining factor on interaction strength, $\Omega_0(r) = \Omega_0 \exp\{i\mathbf{k_0} \cdot \mathbf{r_j}\}$, $\Omega_0 = dE_0/\hbar$. Using variables from figure 1.2 and consistent with treating atoms as point dipoles, d, the dipole interaction term would be the dipole matrix element for the 2 level atomic transition. In some cases the condition of $s \ll 1$ is considered comparable to a single excitation within the distribution which has been the assumption used in previous research into collective effects in the cold atom regime including single photon superradiance [22].

- Further from section 1.4 with the saturation parameter, s defined as above with further derivation we can rewrite the equations for the optical dipole and scattering forces as [46],

$$\mathbf{F}_{dipole} = -\frac{\hbar\Delta_0}{6}\frac{1}{1+s}\nabla s, \tag{2.2}$$

$$\mathbf{F}_{scatter} = \frac{\hbar \mathrm{k}_0 \Gamma}{6}\frac{s}{1+s}. \tag{2.3}$$

We can see from equation 2.3 that the scattering force will saturate as s increases which is not the case with the dipole force. Where $s \ll 1$ this is termed the 'weak field' regime in which the population of two level atom states can be considered to be in the ground state.

- The first Born approximation [47] is applied which in effect defines single scattering rather than multiple scattering per incident light field wavefront passing through a distribution. In view of the scattered field being weak in comparison to the incident field, the incident field is considered to be the same throughout the distribution.The single scattering regime can be considered the case where the saturation parameter condition 2.1, $s \ll 1$ is applied, and the optical thickness is small in the region of $\mathrm{b}(\Delta_0) \leq 10$.

- The Markovian approximation is applied. This considers system evolution in time frames much greater than photon interaction time with the cloud of atoms [48], therefore the dynamic evolution of the system depends only on its current state.

- The Rotating Wave approximation is appropriate in this regime where the incident field frequency is in a similar order of magnitude to the atomic transition frequency such that derived terms in the interaction Hamiltonian H_I with phase oscillation at a frequency of $(\omega_0 + \omega_a)$ are ignored and terms with phase oscillation at the detuning frequency of $\Delta_0 = (\omega_0 - \omega_a)$ are kept.

- It is assumed that the incident radiation field is scalar considering a single excitation state where the polarisation of the light field is not specified. This is relevant to the calculation of scattering cross section and optical thickness which are pertinent to field amplitude and intensity calculations.

- The scattering process is considered to be completely elastic, no frequency redistribution mechanisms are considered (no Raman, Brilliouin interactions or Doppler related shifts in absorbed or transmitted frequency for example).

- Our model assumes classical atomic motion and interaction models. This condition is met and maintained where the superradiant scattering rate is greater than the single atom recoil frequency [49]. The linear recoil frequency is, $\omega_r = \hbar k^2/2m$. This condition applies in cases of recoil resulting from both linear momentum and orbital angular momentum (OAM) which will be defined in section 4.2.1. We define a superradiant scattering rate, $\Gamma_{k'}$, into scattered mode, k', of,

$$\Gamma_{k'} = \frac{\Omega_0}{\Delta_0}\sqrt{\frac{\Gamma\omega_r N}{(k_0 \mathrm{R})^2}}, \tag{2.4}$$

- For the start of simulations unless indicated otherwise the initial atomic coherence values are $\beta_j(0) = 0$.

- The atomic coherences, β_j will relax to equilibrium in the timescale of Γ^{-1} which is negligible in comparison to the timescales of relative atomic motion for our models. This is generally referred to thoughout as the adiabatic approximation.

2.1.1 Experimental Values for Comparison with Simulation Assumptions

We will attempt to provide here some comparable values for the assumptions we have provided in terms of variables applied in experimentation with cold Rubidium atoms in a dilute single scattering interaction with the pump field.

The relevant values for an on resonant pump field for the D2 transition of ^{87}Rb atoms shown in figure 2.2 [50] are provided here.

The wavevector, $k_0 = 8.053\text{x}10^6\text{m}^{-1}$, the transition wavelength $\lambda_{D2} = 780.2\text{nm}$ and the transition linewidth $\Gamma = 6.065\text{x}10^6(\text{x}2\pi)\text{s}^{-1}$ [51].

For a theoretical 3D distribution of Rubidium atoms we might have N, the number of atoms being $1\text{x}10^6$ for a distribution with $k_0 R_{x,y} = 100$, considering $R_{x,y}$ to be the transverse dimension (considering a cigar type shape with the long axis along the Z axis for convenience) as shown in figure 2.1.

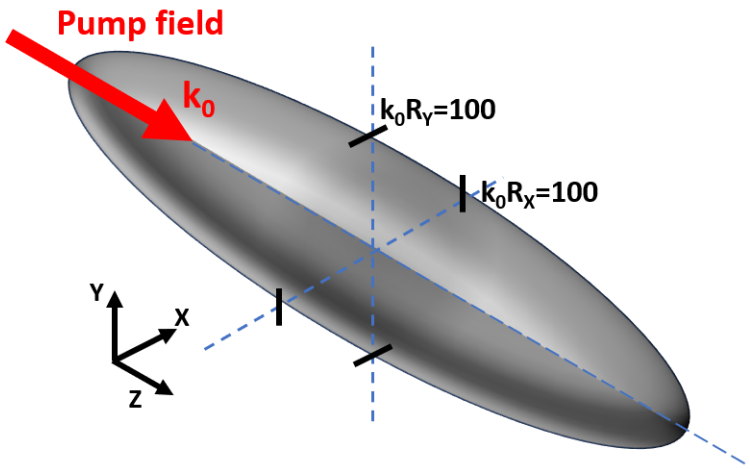

Figure 2.1: Ellipsoid 2 level atom 3D distribution.

This equates approximately to a resonant optical thickness, b_0 1.7 of around 100 for a major minor elliptical axes ratio of around 5. Where we introduce detuning and consider $b(\Delta_0)$ 1.6 this rapidly decreases to values below 1 for a detuning value

of 5 for example (we will use units of linewidth, Γ, throughout for Rabi term and detuning values of the pump field).

A pump field operating at $1.65\text{mW}cm^{-2}$ has been used in experimentation [52] representing a weak field near resonance appropriate for cooperative coherent scattering. This represents around 0.02 of the saturation intensity for the Rb D2 transition [52].

For simulations incorporating atomic motion considered here from chapter three 3. The 'slow' atomic motion model approximation is useful , $k_0 v \ll \Gamma$, with thermal velocities, v representing an rms value for velocity. We can then take temperature, $\text{T} = mv^2/2k_B$ considering 2 degrees of freedom in this case we can evaluate that we would be considering temperatures of much less than 100μK for our simulations or in equivalent experimental settings. For context the Doppler cooling limit is approximately 150μK with a theoretical recoil temperature of afew μK [53].

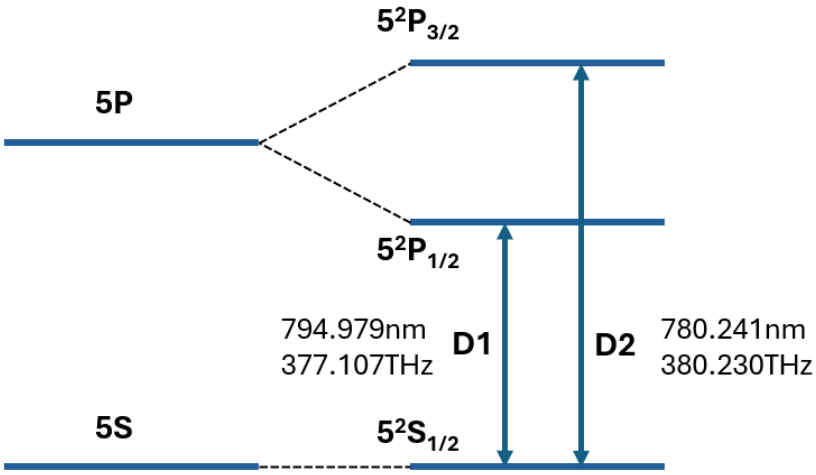

Figure 2.2: Diagram showing Rubidium atomic states and typical doublet transitions of alkali metals commonly used in experimentation and simulations as 2 level atoms. We will use the D2 transition data (given to six significant figures here for reference) for our two level atom modelling throughout [51].

2.2 Classical Derivation of the Coupled Dipole Model

We will develop our light field, 2 level atom interaction picture with a more detailed view of the 2 level atom. It is useful here to add to our original interaction diagram with a little more detail on the internal atomic picture.

Our 2 level atoms have a single outer shell electron which enables us to treat transitions between available energy levels in a simple hydrogenic fashion. The starting point is an equation of motion for the outer shell electron behaving as a classical

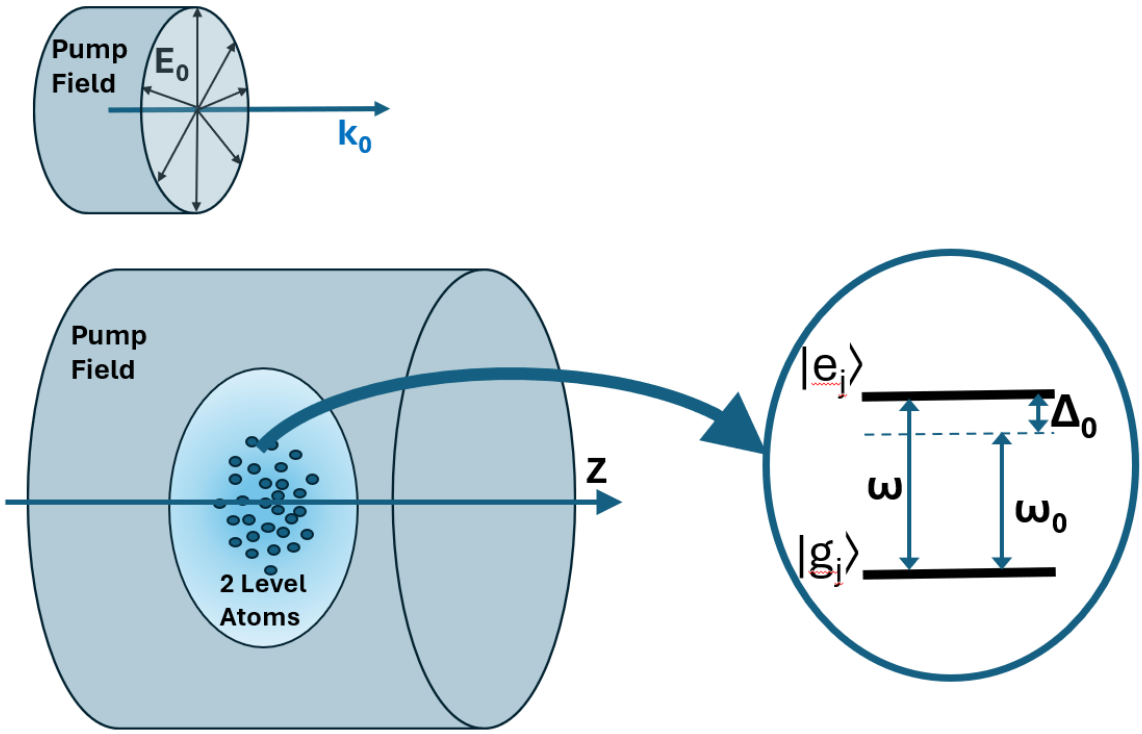

Figure 2.3: Simplified diagram of pump field aligned along Z axis, unpolarised in the transverse XY plane, interacting with 2 level cold atoms with key features shown. The atoms in the cloud have positions r_j

harmonic oscillator with frequency ω, from which point we will develop a picture of the evolution of the internal atomic dynamics interacting with a classical field [32][54].

$$\frac{\partial^2 \mathbf{r}_j(t)}{\partial t^2} + \omega^2 \mathbf{r}_j(t) = \frac{e}{m}\mathbf{E}(t, \mathbf{r}_j), \tag{2.5}$$

where $\mathbf{E}(t, \mathbf{r})$ is the electric field, e and m are the charge and mass of an electron,

respectively. For correlation with microscopic Maxwell equations it is useful to define the current density $\mathbf{j}(t, \mathbf{r})$,

$$\mathbf{j}(t, \mathbf{r}) = \sum_{j=1}^{N} e \frac{\partial \mathbf{r}_j(t)}{\partial t} \delta(\mathbf{r} - \mathbf{r_j}), \tag{2.6}$$

Using the curl of the Maxwell-Faraday equation, substitution of Ampere's Law, applying the vector calculus identity, $\nabla \times \nabla \times \mathbf{E} = \nabla(\nabla \cdot \mathbf{E}) - \nabla^2 \mathbf{E}$ and as a result of initial assumptions taking $\nabla \cdot \mathbf{E} = 0$, due to balanced charges over the slow varying $\mathbf{E}$ field amplitude considered, the following equation can be derived,

$$\nabla^2 \mathbf{E} - \frac{1}{c^2} \frac{\partial^2 \mathbf{E}}{\partial t^2} = \mu_0 \sum_{j=1}^{N} e \frac{\partial^2 \mathbf{r}_j(t)}{\partial t^2} \delta(\mathbf{r} - \mathbf{r_j}). \tag{2.7}$$

Ansatz solutions for the $\mathbf{E}$ field and electron position, r_j are helpful in line with dipole approximation, consistent with [32] we look for solutions in the form,

$$\mathbf{E}(t, \mathbf{r}) = A(t, \mathbf{r}) \exp(-i\omega t) + E_0 \exp(-i\omega t + i\mathbf{k} \cdot \mathbf{r}), \tag{2.8}$$

$$r_j(t) = \beta_j(t) \exp(-i\omega t), \tag{2.9}$$

where $A(t, \mathbf{r})$ and $\beta_j(t)$ are slowly varying functions in comparison to ω. Substitution of 2.8 and 2.9 into 2.5 and 2.7 provides initial differential equations representing dipole amplitudes.

$$\frac{\partial \beta_j(t)}{\partial t} = \frac{ie}{2\omega m}\Big[A(t, \mathbf{r}_j) + E_0 \exp(-i\omega t + i\mathbf{k}\cdot\mathbf{r})\Big], \tag{2.10}$$

$$\nabla^2 A + k^2 A = -\omega^2 \mu_0 e \sum_{j=1}^{N} \beta_j(t)\delta(\mathbf{r} - \mathbf{r_j}). \tag{2.11}$$

Now we can find a solution for $A(t, \mathbf{r})$ using a spatially retarded Green's function transformation applied to the Helmholtz type equation 2.10 which produces the result,

$$A(t, \mathbf{r}) = \frac{\omega^2 \mu_0 e}{4\pi} \sum_{j=1}^{N} \beta_j(t) \frac{\exp(ik_0 \left|\mathbf{r} - \mathbf{r_j}\right|)}{ik_0 \left|\mathbf{r} - \mathbf{r_j}\right|}. \tag{2.12}$$

The result for $A(t, \mathbf{r})$ in equation 2.12 can be substituted into 2.11 and now we have a resulting equation which is familiar and matches terms defined in the commonly accepted Coupled Dipole Model [24].

$$\frac{\partial \beta_j(t)}{\partial t} = -\frac{\Gamma}{2}\beta_j - i\frac{\Omega_0}{2}\exp(i\mathbf{k}\cdot\mathbf{r_j}) - \frac{\Gamma}{2}\sum_{m\neq j} \beta_m \frac{\exp(ik_0 \left|\mathbf{r_j} - \mathbf{r_m}\right|)}{ik_0 \left|\mathbf{r_j} - \mathbf{r_m}\right|}, \tag{2.13}$$

We have used the substitutions for the linewidth, $\Gamma = \omega^2 e^2 / 8\pi\epsilon_0 m c^3$ and Rabi term, $\Omega_0 = dE_0/\hbar$ introduced in section 1.6. We will also use the detuning, $\Delta_0 = \omega_0 - \omega$, representing the difference between the driving frequency and the oscillator frequency, where $\Delta_0 \ll \omega$. This is the source of an $e^{i\Delta_0 t}$ factor on the $\beta_j(t)$ term, in most cases in our time frames $\beta_j(t)$ can be considered to be equivalent to $\beta_j(t)e^{i\Delta_0 t}$. The cumulative cooperative third term on the RHS of the equation represents dipole-

dipole interaction and as such applies influence of atoms r_m relative to the atom in position r_j. Further description of these terms is available in [25].

This is what has been termed the Coupled Dipole Model (CDM) in [55, 25], where each atomic dipole β_j is driven by a combination of the pump field and the field generated by the other atomic dipoles.

2.2.1 Using the CDM to Determine Cooperative Scattered Field Properties

We can express the scattered field radiated in a particular mode direction $\mathbf{k}$ using constants, calculated coherences and atomic positions $r_{j,m}$ which for now are fixed. This allows us to run simulations with various distributions and scattered field modes for the purpose of validating the model.

A further simplification in terminology is introduced using k vector terms appropriate in the far field limit represented by $k_0 |\mathbf{r} - \mathbf{r_m}| \approx k_0 r - \mathbf{k} \cdot \mathbf{r_m}$ with $\mathbf{k} = k_0(\mathbf{r}/r)$ [24].

We will make use of the following equation consistent with our model for a coherently scattered field in mode $\mathbf{k}$ [48]. There is further explanation on the derivation of this equation in 2.3.

$$E_s(\mathbf{k}, t) = -\frac{\hbar\Gamma}{2d}\frac{\exp(ik_0 r)}{k_0 r}\sum_{m=1}^{N}\beta_m(t)\exp(i\mathbf{k}\cdot\mathbf{r_m}). \tag{2.14}$$

Intensity, I, where,

$$I(\mathbf{k},t) = \frac{c\epsilon_0 \left|E\right|^2}{2}, \tag{2.15}$$

in direction $\mathbf{k}$ can then be expressed as,

$$I(\mathbf{k},t) = \frac{\epsilon_0 c\hbar^2\Gamma^2}{2(dk_0 r)^2}\left(\sum_{m=1}^{N}\left|\beta_m\right|^2 + \sum_{j\neq m}^{N}\beta_j\beta_m^* \exp[i\mathbf{k}\cdot(\mathbf{r_j}-\mathbf{r_m}]\right). \tag{2.16}$$

We can now integrate intensity over all directions $\mathbf{k}$ providing a formula for the total scattered power, P_r, making use of the equality [24],

$$\int d\hat{\mathbf{k}} \exp\Big(ik_0\hat{\mathbf{k}}\cdot\mathbf{d}\Big) = 4\pi\frac{sin(k_0\left|\mathbf{d}\right|)}{k_0\left|\mathbf{d}\right|}, \tag{2.17}$$

$$P_r = -\frac{d^2k_0^4 c}{2\pi\varepsilon_0}\left(\sum_{m=1}^{N}\left|\beta_m\right|^2 + \sum_{m\neq j}^{N}\beta_j\beta_m^*\frac{sin(k_0\left|\mathbf{r_j}-\mathbf{r_m}\right|)}{k_0\left|\mathbf{r_j}-\mathbf{r_m}\right|}\right). \tag{2.18}$$

In equation 2.18 it can be observed that the first term is representative of an incoherent summation of contributions from individual dipoles. The second term can be considered an interference term. In the case of a small cloud in terms of the wavelength the phase difference in contributions is minimal and it would be expected that this term results in a cooperative build up of total radiated power realising an expected relationship of $P_r \propto N^2$ described theoretically [56] and experimentally in many papers since Dicke's work.

For simulations in this research where we require coherence calculations 2.12 or related values even we use a substitution in simulations to avoid a discontinuity with small parameter ϵ, defined in equation 2.19. This does not change the nature

of interactions and effects in our distributions which would be considered dilute. This has precedent in gravitational force simulations [57] and allows particles to pass each other without changing the general behaviour. For an equivalent atomic distribution in an experimental set up we have given equivalent values for density and other parameters in section 2.1, though most experimental set ups would be in 3D and our simulations are generally 2D. The value for ϵ most commonly used in our simulations was equivalent to a value of $k_0\epsilon = 0.1$ which corresponds to around 1/60 of a wavelength in dimensionless units used in formulae. This is consistent with CARL multimode research from Strathclyde [36] and superradiance research from Université de Côte D'Azur [17].

$$|\mathbf{r_j} - \mathbf{r_m}| \to \sqrt{|\mathbf{r_j} - \mathbf{r_m}|^2 + \epsilon^2}, \tag{2.19}$$

2.3 Quantum Derivation of Coupled Dipole Model

Using coupled dipole theory introduced in section 1.6 we have developed our microscopic model with a view to describing cooperative effects such as superradiance [17] based on coherent scattering of monochromatic light. The atomic distribution is modelled as a small fixed sample of atoms with two internal energy states. It is of particular interest to examine the weak field regime which can be modelled as a single excitation shared amongst the atomic ensemble. This model has been used as a basis for a quantum derivation of the coupled atomic coherence equations 2.13 [24, 25, 58] derived classically in section 2.2. The quantum derivation is included for completeness, specifically quantum effects will not be considered in this research.

It is useful to reference the standard field interaction Hamiltonian [48] which enables modelling evolution of field properties for the purpose of comparing our model with published results. We can refer back to key parameters used in this model illustrated in figure 2.3

$$\begin{aligned} H_I = \frac{\hbar\Omega_0}{2}\sum_{j=1}^{N}\Big[\hat{\sigma}_j \exp(i\Delta_0 t - i\mathbf{k}_0\cdot\mathbf{r}_j) + h.c.\Big] \\ + \hbar\sum_{j=1}^{N}\sum_{\mathbf{k}}\Big[g_k\hat{\sigma}_j\hat{a}^{\dagger}_{\mathbf{k}}\exp(-i\Delta_{\mathbf{k}}t + i\mathbf{k}\cdot\mathbf{r}_j) + h.c.\Big], \end{aligned} \tag{2.20}$$

where $\Omega_0 = dE_0/\hbar$ represents the Rabi frequency of the incident field and $\Delta_0 = \omega_0 - \omega_a$ is the detuning between the field and the 2 level atomic transition. $\mathbf{k}$ represents the emission mode of scattered photons which in this elastic scattering description has the same frequency as the incoming field but variable direction per emission. Also used in equation 2.20 $\hat{\sigma}_j = |g_j\rangle\langle e_j|$ is the lowering operator for the j_{th} atom, $\hat{a}^{\dagger}_k$ is the photon creation operator for the mode $\mathbf{k}$ in the scattered field, and $g_k = (d^2\omega_k/2\hbar\epsilon_0 V_{ph})^{1/2}$ is the single photon Rabi frequency coupling the atomic transition to vacuum mode $\mathbf{k}$, where d is the dipole transition matrix element and V_{ph} is the mode volume associated with vacuum mode $\mathbf{k}$.

Initially we can look at the dynamic evolution of the radiated field operator $\hat{a}_{\mathbf{k}}$ for which we can solve the Heisenberg equation

$$\frac{d\hat{a}_{\mathbf{k}}}{dt} = -\frac{i}{\hbar}\Big[H, \hat{a}_{\mathbf{k}}\Big]. \tag{2.21}$$

The electric field operator for the scattered field contributes to providing a mechanism for considering output scattered field and intensity variations against baseline conditions. The aim is for the model to take into account dynamic coupling to atomic motion due to collective recoil effects considered in addition to variations of geometry, optical thickness and introduction of partial coherence to input radiation within assumption boundaries. This operator is given by a summation across all available modes with respect to the positive frequency component given as

$$\hat{E}_s(\mathbf{r},t) = \sum_{\mathbf{k}} \varepsilon_k \hat{a}_{\mathbf{k}}(t) \exp(i\mathbf{k}\cdot\mathbf{r} - i\omega_{\mathbf{k}}t), \tag{2.22}$$

where, $\varepsilon_k = (\hbar\omega_k/2\epsilon_0 V)^{1/2}$. Setting a boundary condition of zero for the initial value of the radiated field operator and following integration of the resultant of equation 2.21 based on our Hamiltonian and insertion into equation 2.22 provides a scattered electric field operator, $\hat{E}_s$, with terms dependent on incident radiation wave number, atomic transition frequency and position of fixed atoms, assuming an initial condition of $\hat{a}_{\mathbf{k}}(t) = 0$. This derivation has been described in more detail in [24].

We can apply this operator to a baseline state of atoms and photons with terms describing a single excitation among the atoms and a single scattered photon ignoring virtual transitions [32], such that

$$\hat{E}_s \left|\psi\right\rangle = E_s \exp(i\omega_0 t) \left|g_1 ... g_N\right\rangle, \tag{2.23}$$

$$E_s(\mathbf{r},t) = -\frac{\hbar\Gamma}{2d}\sum_{m=1}^{N}\beta_m(t)\frac{\exp(ik_0\left|\mathbf{r_j}-\mathbf{r_m}\right|)}{k_0\left|\mathbf{r_j}-\mathbf{r_m}\right|}. \tag{2.24}$$

This is a significant result from defined initial conditions and assumptions from which it can be determined that the radiated field can be represented by a summation of spherical waves originating from atomic dipoles. Here $\beta_m(t)$ which can be described as the atomic coherence represents the coefficient of the state where there is one excitation among the atoms and no photon. Significantly this equates to the term β_j introduced in 1.6 as the dipole amplitude in the classical derivation.

To further investigate the evolution of the cooperatively scattered optical field it is useful to solve for the dipole amplitude terms β_j for $j = 1$ to N in an atomic ensemble. Initially this is done for the steady state, solving equation 2.13 for β_j.

2.3.1 Simulation of Superradiance using the Coupled Dipole Model

We are now in a position to run a simulation using the CDM to calculate evolving values for the atomic coherences, β_j and resultant scattered field intensity values, $\mathbf{I}(\mathbf{k},t)$. This allows us to benchmark our model against published work detailing numerical results for expected cooperative effects. For this purpose we will look at the evolving scattered field profile in a superradiant regime [17]. We can run our model with the same initial conditions as presented in the paper and present the results for intensity evolution in the XZ plane where the Z axis is in the direction of the pump field. We apply the adiabatic approximation specified in 2.1 to coupled equations 2.13 for our simulation and use equation 2.16 to calculate intensity evolution in all

directions in the XZ plane.

We are replicating an experimental set of results measured from a dilute sphere of cold 2 level atoms in a Gaussian distribution which are driven to a steady state by a continuous collimated weak field laser in the Z direction. Results for scattered far field intensity are taken after the pump field laser is switched off and the decay rate measured against the peak initial intensity in different directions is observed over time. In this experiment off-axis measurements are taken in the XZ plane at an angle of $\theta = \pi/2$ from the Z axis and at $\theta = 0$ in the forward direction corresponding to the pump field direction along the Z axis.

An illustration of the experimental set up is shown in figure 2.4. We use the same parameters specified in [17] and present our results in figure 2.5.

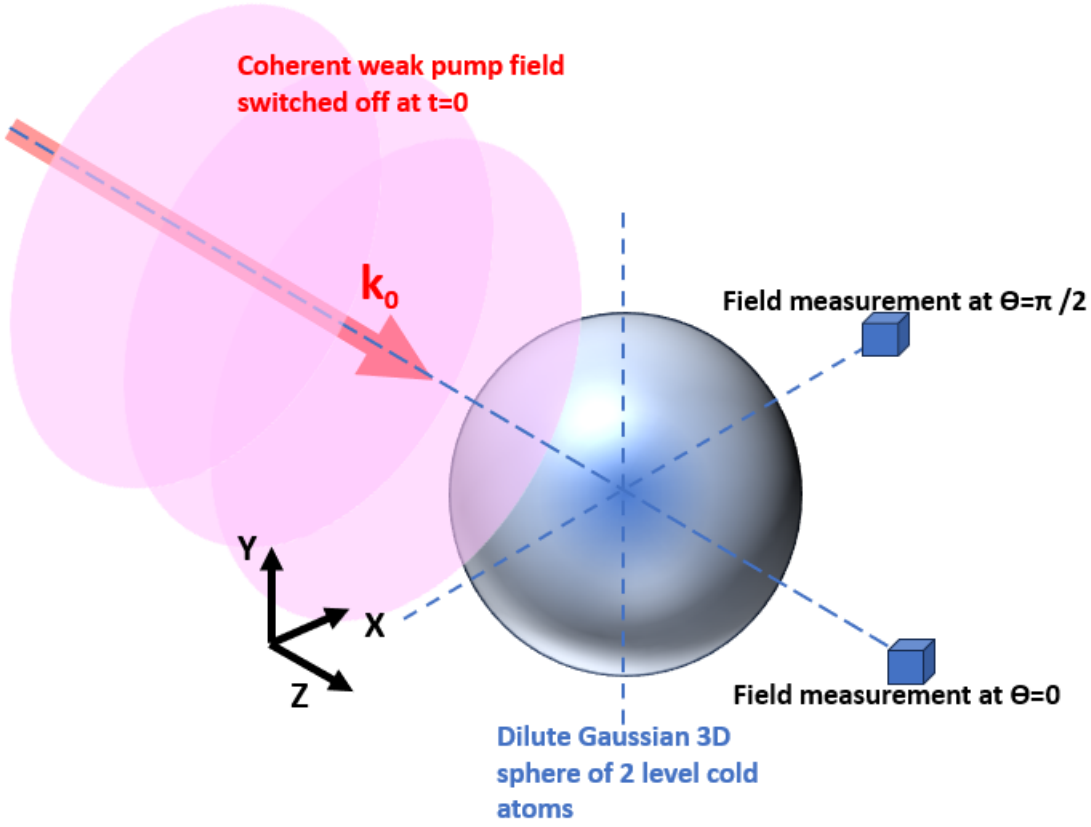

Figure 2.4: Experimental set up for scattered intensity evolution results from Nice group [17] which we seek to emulate using our model.

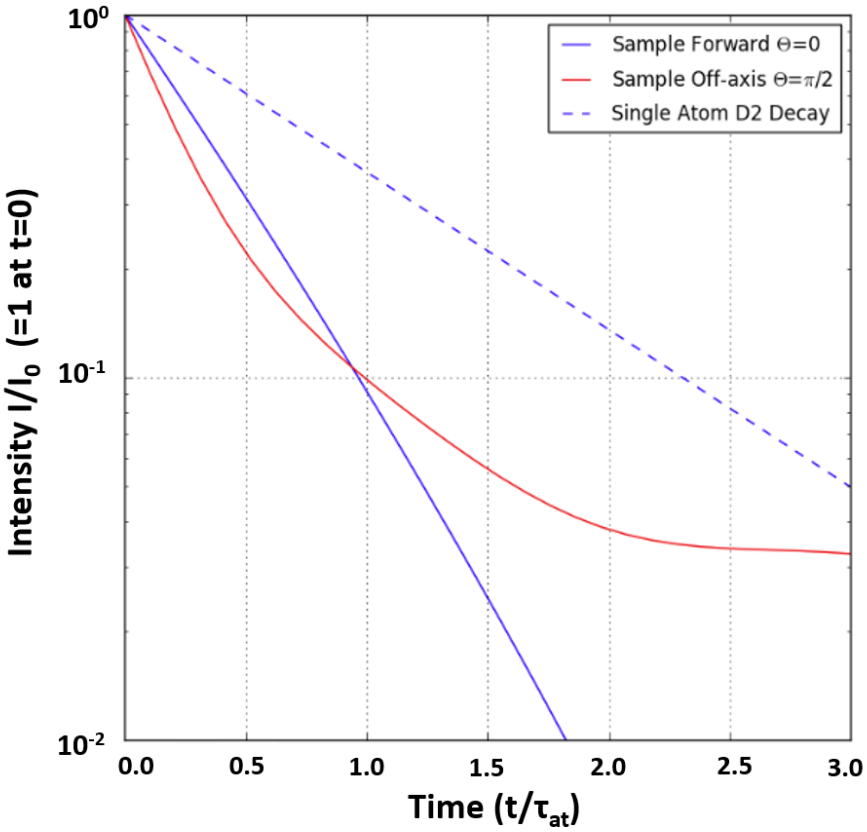

Figure 2.5: Superradiant signature cooperative behaviour from our simulation based on parameters from [17] which for reference correspond to $b_0 \approxeq 12$, R, the radius of the approximate sphere in our case $\approxeq 2\lambda$, $N \approxeq 500$, $\omega_0 \ll \Gamma$, $N\lambda^3 \approxeq 5$, $\Delta \approxeq 10\Gamma$. Again the measured intensity is normalised to the steady state value, I_0, which is much larger for $\theta = 0$.

We can compare the key features of results from our simulation with published work [17]. We have observe same signature behaviour for far-field forward and off-axis intensity evolution. What is not immediately obvious from the graph is that the zero on the time scale corresponds to a time where after reaching a steady state, in terms of collective and individual dipole response from the atomic cloud, the pump field is turned off and the behaviour of the scattered field is observed from that point with the standard single atom decay behaviour is shown by the dotted line. The intensity evolution is normalised against the initial intensity value in that direction. The time scale is normalised to the state lifetime of the excited state $\tau_{at} = \Gamma^{-1}$. At these time scales the positions of the atoms can be assumed to be fixed as they are much shorter than an absorption emission cycle based on the recoil frequency, ω_r, which is indicative of the timescales involved in changes in atomic motion and position. The intensity evolution shows an accelerated decrease from the initial value shows a faster cooperative relaxation of the distribution indicative of superradiance. In our case the gradient indicates a situation where $\Gamma_{Cooperative} \approxeq 2.5\Gamma$ for $\theta = \pi/2$ and $\Gamma_{Cooperative} \approxeq 1.8\Gamma$ for $\theta = 0$ where $\Gamma \gg \omega_r$ which is consistent with results for superradiant behaviour in [17].

3 Modelling Cooperative Effects Including Centre of Mass Motion

3.1 Optical Binding and the Addition of Centre of Mass Motion to the Model

Investigation of the mechanical effects of light fields upon microscopic particles was a natural progression from initial work on atomic manipulation with light successfully applied in laser cooling [59] [60]. This would lead to work in trapping or manipulation of particles with no physical contact. These particles would typically be in colloidal solution form with an additional viscous force compared to atomic modelling work in this area as described in [61]. In terms of looking at the forces involved which can translate between the point dipole and nanoscale objects (in the region of a wavelength in size) it is useful to make reference to gradient and scattering forces introduced in section 1.4 with a view to coupling the resultant motion into our model such that we can further examine CARL and other cooperative phenomena.

The gradient force is the result of the interaction between a permanent or induced dipole with the gradient of the resultant field intensity. This is the principal cause of self-consistent pattern formation where particles will either be attracted to or repelled from areas of high or low field intensity (in our case depending on the frequency dependent complex atomic polarisability described in equations 1.8 and 1.9) which in turn contributes to the developing distribution pattern. The scattering or radiation pressure force is dependent on the momentum change in the light field due to an absorption and re-emission of the input pump field which will vary depending on the

emission field profile but will usually predominantly generate forces principally in the direction of propagation of the pump field. The relative contribution of these force terms depend on the detuning of the pump field as defined in 2.1. The cooperative nature of the interaction has a dependency on the coherent summation of pump and scattered field which would normally require a weak field (in the atomic case weak excitation), a single scattering environment and dilute distribution of particles such that the phase profile of the resultant field is conserved. In the alternative multiple scattering environment not applicable here the phase profile would rapidly average out leading to familiar radiative transfer equations and diffusive models for propagation of light fields [62]. Particularly in the case of the optical binding regime for cold atoms we seek to build upon equations and assumptions applied in previous work describing two atom optical binding [42]. The main components of this model are illustrated in figure 3.1 which shows multiple atoms involved in binding further to the original two atom situation.

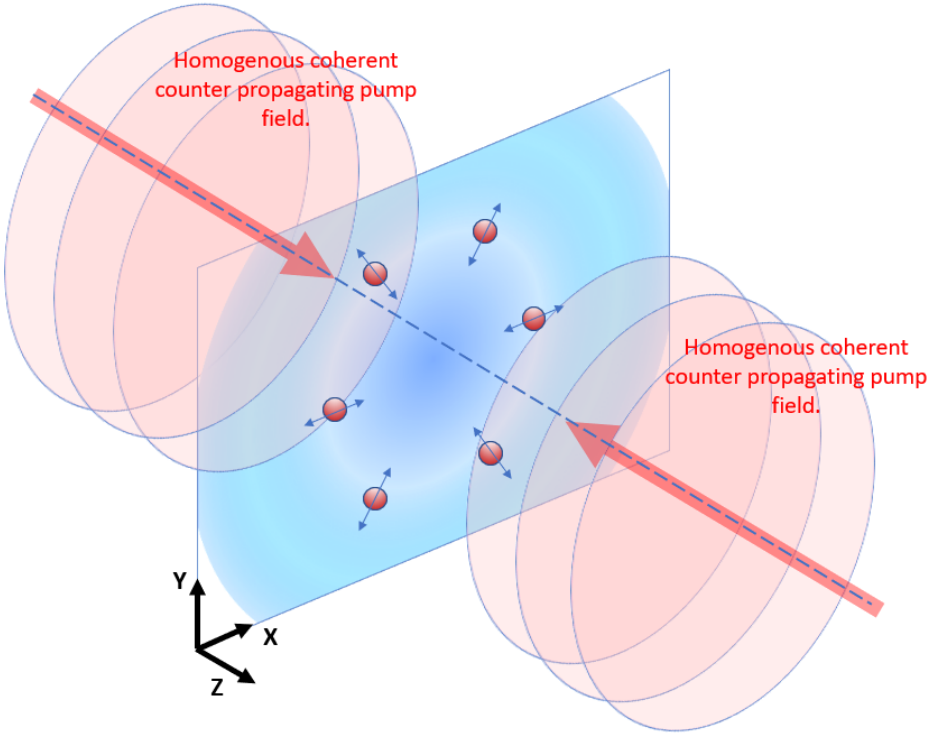

Figure 3.1: Multiple atom 2D Optical binding model. Six Atoms shown but simulations may have varied distributions with motion confined to the XY plane. Weak field trapping incident radiation propagates along the Z axis from coherent sources as shown.

3.1.1 Coupling of Atomic Motion to the Model

We can consider a fixed atomic distribution interacting with a pump field tuned close to resonance with the D2 transition similar to the 2 atom optical binding case [42]. We have derived formulae for calculating the atomic internal degrees of freedom, the coherences, β_j, calculated in equation 2.13. These are given in the multiple atom

case consistent with our environment and model by,

$$\frac{\partial \beta_j(t)}{\partial t} = \left(\mathrm{i}\Delta - \frac{\Gamma}{2}\right)\beta_j - \mathrm{i}\Omega_0 - \frac{\Gamma}{2}\sum_{l\neq j}^{N}\beta_l \frac{\exp(\mathrm{i}k_0\left|\mathbf{r_j}-\mathbf{r_l}\right|)}{\mathrm{i}k_0\left|\mathbf{r_j}-\mathbf{r_l}\right|}. \tag{3.1}$$

There is a difference in the coefficient of the Rabi term, Ω_0 between equations 2.13 and 3.1, this is accounted for in treating the pump field as a counterpropagating plane wave. We can assume that the ring of atoms is motionless in the Z plane. Although the radiation pressure force would become more prevalent close to resonance in environments such as those used to demonstrate optical binding in which the detuning, Δ and Rabi term Ω_0 are small in comparison to the linewidth, Γ, the counterpropagating nature of the pump field means there is no favoured direction for a radiation pressure force term and spontaneous emission is also limited by the weak excitation.

We want to couple the external degrees of freedom (evolving position and velocity) into our model so we will proceed using the equations and definitions describing optical interaction forces from section 1.4.

We will continue to describe 2 level cold atom distributions as behaving like point dipoles. We will define a potential in terms of a Hamiltonian representing a perturbation due to the individual and collective atom field interaction. We can then derive and define our force terms in a familiar manner by taking the negative spatial derivative of the potential field.

Therefore taking the Hamiltonian representing the perturbation as $\mathbf{H_I} = -\mathbf{d}\cdot\mathbf{E}$ we have,

$$\mathbf{F} = -\nabla \mathbf{H_I} = \nabla(\mathbf{d} \cdot \mathbf{E}) = (\mathbf{d} \cdot \nabla)\mathbf{E}, \tag{3.2}$$

where in this case we shall use familiar terms for the dipole moment, $\mathbf{d}$, and for the electric field,

$$\mathbf{E} = \frac{1}{2}(A_0(\mathbf{r}) \exp(-i\omega_0 t) + c.c.)\hat{\mathbf{e}}, \tag{3.3}$$

where $\hat{\mathbf{e}}$ is a unit transverse vector of the field.

We can see the direct correspondence between the derivation carried out here based on 3.2 and the defined optical forces we are considering described in section 1.4.

For a 2 level atom we represent the state using,

$$|\psi(t)\rangle = \sum_{j=1,2} a_j(t) \, |\phi_j\rangle = a_1(t) \, |\phi_1\rangle + a_2(t) \, |\phi_2\rangle \, , \tag{3.4}$$

where $|\phi_{1,2}\rangle$ are unperturbed states consistent with usual treatment of orthogonal Dirac states $\langle \phi_i | \phi_j \rangle = \delta_{ij}$. Introducing density matrix notation,

$$\hat{\rho} = \langle \psi | \psi \rangle = \begin{pmatrix} \rho_{11} & \rho_{12} \\ \rho_{21} & \rho_{22} \end{pmatrix} = \begin{pmatrix} a_1 a_1^* & a_1 a_2^* \\ a_2 a_1^* & a_2 a_2^* \end{pmatrix}, \tag{3.5}$$

where, $\rho_{ij} = a_i a_j^*$ as shown in equation 3.5. The dipole operator,

$$\hat{\mathbf{d}} = \begin{pmatrix} 0 & \langle\phi_1|\,\mathbf{d}\cdot\mathbf{E}\,|\phi_2\rangle \\ \langle\phi_2|\,\mathbf{d}\cdot\mathbf{E}\,|\phi_1\rangle & 0 \end{pmatrix} = \begin{pmatrix} \mu_{11} & \boldsymbol{\mu_{12}} \\ \boldsymbol{\mu_{21}} & \mu_{22} \end{pmatrix}, \tag{3.6}$$

is also shown as a matrix in equation 3.6 with $\mu_{\mathbf{ij}}$ representing matrix elements for the dipole operator in this case. The dipole operator matrix terms follow the convention that $\mu_{11} = \mu_{22} = 0$ since the dipole operator is an odd function and $\boldsymbol{\mu_{12}} = \boldsymbol{\mu_{21}}$ is real. That is, the dipole operator would normally introduce a coupling between states without influencing the state energies themselves therefore we would expect $\langle\phi_n|\,\mathbf{d}\cdot\mathbf{E}\,|\phi_n\rangle = 0$.

We can expand the expectation value of the dipole moment, $\langle\mathbf{d}\rangle$,

$$\langle\mathbf{d}\rangle = \mathbf{Tr}(\hat{\mathbf{d}}\hat{\rho}) = a_1a_1^*\mu_{11} + a_2a_1^*\boldsymbol{\mu_{12}} + a_1a_2^*\boldsymbol{\mu_{21}} + a_2a_2^*\mu_{22}. \tag{3.7}$$

Then we can simplify to,

$$\langle\mathbf{d}\rangle = (\rho_{21} + c.c.)\mu_{21}. \tag{3.8}$$

We can now substitute this simplified dipole moment to the force equation 3.2 which can be written,

$$\mathbf{F} = \frac{1}{2}(\rho_{21} + c.c.)(\nabla A(\mathbf{r})\exp(-i\omega t) + c.c)(\boldsymbol{\mu_{21}}\cdot\hat{\mathbf{e}}), \tag{3.9}$$

In order to complete the derivation of the force term for our microscopic model

we make use of the Bloch equation formalism [63] for a 2 level atom in a coherent monochromatic field. The optical Bloch equations will be referred to again and are significant in our force derivations terms so the main principles will be summarised here. We take a Hamiltonian for a 2 level atom including an interaction term containing the atomic dipole and light field, $-\mathbf{d}\cdot\mathbf{E}$ as described earlier. The Schrödinger equation is applied to a wavefunction representing the two available states. A density matrix methodology can be used to determine the time evolution of states we are interested in where we take density matrix terms, $a_1a_1^*, a_2a_2^*$ representing state populations and $a_1a_2^*, a_2a_1^*$ representing atomic coherences. The optical Bloch equations provide the time evolution for these states incorporating the Rabi term and spontaneous emission rate (or transition linewidth) allowing us to make determinations about state population and atomic coherence behaviour which will vary depending on the relative size of the Rabi term and the transition linewidth, Γ.

Further to state and perturbation definitions introduced in 3.2 and 3.4 we use the Schrodinger equation for state evolution and state level energy eigenvalues for the unperturbed Hamiltonian, $\mathbf{H_0}$.

$$i\hbar\frac{\partial\left|\psi\right\rangle}{\partial t} = \left(\mathbf{H_0} + \mathbf{H_I}\right)\left|\psi\right\rangle, \tag{3.10}$$

$$\mathbf{H_0}\left|\phi_{1,2}\right\rangle = E_{1,2}\left|\phi_{1,2}\right\rangle, \tag{3.11}$$

where $E_{1,2}$ are the energy eigenvalues corresponding to the unperturbed Hamiltonian for atomic states $|1\rangle$ and $|2\rangle$.

Substituting our state equation 3.4 into the Schrodinger equation 3.10 and applying $\langle\psi_{1,2}|$ to the resulting equations, we retrieve the following dynamic equations for the coefficients given in 3.4,

$$\frac{da_1}{dt} = -i\omega_1 a_1 + \frac{i}{\hbar} a_2 \mathbf{E} \cdot \boldsymbol{\mu_{12}}, \tag{3.12}$$

$$\frac{da_2}{dt} = -i\omega_2 a_2 + \frac{i}{\hbar} a_1 \mathbf{E} \cdot \boldsymbol{\mu_{21}}, \tag{3.13}$$

Again following established Quantum Electro-Dynamic models in the semiclassical regime [64] we can make use the standard definitions for state frequencies $\omega_{1,2} = \frac{E_{1,2}}{\hbar}$ and for the dipole matrix elements, $\boldsymbol{\mu_{ij}} = e \langle\phi_i| \mathbf{r} |\phi_j\rangle$.

In all cases for our model the atoms are weakly driven where $s \ll 1$ 2.1 which means we can apply the assumption $a_2 \approx 0$ and $a_1 \approx 1$ and recalling that $\rho_{ij} = a_i a_j^*$ provides the coherence rate equation,

$$\frac{d\rho_{21}}{dt} = -i(\omega_2 - \omega_1)\rho_{21} + \frac{i}{\hbar}\mathbf{E} \cdot \left(|a_1|^2 \boldsymbol{\mu_{21}} - |a_2|^2 \boldsymbol{\mu_{12}} \right). \tag{3.14}$$

Consistent with the interaction model used here, the CDM described in section 2.2 and in other published works with further derivation in [48], $\rho_{21} = \beta \exp(-i\omega_0 t)$ also applying $\Delta = \omega_2 - \omega_1 - \omega_0$ and including a boundary condition of $|\psi(t=0) = |\phi_1\rangle\rangle$,

$$\frac{d\beta}{dt} = i\Delta\beta + i\frac{A}{2\hbar}\hat{\mathbf{e}} \cdot \boldsymbol{\mu_{21}}. \tag{3.15}$$

We can compare this with the derived solution across research groups for the coupled coherence rate equations [65],

$$\frac{d\beta_j}{dt} = \left(i\Delta - \frac{\Gamma}{2}\right)\beta_j - i\Omega(r) - \frac{\Gamma}{2}\sum_{m\neq j}\beta_m \frac{\exp\{(ik_0\left|\mathbf{r_j}-\mathbf{r_m}\right|)\}}{ik_0\left|\mathbf{r_j}-\mathbf{r_m}\right|}. \tag{3.16}$$

We can apply incoherent damping as described in the Bloch equation model for coherences [63] to introduce the $-\frac{\Gamma}{2}\beta_j$ term. This leads to a conclusion that the following values have an equivalence in the CDM derivation,

$$\frac{A(r)}{2\hbar}\hat{\mathbf{e}}\cdot\boldsymbol{\mu_{21}} = -2\Omega(r) + i\Gamma\sum_{m\neq j}\beta_m \frac{\exp\{(ik_0\left|\mathbf{r_j}-\mathbf{r_m}\right|)\}}{ik_0\left|\mathbf{r_j}-\mathbf{r_m}\right|}, \tag{3.17}$$

This is a significant result in that it confirms the expected result of the single scattering model inferring that the total electric field is a summation of the position dependent pump field and a first order scattering term from other atomic dipoles.

Now referring back to the force equation 3.9 we can perform a substitution using 3.17 to provide an equation from which we can resolve cumulative forces on individual atoms based on coherence values, Rabi term, transition linewidth and position.

$$\mathbf{F_j} = -\hbar(\beta_j\nabla\Omega_j^*(r) + c.c) + i\hbar\frac{\Gamma}{2}\left(\sum_{m\neq j}\beta_m\beta_j^*\nabla\frac{\exp\{(ik_0\left|\mathbf{r_j}-\mathbf{r_m}\right|)\}}{ik_0\left|\mathbf{r_j}-\mathbf{r_m}\right|} - c.c\right), \tag{3.18}$$

We can see from the nature of the resulting force equation 3.18 that the first term depending on the light field (via the Rabi term) is a single atom force term and

the second term is a cooperative interatomic force term. Given that the complex conjugate is subtracted in the second cumulative term we can rewrite an equation for the force on one atom due to another atom in a distribution in this regime. If we again consider the set up in figure 3.1, given that we have coherent counter-propagating light fields we will create a stationary field with no transverse gradient in the XY plane. Therefore for the specific case of the optical binding regime in this section we can approximate the single atom force term to be zero on this occasion.

Therefore in this case for our optical binding scenario described in figure 3.1 we have a final force equation of,

$$\mathbf{F_j} = \hbar\Gamma \mathrm{Im}\left[\sum_{l\neq j}^{N} \hat{\mathbf{r}}_{jl}\left(\frac{\exp(\mathrm{i}k_0\left|\mathbf{r_j}-\mathbf{r_l}\right|)}{\left|\mathbf{r_j}-\mathbf{r_l}\right|}+\frac{\mathrm{i}\exp(\mathrm{i}k_0\left|\mathbf{r_j}-\mathbf{r_l}\right|)}{k_0\left|\mathbf{r_j}-\mathbf{r_l}\right|^2}\right)\beta_j\beta_l^*\right]. \tag{3.19}$$

This provides us with equations of motion for our distributions coupled to the position dependent atomic coherence equations 3.15.

We can solve these coupled equations numerically to dynamically calculate the external degrees of freedom of the atoms from initial position data and evolving atomic coherences from equations. This allows us to incorporate centre of mass motion due to optical forces into our model which is described in the following section 3.1.2.

3.1.2 Implementation of Coupled Dipole Model Including Atomic Motion and Optical Forces

From here we can generate a series of first order ordinary differential equations using momenta and position of atoms. This allows us to use integration methods with our

model to produce results for the evolving position of atoms in time consistent with our aims to investigate cooperative phenomena of the nature described in section 1.5.

For the purposes of using the results generated for the atomic coherences 3.1 and the related resultant Force equations 3.18 to generate position evolution data for atomic clouds in the cooperative regimes we are interested in it is useful to define dimensionless variables.

We use, $\mathbf{R}_j = k\mathbf{r}_j$, $\tau = \Gamma t$, $\bar{\Delta} = \Delta/\Gamma$, $\bar{\Omega} = \Omega/\Gamma$, based on previously defined variables for position, time, detuning and the Rabi term. For actual calculations we would have seperate differential equations for X, Y and Z dimensions as required. For clarity we will use a single dimension for position.

Now we can rewrite the force equation 3.18 making use of the notation, $q_{jm} = k\left|\mathbf{r_j} - \mathbf{r_m}\right|$ and the unit vector $\hat{\mathbf{r}}_{jm}$ pointing in the direction of $\mathbf{r}_{jm}$ as,

$$\frac{d^2\mathbf{R}j}{d\tau^2} = -\frac{\hbar k^2}{m\Gamma}(\beta_j \bar{\nabla}\bar{\Omega}_j^*(r) + c.c) - \frac{\hbar k^2}{m\Gamma}\sum_{m\neq j}\beta_m\beta_j^*\left(\frac{\sin q_{jm}}{q_{jm}} + \frac{\cos q_{jm}}{q_{jm}^2}\right)\hat{\mathbf{r}}_{jm}. \quad (3.20)$$

We will take the X component of acceleration due to cumulative force which will take the form,

$$\frac{d^2\mathbf{X}j}{d\tau^2} = -2\bar{\omega}_r(\beta_j\frac{\partial\bar{\Omega}_j^*(r)}{\partial X} + c.c) - 2\bar{\omega}_r\sum_{m\neq j}\beta_m\beta_j^*\left(\frac{\sin q_{jm}}{q_{jm}} + \frac{\cos q_{jm}}{q_{jm}^2}\right)\left(\frac{X_j - X_m}{q_{jm}}\right), \tag{3.21}$$

where $\bar{\omega}_r = \frac{\hbar k^2}{2m\Gamma}$ is a dimensionless recoil frequency. We will define the dimensionless momentum, $\mathbf{P} = \frac{m\mathbf{v}}{\hbar k}$. Now we can rewrite as a series of first order ODEs,

$$\frac{d\mathbf{X}j}{d\tau} = 2\bar{\omega}_r\mathbf{P}_x, \tag{3.22}$$

$$\frac{d\mathbf{P}_{x(j)}}{d\tau} = -(\beta_j\frac{\partial\bar{\Omega}_j^*(r)}{\partial X} + c.c) - \sum_{m\neq j}\beta_m\beta_j^*\left(\frac{\sin q_{jm}}{q_{jm}} + \frac{\cos q_{jm}}{q_{jm}^2}\right)\left(\frac{X_j - X_m}{q_{jm}}\right), \tag{3.23}$$

Given a state vector representing the initial state of an atomic cloud in terms of position and momenta in the dimensions required and using our 1st order ODEs we can use a Runge-Kutta 4th order integration method to numerically model the evolution of the position and momenta values for our distributions. This is the method used in simulations within this research.

3.1.3 Optical Binding Simulations

In this section we will describe optical binding as shown in figure 3.1 for two atom, three atom and multiple atom regimes. We first validate our model by simulating optical binding of two atoms as described in [42]. It was found that collective light

mediated forces can act to form a bound or metastable state depending on whether detuning of the counter-propagating pump field is positive or negative. Figure 3.2 shows the same behaviour on the same timescales using similar data as original findings [42]. The position data for 2 atom optical binding results from the integration of equations 3.1 and the following equation of motion between atoms using 3.18,

$$\ddot{\mathbf{r}}_{jl} = \frac{\hbar\Gamma}{m}\mathrm{Im}\left[\nabla_{\mathbf{r}}\frac{\exp(\mathrm{i}k_0\left|\mathbf{r_j}-\mathbf{r_l}\right|)}{\mathrm{i}k_0\left|\mathbf{r_j}-\mathbf{r_l}\right|}\beta_j\beta_l^*\right], \tag{3.24}$$

between atoms identifed as j and l. Position data can then be obtained by solving these ODEs as described in section 3.1.2.

The signature two atom optical binding behaviour described in [42] involves evolution of the separation of 2 atoms and the existence of a stable bound state, a metastable state or an unstable state where the two atoms quickly separate with a dependency on the detuning of the pump field and ratio of detuning, linewidth and Rabi term of the pump field. The particular characteristics of optically bound states as presented in [42] are that positive detuning results in a metastable bound state and negative detuning results in a long term bound state with some reduction in the difference between maximum and minimum separation over timescales of milliseconds. These effects will be used as indicators of optical binding behaviour for our simulations and are further examined in [66].

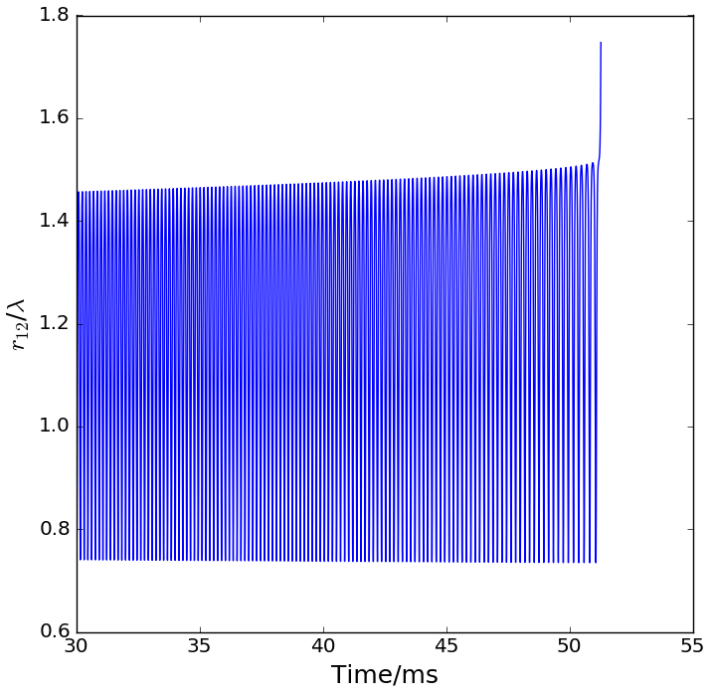

(a) Detuning of pump field normalised to the linewidth of the Rb D2 transition ,Δ/Γ=1.0 and Rabi term Ω_0/Γ=0.1

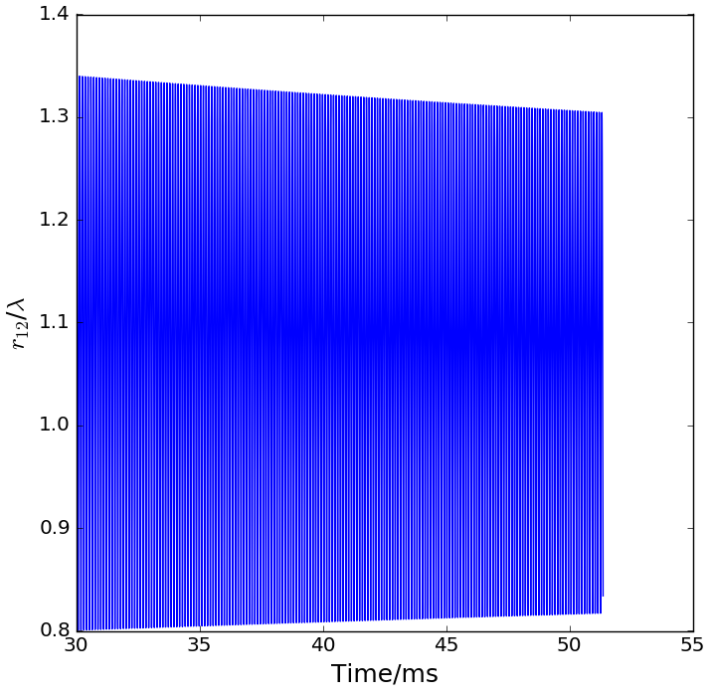

(b) Detuning of pump field normalised to the linewidth of the Rb D2 transition ,Δ/Γ=-1.0 and Rabi term Ω_0/Γ=0.1

Figure 3.2: Simulation results for comparison with results from [42] for a 2 atom arrangement in the XY plane shown in 3.1. The same conditions are applied where initial motion is considered negligible in the time scales observed prior to the introduction of the pump field. r_{12} represents atomic separation between atoms 1 and 2.

Figure 3.2 shows results for 2 atom optical binding as calculated from a numerical solution of equations 3.1 and 3.24. It shows examples of metastable and stable state behaviour respectively in the case of positive or negative detuning in agreement with [42].

3.1.4 Optical Binding of 3 Atoms

We now use our model to look for characteristics of optical binding in the case of three atoms. Results for both positive and negative detuning are shown in figures 3.4 and 3.5. It is worth observing that the system behaves in a similar fashion to 2 atom optical binding in that during stable or metastable periods of interaction we have a rotationally symmetrical formation in the XY plane so the atoms are equidistant. This means that plots for the evolution of the interatomic distance r_{jl} are the same for r_{12}, r_{23}, r_{31}.

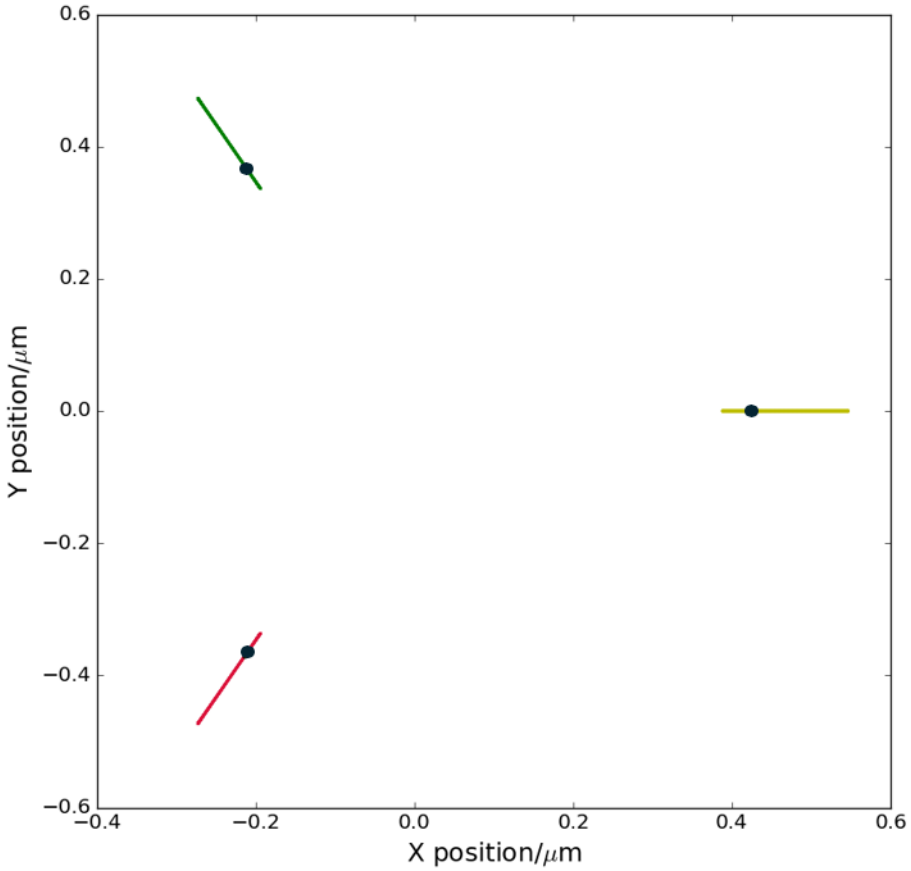

Figure 3.3: 3 atom 2D optical binding, Δ/Γ=1.0, Ω_0/Γ=0.1, (lines show paths atoms follow back and forth over multiple cycles, bordered dots are final positions).

The atomic trajectories for the 3 atom bound state in the XY plane is shown in figure 3.3.

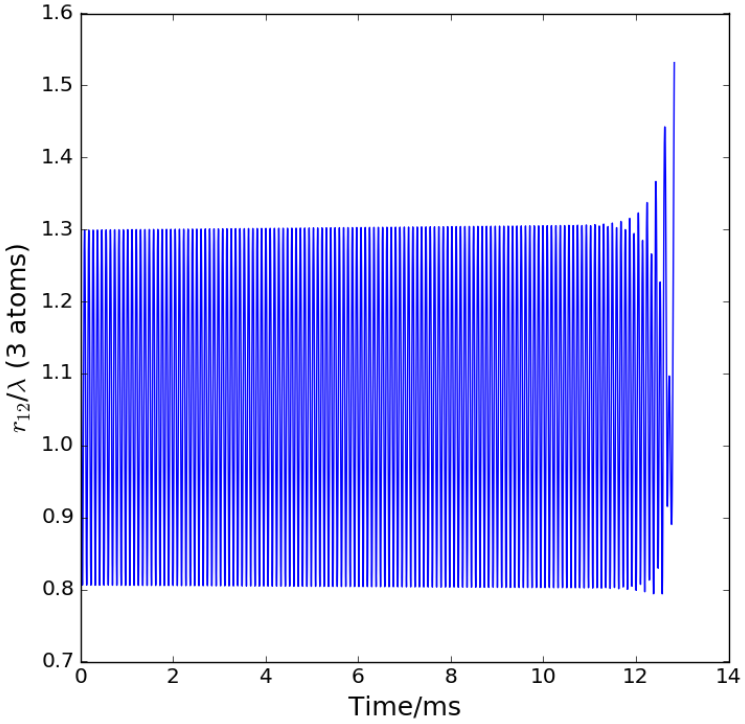

(a) Detuning of pump field normalised to the linewidth of the Rb D2 transition ,Δ/Γ=1.0 and Rabi term Ω_0/Γ=0.1

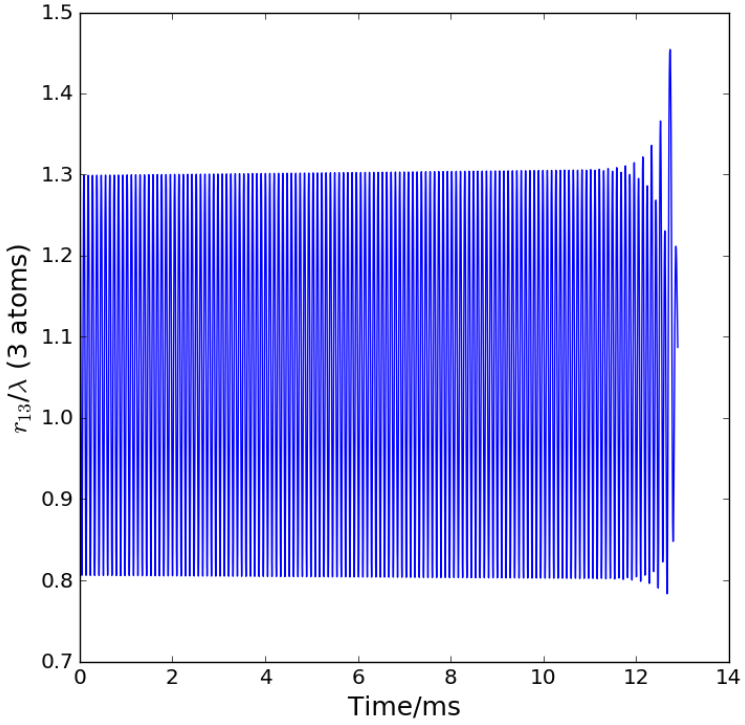

(b) Detuning of pump field normalised to the linewidth of the Rb D2 transition ,Δ/Γ=1.0 and Rabi term Ω_0/Γ=0.1

Figure 3.4: 3 atom optical binding simulation results, r_{jl} represents atomic separation between atoms j and l.

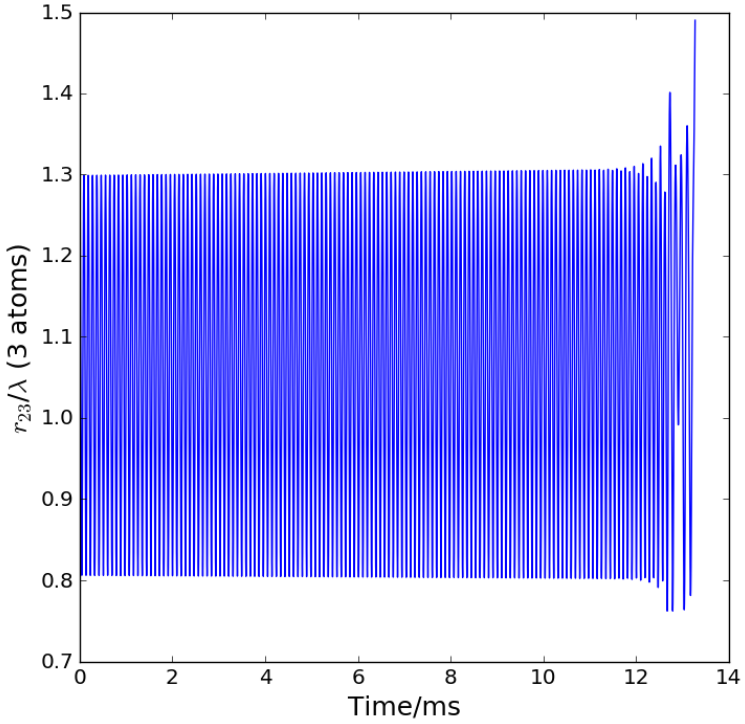

(a) Detuning of pump field normalised to the linewidth of the Rb D2 transition ,Δ/Γ=1.0 and Rabi term Ω_0/Γ=0.1

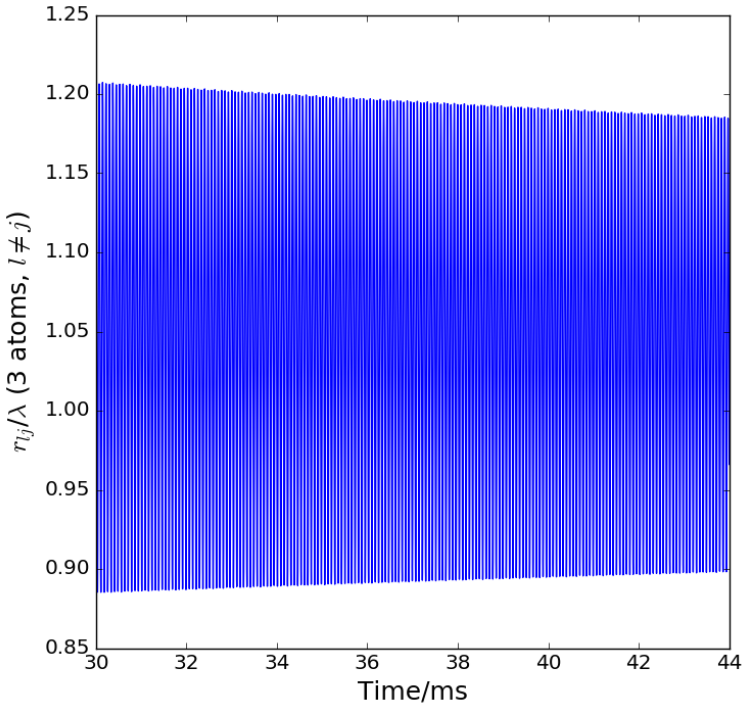

(b) Detuning of pump field normalised to the linewidth of the Rb D2 transition ,Δ/Γ=-1.0 and Rabi term Ω_0/Γ=0.1

Figure 3.5: 3 atom optical binding simulation results, r_{jl} represents atomic separation between atoms j and l. For negative detuning shown in (b) the evolution of separations r_{12}, r_{13}, r_{23} are identical.

In the simulated 3 atom case we can see patterns corresponding to metastability and loss of the bound state for positive detuning shown in figure 3.4 and 3.5. We can also see a stable bound state with a slight overall decrease in the maximum atomic separation which is identical for any two out of the three atoms in the distribution in the case of negative detuning also shown in figure 3.5. If the characteristics of optical binding as described in [42] are taken to be a signature of optical binding behaviour then figures 3.4 and 3.5 show evidence of optical binding behaviour extended to 3 atoms.

3.1.5 Optical Binding of Many Atoms

It has been observed in simulations consistent with macroscopic optical binding work in [61] that rotationally symmetric distributions of a few atoms show increased stability in terms of the lifetime of metastable states. This appears to be related to the maintenance of radial symmetry in the collective inter-atomic potential. An interesting feature of some distributions of many atoms was the existence of a 'breathing' behaviour where the radial position of the optically bound atoms oscillates.

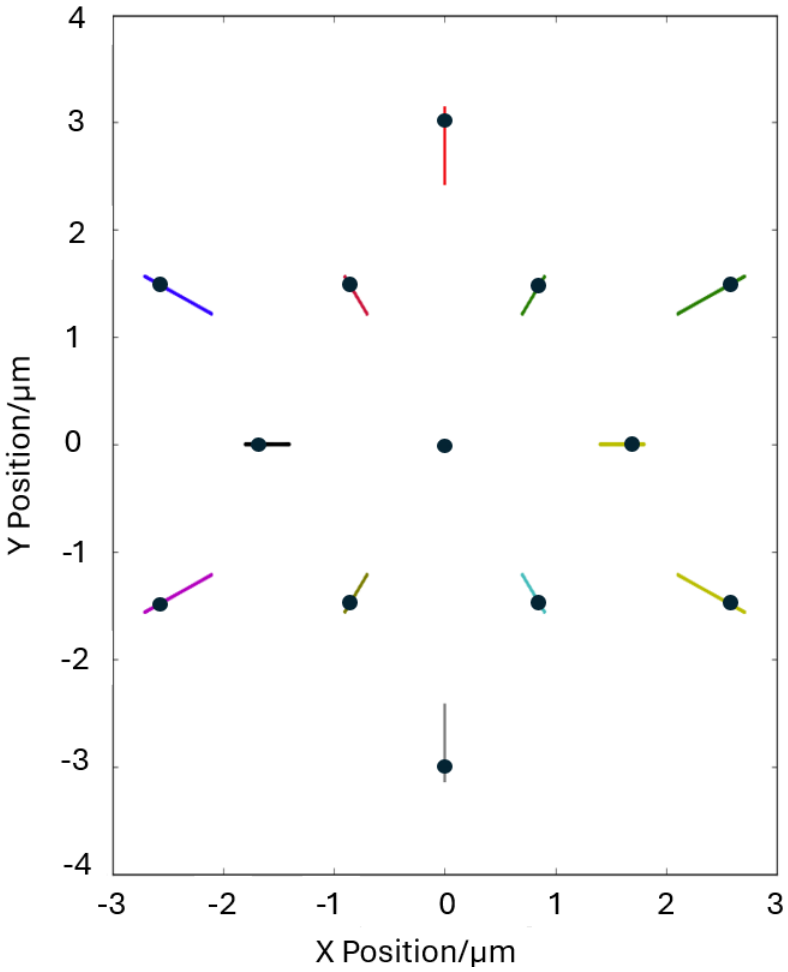

Figure 3.6: Breathing behaviour of 13 optically bound atoms (lines show atom trajectories, bordered dots are final positions). Simulation was run over a timeframe of 2.0ms with Δ/Γ=1.5, Ω_0/Γ=0.1.

An example of this 'breathing' is shown in figure 3.6 for the case of 13 atoms initially distributed in a 'star-like' pattern. This pattern is stable for multiple bound state oscillations for several milliseconds in this simulation which is unusual for larger numbers of atoms. It is worth re-iterating that these atoms have free movement in the XY plane and other regular formations were attempted which did not show the same stability as this hexagonal based arrangement. The values of the Rabi term and the detuning in relation to the pump field remain very similar to the original work on 2 atom dipole optical binding [42].

3.2 Modelling Multimode CARL

We will now show the derivations involved in the CARL model compared to the model used for this work identifying resultant equations for the forces experienced by individual atoms as a result of cooperative and single atom interactions. Firstly to briefly review our model, complex dipole amplitudes (i.e. atomic coherences) are derived for low levels of excitation corresponding to the linear optics regime, where $s \ll 1$ referred to in section 2.1. With this condition the model can operate in high detuning typical of CARL and lower detuning sometimes as applied in optical binding simulations [42]. Evolution of the complex dipole amplitudes is provided by the N coupled equations for $\dot{\beta}_j$ 3.1,

We again consider ^{87}Rb atoms with the D2 transition representing our 2 level system and atomic mass of m. In this case $\Gamma \gg \omega_r$, where the recoil frequency, $\omega_r = \hbar k^2/2m$. Working in timescales in the domain of the inverse of the recoil frequency, ω_r^{-1}, we can adiabatically eliminate the internal degree of freedom taking $\dot{\beta}_j \approxeq 0$. We then

use the force equation 3.18 derived in section 3.1.1,

$$\mathbf{F}(r_j) = -2\hbar \mathrm{Re}\left(\beta_j \nabla \Omega_j^*\right) - \hbar\Gamma \mathrm{Im}\left[\sum_{l\neq j}^{N} \hat{\mathbf{r}}_{jl}\left(\frac{\exp(\mathrm{i}k_0\left|\mathbf{r_j}-\mathbf{r_l}\right|)}{\left|\mathbf{r_j}-\mathbf{r_l}\right|} + \frac{\mathrm{i}\exp(\mathrm{i}k_0\left|\mathbf{r_j}-\mathbf{r_l}\right|)}{k_0\left|\mathbf{r_j}-\mathbf{r_l}\right|^2}\right)\beta_j^*\beta_l\right]. \tag{3.25}$$

Using the same assumptions force equations based on the position gradient of a two component Hamiltonian (pump/atoms interaction and atom/vacuum mode interaction) are calculated in the multimode CARL model shown in the following equation 3.26 [36].

$$\dot{\mathbf{p}}_j = \Gamma\hbar k_0\left(\frac{\Omega_0}{2\Delta_0}\right)^2 \sum_{l\neq j}^{N}\left\{(\hat{\mathbf{z}} - \hat{\mathbf{r}}_{jl})\frac{\sin\left[k_0(r_{jl}-z_{jl})\right]}{k_0 r_{jl}} - \hat{\mathbf{r}}_{jl}\frac{\cos\left[k_0(r_{jl}-z_{jl})\right]}{(k_0 r_{jl})^2}\right\}. \tag{3.26}$$

Where $r_{jl} = |\mathbf{r}_j - \mathbf{r}_l|$ and $\hat{\mathbf{r}}_{jl} = (\mathbf{r}_j - \mathbf{r}_l)/r_{jl}$, which is the unit vector along the distance between $\mathbf{r}_j$ and $\mathbf{r}_l$. This model described by equation 3.26 assumes classical atomic motion which is realised when the superradiant scattering rate is larger than the recoil frequency 2.1. The condition in order to neglect quantum effects in the atomic motion is that the superradiant rate $\Gamma_{k'}$ which will be associated with a particular scattering mode in both single mode [49] and multimode CARL [36] must be larger than the appropriate recoil frequency. We will compare available results from the multimode model with our results based on forces calculated using the full cooperative model per equation 3.25.

The scattered intensity in the far-field limit based on coherent spherical waves, single

scattering in the dilute cooperative regime we have described for $\mathbf{r} \gg \mathbf{r}_j$, is [36]

$$I_s(\mathbf{k}) = I_1 N^2 |M(\mathbf{k}, t)|^2, \tag{3.27}$$

where $I_1 = (\hbar\omega_0\Gamma/8\pi r^2)(\Omega_0/2\Delta_0)^2$ is the single-atom Rayleigh scattering intensity and

$$M(\mathbf{k}, t) = \frac{1}{N}\sum_{j=1}^{N} R(\rho_j) e^{i(\mathbf{k}_0 - \mathbf{k})\cdot\mathbf{r}_j(t)} \tag{3.28}$$

where,

$$R(\rho_j) = e^{-\rho^2/w^2}\left(\frac{\sqrt{2}\rho}{w}\right)^{\ell}, \tag{3.29}$$

M is the optical magnetisation and R is a factor representing the field amplitude at a given radius ρ with a beam waist w which becomes significant for values of $\ell \neq 0$ which will be considered in chapter 4. For the moment we will only consider plane waves where $\ell = 0$. The direction of the scattered field is determined by the wave-vector $\mathbf{k}$ in equation 3.28, which depends on the spatial distribution of the atoms which for the purpose of our simulations will be in the XZ or XY planes.

3.2.1 Simulations of Multimode CARL Using the Coupled Dipole Model Including Optical Forces [36]

The multimode CARL model was used to determine the evolution of elliptical cold atom distributions in the XZ plane in [36] based on calculations using equation 3.26 and applying assumptions described relevant to the Couple Dipole model. We will use similar key variables for our simulations and compare the results presented in [36] and our own results from the coupled dipole theory model coupled to atomic motion (full cooperative model). Our results are presented in figures 3.9, 3.11. Dimensionless variables are used substituting factor A into the force equation and setting it to be $A = 1.0$ as was used in [36] for the following results, where,

$$A = \Gamma/\omega_r(\Omega_0/2\Delta_0)^2, \tag{3.30}$$

with values for the Rubidium D2 transition applied this implies a ratio of $\Delta_0 \approxeq 15\Omega_0$ whilst maintaining the saturation parameter, $s \ll 1.0$.

Our results will be presented for simulations using our model incorporating centre of mass motion for a plane coherent pump field with a 2D elliptical cloud of cold atoms as shown in figure 3.7.

The aim here is to demonstrate the emergence of signature cooperative behaviours which were observed in [36] using our model. Similar values for density, axes ratio, pump field properties and atomic properties will be used and described. Measurable specific outcomes will be shown and compared to results which would demonstrate cooperative behaviour in multimode CARL.

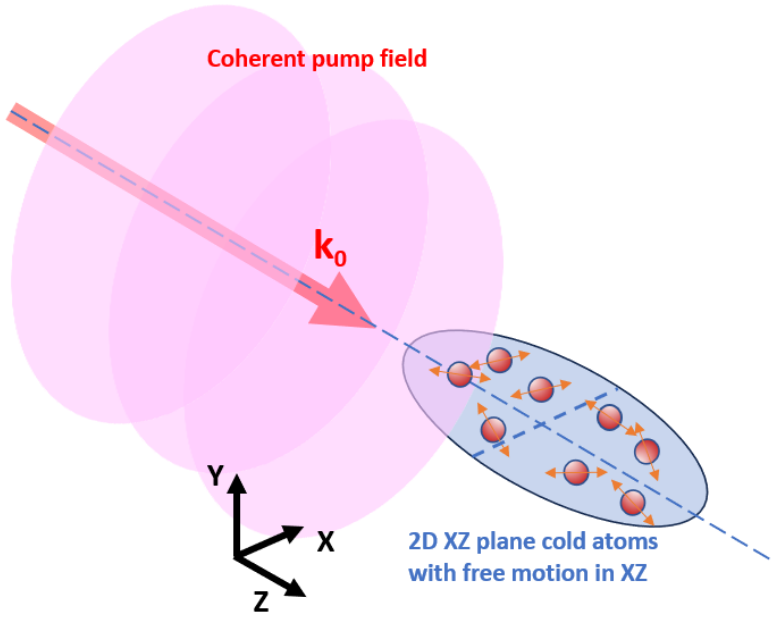

Figure 3.7: A Z direction plane pump field and an elliptical atomic distribution in the XZ plane with a main axis along Z (shown) or X.

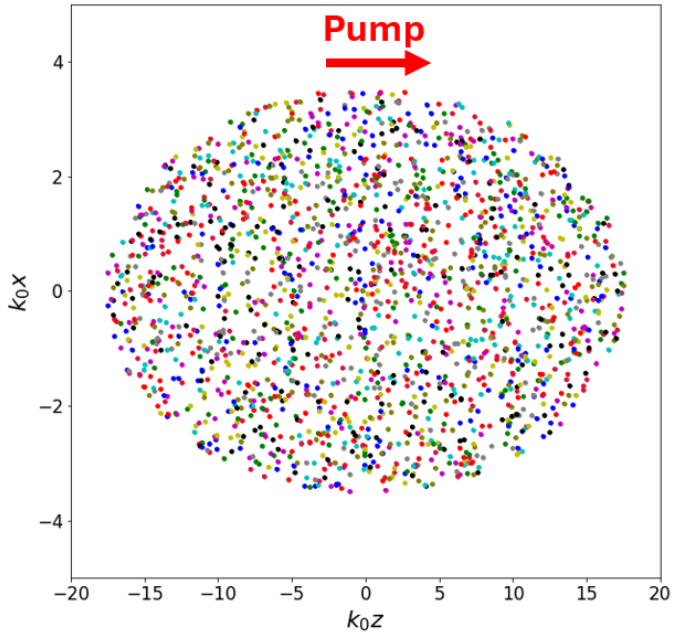

Figure 3.8: The set up this time has a single Z direction plane pump field and an elliptical atomic distribution in the XZ plane with a main axis along Z at $t = 0$.

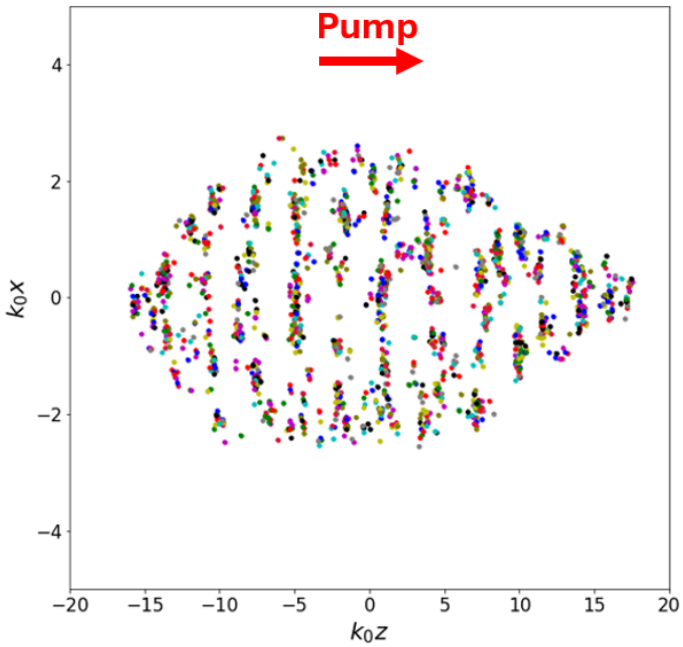

Figure 3.9: Pattern formation observed with a main Z axis ellipse using our model based on coupled dipole theory and coupled with atomic motion as described in section 3.1.2. The axis scales are chosen to provide a clearer view of pattern formation.

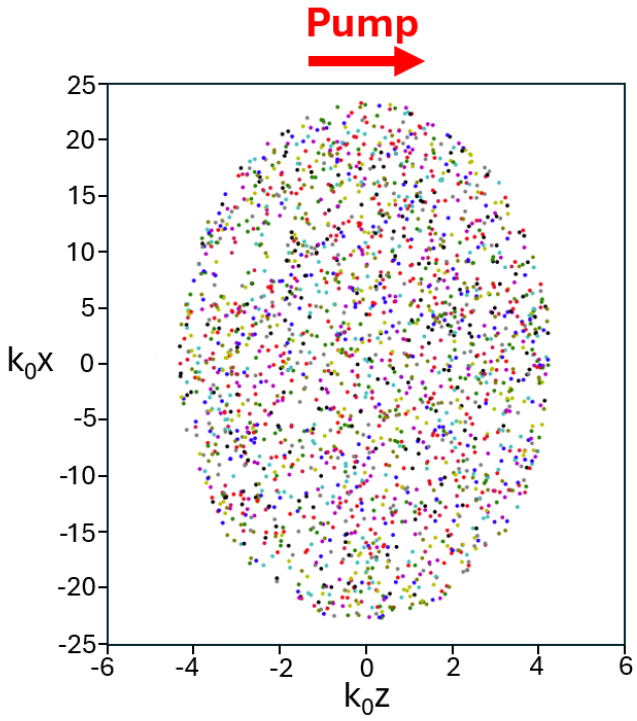

Figure 3.10: The set up this time has a single Z direction plane pump field and an elliptical atomic distribution in the XZ plane with a main axis along X at $t = 0$.

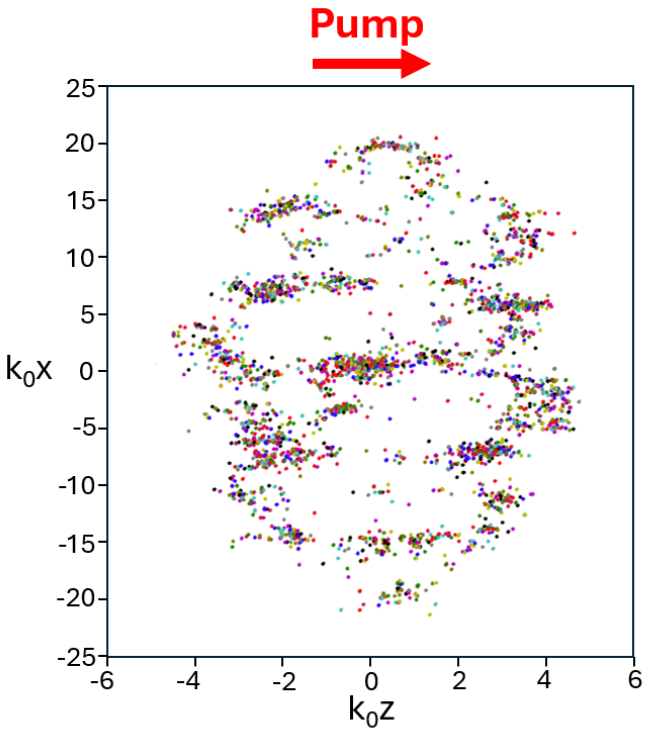

Figure 3.11: Pattern formation observed with a main X axis ellipse using our model based on coupled dipole theory and coupled with atomic motion as described in section 3.1.2. The axis scales are chosen to provide a clearer view of pattern formation.

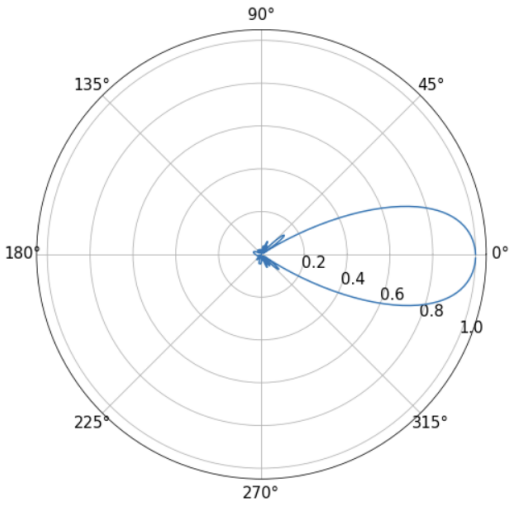

(a) Main axis Z Ellipse showing Optical Magnetisation 3.28 in the 2D XZ plane for random distribution as shown in figure 3.8 at $t = 0\omega_r^{-1}$

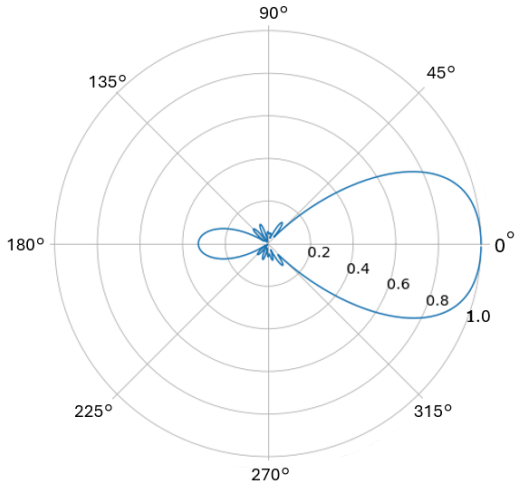

(b) Main axis Z Ellipse showing Optical Magnetisation 3.28 in the 2D XZ plane for random distribution as shown in figure 3.8 at $t = 0.25\omega_r^{-1}$

Figure 3.12

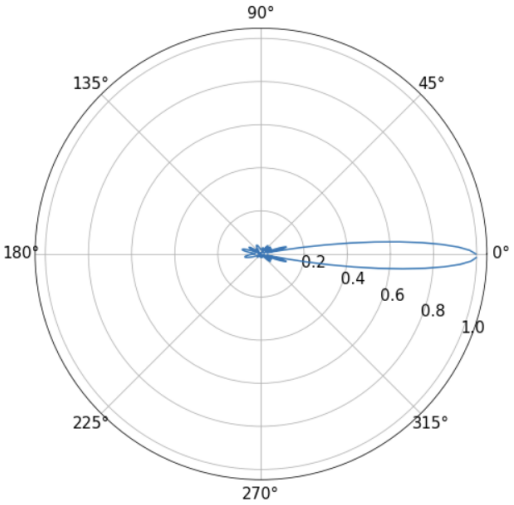

(a) Main axis X Ellipse showing Optical Magnetisation 3.28 in the 2D XZ plane for random distribution as shown in figure 3.10 at $t = 0\omega_r^{-1}$

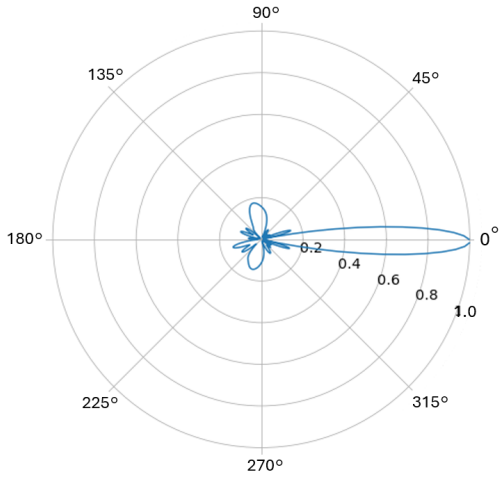

(b) Main axis X Ellipse showing Optical Magnetisation 3.28 in the 2D XZ plane for random distribution as shown in figure 3.10 at $t = 0.25\omega_r^{-1}$

Figure 3.13

There are some main points to be highlighted in the comparing our results shown in figures 3.9, 3.11 and those published in [36]. Firstly we start with random uniform distributions for $t = 0$ shown in figures 3.8 and 3.10. The saturation parameter condition is maintained as described and we choose values for the simulations in 3.9, 3.11 of Ω_0=10Γ and Δ_0=150Γ reflecting the ratio of $\Delta_0/\Omega_0 \approxeq 15$ identified in [36]. We have a slightly smaller ellipse dimension with the same ratio of major to minor axis (of approximately 5:1) and a similar density of atoms of around 25 atoms per unit squared space in k_0X, k_0Y dimensionless units used in figures. Notable signature behaviours in the multimode CARL model in [36] are the grating formation with a main Z axis ellipse or some diagonal bunching with a main X axis ellipse with a gap of approximately 2.5 in dimensionless k_0 space. The grating pattern in similar dimensions can be seen in 3.9 for our full cooperative model simulation, the diagonal pattern is there though slightly less well defined with less atoms in our simulation. Significantly the optical magnetisation evolution shows the same patterns in both the main X and main Z axes ellipses for both models including the width, relative size and position of the lobes with our results shown in figures 3.12 and 3.13. A slightly more subtle similarity can be seen in the main Z axis ellipse simulations in that there is an increased level of 'escape' from the distribution at the 'top' of the distribution in terms of Z position.

This strong correlation of results demonstrating specific signature cooperative behaviours from simulations is taken as validation of our full cooperative model with centre of mass motion that we have described and implemented for simulations.

4 CARL with Orbital Angular Momentum (OAM)

In this chapter we extend the CARL model to include pump fields possessing orbital angular momentum (OAM). The work described in this chapter contributed to a collaboration with the research group of Dr N Piovella of the University of Milan with results published in [44].

4.1 Definition of Model and Dynamics for CARL with OAM

The description of CARL in 1.6 highlighted the significance of the transfer of linear momentum between light field and a cold atomic distribution resulting in the enhancement of scattered light field modes consistent with cooperative interactions between the light field and the atomic distribution. As a natural extension to this light may also carry spin angular momentum, SAM [67] and orbital angular momentum, OAM [68]. OAM of a light field is related to an azimuthal phase dependence ($e^{i\ell\phi}$). It is well established that it is possible to transfer OAM from light to atoms in the absence of competing effects and many examples are available [69]. The work described here describes an equivalent CARL effect involving collective exchange of OAM between a pump and a scattered field as proposed in [70, 71]. Considering OAM transfer in a similar manner to the description of CARL for the transfer of linear momentum 1.7, the proposed model uses a light field propagating along a central Z axis. The helically phased wavefront of light carrying OAM is most often described using a Laguerre Gaussian (LG) mode description [72]. We will use LG modes, $LG_{n\ell}$ with a radial node index n of zero which have a characteristic transverse intensity profile which consists of a single ring which can be seen in the light

field representation in figure 4.1. The azimuthal index, ℓ, defines a magnitude of OAM of $\ell\hbar$ per photon and corresponds to the number of overlaid helical 2π phase profiles per wavelength. The value of ℓ can be varied in simulations.

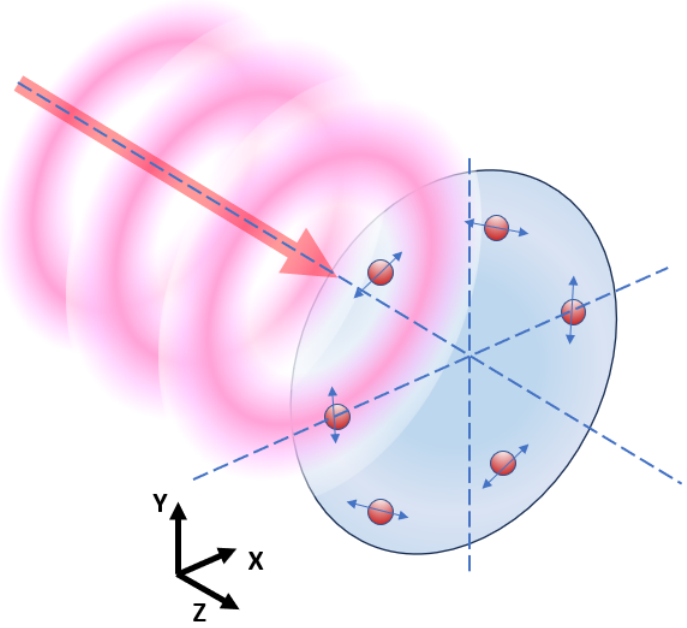

Figure 4.1: As for linear CARL described in 1.6 mutual momentum transfer (OAM) between light field and atoms determines preferred 'bunched' state. Initial atomic positions are random with no preferred scattering mode. In our case atoms are radially trapped at a fixed value of Z with free motion around the resulting ring in the XY plane. The pump light field is represented by a single concentric ring showing the radial intensity profile for $LG_{0\ell}$ OAM modes as described in 4.1

The cold atom distribution is composed of a ring confined to a fixed radius in the XY plane. The pattern formation potentially enhancing a favoured scattered OAM field mode would be described by an azimuthal density modulation of the ring distribution

in a similar manner to the CARL process where density modulations evolve along the Z axis.

We again consider the atomic grouping as a collection of point scatterers consistent with our model assumptions described in section 2.1. Using the accepted scalar model for dipole-dipole coupling taking into account interference effects we assume a single scattering interaction between the pump and the atomic distribution. We apply the Laguerre Gaussian field profile which applies to the Rabi term, $\Omega(r)$, which is proportional to the pump field amplitude. Applying the OAM field profile to our model in the Rabi term component based on our existing equation 3.16 derivatives of complex dipole amplitudes are described by the equation [72],

$$\begin{aligned}\frac{\partial\beta_j(t)}{\partial t} = &\left(\mathrm{i}\Delta - \frac{\Gamma}{2}\right)\beta_j - \mathrm{i}\Omega_0(\mathrm{L}_n^{|\ell|})\frac{1}{w_0}\left(\frac{\sqrt{2}r_j}{w_0}\right)^{|\ell|}\exp\left(\mathrm{i}\ell\Phi_j - \frac{r_j^2}{w_0^2}\right)\\ &- \frac{\Gamma}{2}\sum_{l\neq j}^{N}\beta_l\frac{\exp(\mathrm{i}k_0\left|\mathbf{r_j}-\mathbf{r_l}\right|)}{\mathrm{i}k_0\left|\mathbf{r_j}-\mathbf{r_l}\right|}.\end{aligned} \tag{4.1}$$

For simplicity we will consider interactions occurring in the XY profile perpendicular to the pump field propagation as shown in 4.1. The field component of the Rabi term follows the normal radial profile for a $LG_{0\ell}$ with a dependency on the radius from the Z axis of the field. Φ is the azimuthal angle for any given atom in the XY plane. $\mathrm{L}_n^{|\ell|}$ is the generalised Laguerre polynomial of order n and degree ℓ. w_0 is the pump field $1/e$ waist, position relative to which determines the amplitude of the LG mode. For our purposes we have a system of N dipoles with complex coherence β_j, position r_j, initial condition $\beta_j(0) = 0$ and Γ the state linewidth defined in section 1.6, Ω_0 is

the peak Rabi value based on the pump field maximum amplitude.

Similar to the example of a matrix/vector representation given in 3.1 we can generate a set of N coupled equations for a population of N dipoles based on 4.1. For simplicity we show an example based on 2 dipoles, again A_{jl} represents the final term in equation 4.1.

$$\begin{pmatrix}\dot{\beta}_1\\ \dot{\beta}_2\end{pmatrix} = \begin{pmatrix}\left(\mathrm{i}\Delta - \frac{\Gamma}{2}\right) & A_{12}\\ A_{21} & \left(\mathrm{i}\Delta - \frac{\Gamma}{2}\right)\end{pmatrix}\begin{pmatrix}\beta_1\\ \beta_2\end{pmatrix} = \begin{pmatrix}\mathrm{i}\Omega_0(\mathrm{L}_n^{|\ell|})\frac{1}{w_0}\left(\frac{\sqrt{2}r_1}{w_0}\right)^{|\ell|}\exp\left(\mathrm{i}\ell\Phi_1 - \frac{r_1^2}{w_0^2}\right)\\ \mathrm{i}\Omega_0(\mathrm{L}_n^{|\ell|})\frac{1}{w_0}\left(\frac{\sqrt{2}r_2}{w_0}\right)^{|\ell|}\exp\left(\mathrm{i}\ell\Phi_2 - \frac{r_2^2}{w_0^2}\right)\end{pmatrix}. \tag{4.2}$$

In cases considering pattern formation of atoms and bound states we are working in timescales of the order of the inverse of the recoil frequency, ω_r^{-1}. Again for the 2 level atom in our model we are using the D2 transition of ^{87}Rb. Therefore we have a value for the recoil frequency, ω_r of $\hbar k^2/2m$. Consistent with our assumptions listed in section 2.1.1 the time derivative of the atomic coherences will be taken as zero as the states reach equilibrium in the timescale of Γ^{-1} which is negligible in comparison to the timescales of relative atomic motion for this model. The atomic coherence, β_j, represents the internal degree of freedom resulting from the induced atomic dipole interaction with the field. As described we can consider these internal degrees of freedom at equilibrium and use this adiabatic approximation for our calculations. Such that the set of N coupled equations 4.1 are equal to zero.

We are now in a position to further develop our full dynamic cooperative model further and apply force and resulting position data to simulations as described including

OAM in the pump field.

4.1.1 Optical Forces Produced by Beams Possessing OAM

Under our approximations of a single plane where the pump field interacts with our atomic distribution as described and consistent with accepted theory presenting the quantum derivation of the CDM [24] of the field atom interaction Hamiltonian in this case takes the form,

$$H_I = \frac{\hbar}{2}\sum_{j=1}^{N}\Big[\hat{\sigma}_j\Omega_j(r)\exp\{\mathrm{i}(\Delta_0+\ell\Phi_j)\}+h.c.\Big], \tag{4.3}$$

Considering our assumptions and timescales within the derivation of equation 4.1 in the two level atom case $\hat{\sigma}_j$ can be represented by the complex dipole amplitude value β_j [58]. We can consider the adiabatic approximation described earlier in this section in which the dipole relaxation time is negligible such that the LHS term of equation 3.1 is equal to zero. In which case $\beta_j = \alpha\Omega_j(r)$. If we consider the resulting force equation 3.18 and for the moment we will consider only the single atom field component which will require further calculation due to transverse variation of the Rabi term.

$$\langle \mathbf{F}(r_j)\rangle = -\frac{\hbar}{2}\Big(\alpha^*\Omega_j^*\nabla_{\mathbf{r}}\Omega_j + h.c.\Big). \tag{4.4}$$

From stationary solutions to the 2 level Bloch equations, the normalised atomic

polarisability, $\alpha = 1/(\Delta + i\frac{\Gamma}{2})$ and making use of gradient operator identities the force equation can be written in a form corresponding to our earlier description of optical forces in section 1.4. Expanding equation 4.4 for the instantaneous force we have,

$$\mathbf{F}(r_j) = -\frac{\hbar}{(\Delta_0^2 + \frac{\Gamma}{4})}\left[\left(\Delta_0 - \mathrm{i}\frac{\Gamma}{2}\right)\Omega\nabla\Omega^* + \left(\Delta_0 + \mathrm{i}\frac{\Gamma}{2}\right)\Omega^*\nabla\Omega\right]. \tag{4.5}$$

Using the identities $\Omega\nabla\Omega^* + \Omega^*\nabla\Omega = \nabla(\Omega\Omega^*)$, $\Omega\nabla\Omega^* - \Omega^*\nabla\Omega = \Omega^2\nabla\left(\frac{\Omega^*}{\Omega}\right)$ and where we apply the simplification $\Omega = |\Omega|\exp(\mathrm{i}\phi)$ we can retrieve this final single atom and field interaction force equation expressed with radial and azimuthal derivative terms,

$$\mathbf{F}(r_j) = -\hbar\left(\frac{\Delta_0}{\Delta_0^2 + \frac{\Gamma^2}{4}}\right)\nabla\left|\Omega_j(r)\right|^2 + \frac{\hbar\Gamma}{(\Delta_0^2 + \frac{\Gamma^2}{4})}\left|\Omega_j(r)\right|^2\nabla\Phi. \tag{4.6}$$

We can see two contributions to the resultant force experienced by a two level atom in a light field shown in equation 4.6. These forces correspond to the dipole force, $\mathbf{F}_{dipole}$ proportional to the intensity gradient and the inverse of the detuning and the second term is the scattering force, $\mathbf{F}_{scatter}$ proportional to the phase gradient and the inverse of the square of the detuning.

In order to solve these position dependent equations of motion for cold atom distributions with a weak pump field incorporating OAM for a LG_{nl} pump field as described we need the spatial derivative of the modulus squared of the Rabi term and of the azimuthal phase term.

$$\nabla_{\mathbf{r}} \left|\Omega_j(r)\right|^2 = \Omega_0^2 (\mathbf{L}_n^{\ell})^2 \frac{\partial}{\partial r} \left[\left(\frac{1}{w_0} \left(\frac{\sqrt{2} r_j}{w_0} \right)^{|\ell|} \exp\left\{ \left(-\frac{r_j^2}{w_0^2} \right) \right\} \right)^2 \right] \hat{\mathbf{r}}_j, \tag{4.7}$$

We can develop equation 4.7 in the case of $n = 0$ and various integer values of l ,

$$\nabla_{\mathbf{r}} \left|\Omega_j(r)\right|^2 = \Omega_0^2 (\mathrm{L}_0^{\ell})^2 \left[-\frac{2^{|\ell|+1} \left(\frac{r}{w}\right)^{2|\ell|} \left(2r_j^2 - |\ell| w_0^2\right) \exp\left\{ \left(-\frac{2r_j^2}{w_0^2} \right) \right\}}{w_0^4 r_j} \right] \hat{\mathbf{r}}_j, \tag{4.8}$$

$$\nabla \Phi = \frac{\ell}{r} \hat{\mathbf{\Phi}}_j \tag{4.9}$$

Using solutions to equation 4.7 we are now able to calculate the single atom dipole interaction force for individual atoms and combine with cooperative dipole forces given by equation 3.19 and model dynamics where we have starting positions, Rabi term, detuning, LG mode and beam waist size w_0 and two level atom linewidth.

Now we can express a final force equation for atom j in position r_j where the inter-atomic cooperative term is also reincorporated for other atoms l. Therefore our final force equation which can be used in our model incorporating centre of mass motion as described in section 3.1.2 will be,

$$\mathbf{F}(r_j) = -\hbar\left(\frac{\Delta_0}{\Delta_0^2+\frac{\Gamma^2}{4}}\right)\Omega_0^2(\mathrm{L}_0^\ell)^2\left[-\frac{2^{|\ell|+1}\left(\frac{r}{w}\right)^{2|\ell|}\left(2r_j^2-|\ell|w_0^2\right)\exp\left\{\left(-\frac{2r_j^2}{w_0^2}\right)\right\}}{w_0^4 r_j}\right]\hat{\mathbf{r}}_j$$
$$+\frac{\hbar\Gamma}{(\Delta_0^2+\frac{\Gamma^2}{4})}\left|\Omega_j(r)\right|^2\frac{\ell}{r}\hat{\mathbf{\Phi}}_j$$
$$-\hbar\Gamma\mathrm{Im}\left[\sum_{l\neq j}^{N}\hat{\mathbf{r}}_{jl}\left(\frac{\exp(\mathrm{i}k_0\left|\mathbf{r_j}-\mathbf{r_l}\right|)}{\left|\mathbf{r_j}-\mathbf{r_l}\right|}+\frac{\mathrm{i}\exp(\mathrm{i}k_0\left|\mathbf{r_j}-\mathbf{r_l}\right|)}{k_0\left|\mathbf{r_j}-\mathbf{r_l}\right|^2}\right)\beta_j^*\beta_l\right]. \tag{4.10}$$

4.2 Azimuthal Bunching of Atoms Due to Cooperative Scattering of Light Possessing OAM

4.2.1 Emergence of Azimuthal Bunching

For this study [44] we used an initially circular ring of atoms in the XY plane as in 4.1, located at the maximum mode intensity. It is useful in this case to use the same cylindrical coordinates adopted in the resulting paper [44] i.e. at $\rho = \rho_{\max}$, where $\rho_{\max} = \omega_0\sqrt{\ell/2}$ is the tranverse radius of this intensity peak as can be determined from the transverse profile of an $LG_{0\ell}$ light field. The initial position of atoms is an even distribution along the entire circumference of this maximum. Again as was referenced in section 3.2 in order to neglect quantum effects in the atomic motion is that the superradiant rate $\Gamma_{k'}$ which will be associated with a particular scattering mode must be larger than the appropriate recoil frequency. In the OAM case the azimuthal recoil frequency [44],

$$\omega_\phi = \frac{\hbar k_\phi^2}{2m} = \frac{\omega_r}{k_0^2 \rho^2}, \tag{4.11}$$

where consistent with terms defined in the application of an OAM field to atoms distributed in a ring formation in the XY plane, for which we can define the azimuthal wavenumber, $k_\phi = \sqrt{2}/w = 1/\rho$. This can now be applied to the superradiant scattering rate, $\Gamma_{k'}$ as defined in section 2.1, in the case of a pump with OAM.

We have looked at simulations containing 20-30 atoms in this ring formation with weak OAM pump where the azimuthal mode number, ℓ has been set at values between -10 and 10 and calculated the evolution of the azimuthal bunching term [44];

$$\mathrm{B}_n = \frac{1}{N} \sum_{j=1}^{N} e^{in\Phi_j} = |\mathrm{B}_n| e^{i\psi_n}. \tag{4.12}$$

We are then able to look for patterns in timescales based on several recoil periods $\omega_{\mathbf{r}}^{-\mathbf{1}}$. We are interested in position dependent dynamic development of instabilities which in this case show a relationship to the field azimuthal mode number. The detuning, peak Rabi frequency, cut-off value ($k_0\epsilon$), ring radius, number of atoms all have a bearing on interaction strength and the emergence of any patterns. We have chosen a smaller Rabi term and larger detuning for these simulations over longer timescales. We have maintained the cut-off value of $k_0\epsilon = 0.1$. The following results show that the field azimuthal mode number can correspond to the initially dominant bunching mode. Results are shown for two sample values of ℓ displaying atomic positions and dynamic development of bunching modes. Figures include a snapshot of atomic positions on the circular ring at a time which demonstrates the emergence of the dominant bunching mode compared to other modes and corresponding grouping is

observable.

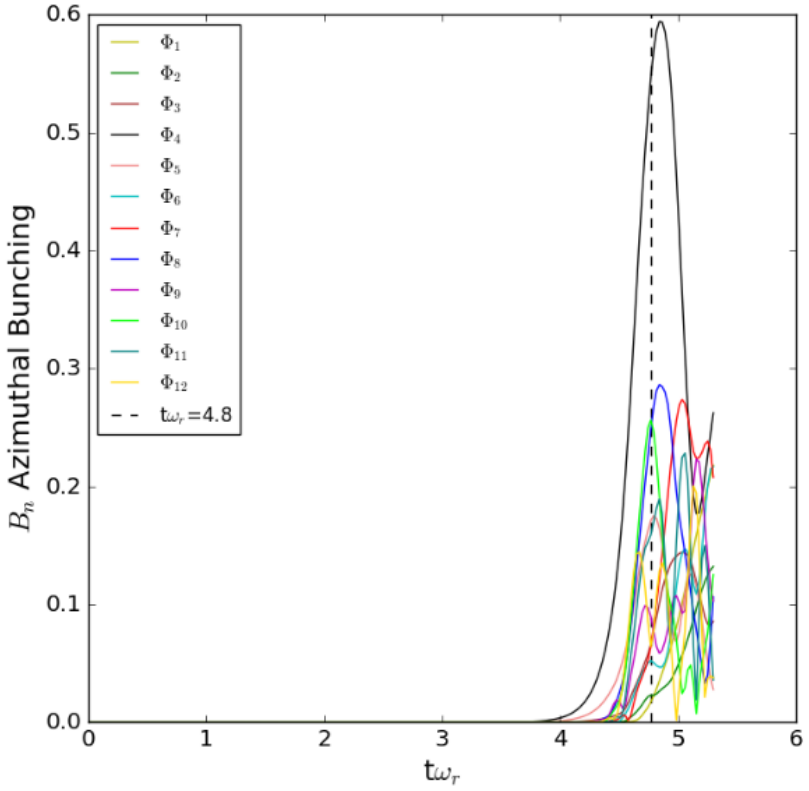

Figure 4.2: $\omega_0/\Gamma = 0.1\Delta/\Gamma$=-750, l=+4, 22 atoms in a trapped fixed ring, radius $\approx$ 4.0λ.

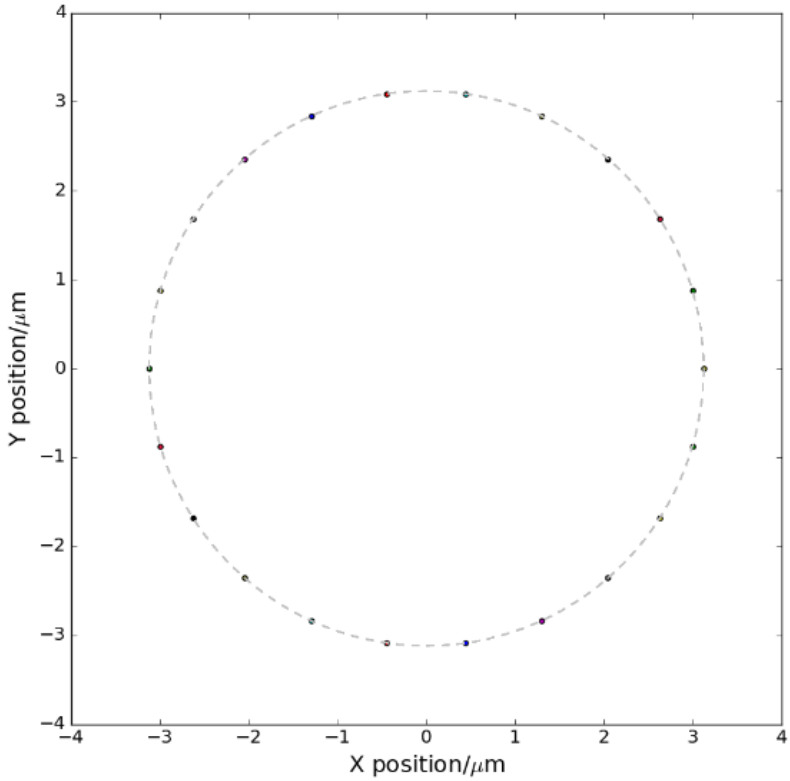

Figure 4.3: $\omega_0/\Gamma = 0.1\Delta/\Gamma$=-750, l=+4, $t\omega_r$=0.0.

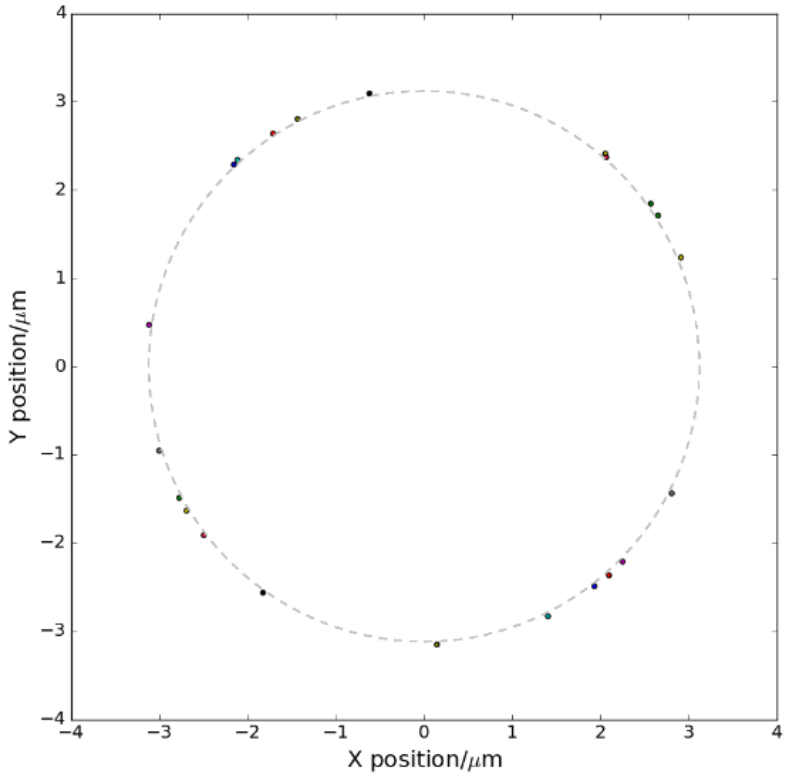

Figure 4.4: $\Omega_0/\Gamma = 0.1\Delta/\Gamma$=-750, l=+4, t$\omega_r$=4.8.

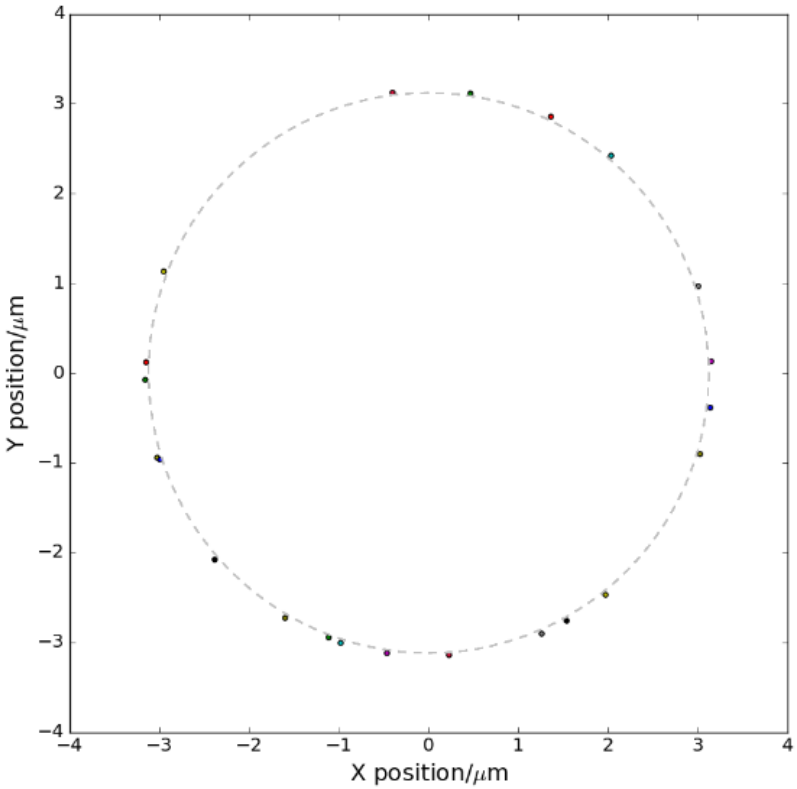

Figure 4.5: $\Omega_0/\Gamma = 0.1\Delta/\Gamma$=-750, l=+4, t$\omega_r$=5.3.

Evolution of $|B_n|$ for modes 1-12 for given resultant field azimuthal mode **l=+4** in 22 atom ring distribution. In each case the cut-off value $k_0\epsilon$ is 1.25. 4.2 shows the time evolution of the azimuthal bunching term for modes 1-12 showing a value of $t\omega_r$ where the first emergent mode looks to be dominant. Then we have a time series from the initial postion of atoms, 4.3, to atomic positions at a time where the dominant bunching term should be evident, 4.4, to final positions in which bunching becomes more mixed, 4.5.

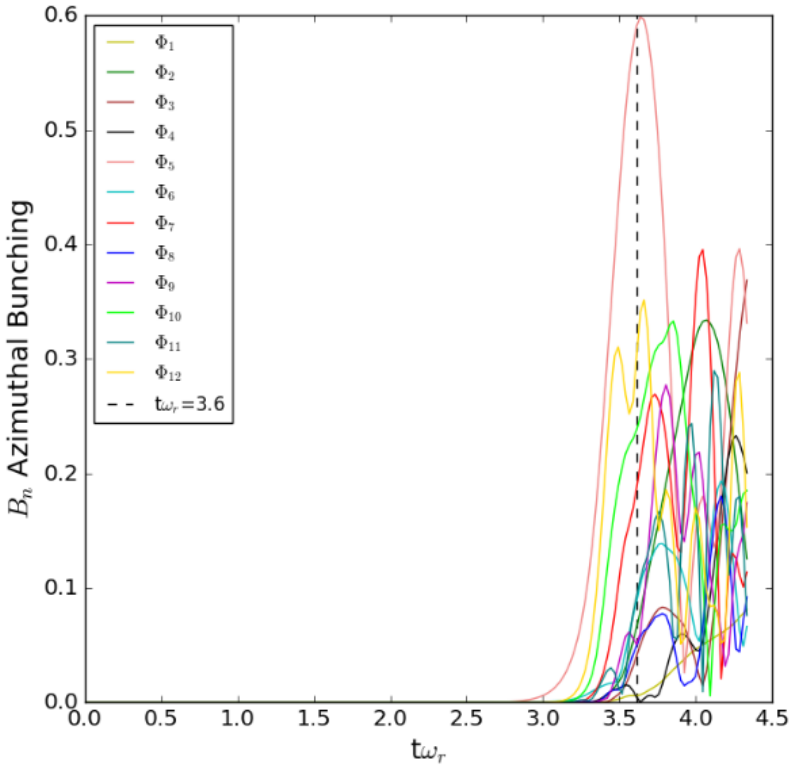

Figure 4.6: $\Omega_0/\Gamma = 0.1\Delta/\Gamma$=-750, l=-5, 22 atoms in a trapped fixed ring, radius $\approxeq$ 4.0λ.

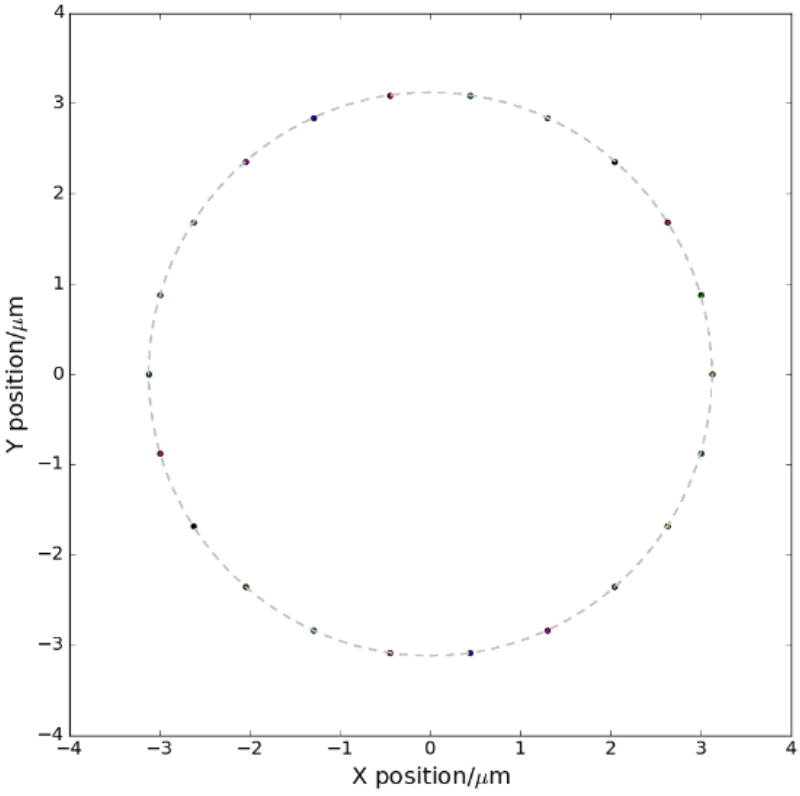

Figure 4.7: $\Omega_0/\Gamma = 0.1\Delta/\Gamma$=-750, l=-5, $t\omega_r$=0.0.

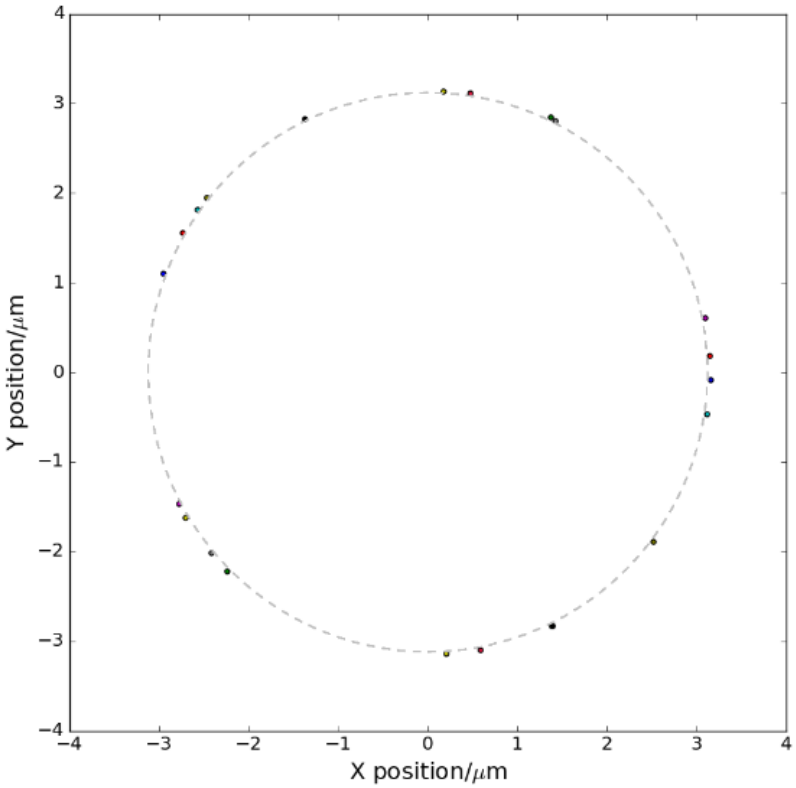

Figure 4.8: $\Omega_0/\Gamma = 0.1\Delta/\Gamma$=-750, l=-5, t$\omega_r$=4.8.

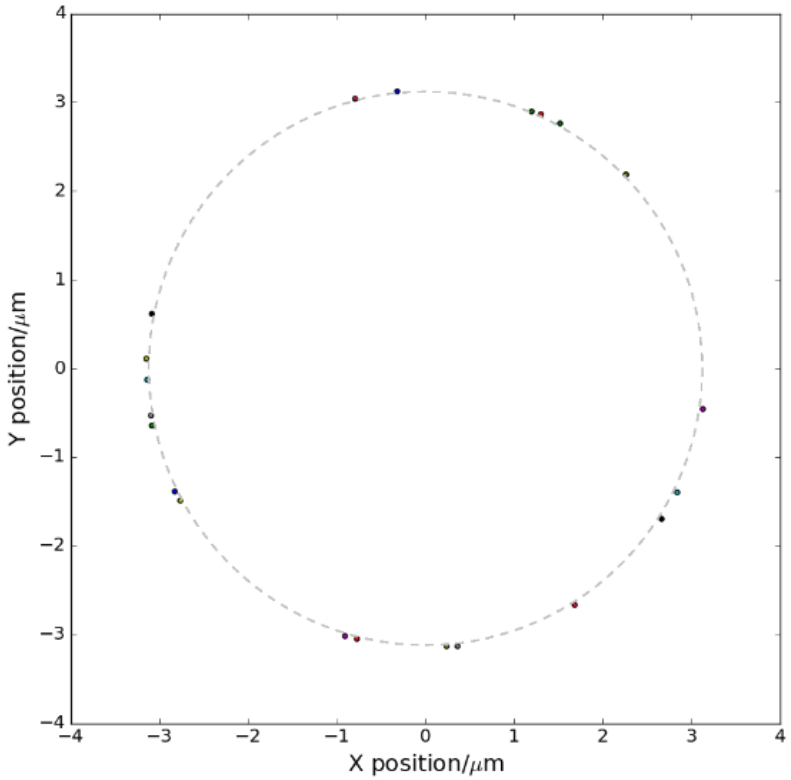

Figure 4.9: $\Omega_0/\Gamma = 0.1\Delta/\Gamma$=-750, l=-5, t$\omega_r$=5.3.

Evolution of $|B_n|$ for modes 1-12 for given resultant field azimuthal mode l=-5 in 22 atom ring distribution. In each case the cut-off value $k_0\epsilon$ is 1.25. 4.6 shows the time evolution of the azimuthal bunching term for modes 1-12 showing a value of $t\omega_r$ where the first emergent mode looks to be dominant. Then we have a time series from the initial postion of atoms, 4.7, to atomic positions at a time where the dominant bunching term should be evident, 4.8, to final positions in which bunching becomes more mixed, 4.9.

It is important to distinguish for the simulations illustrating the emergence of bunching described here we consider that the atoms would be trapped at a fixed radius in the XY plane with free azimuthal motion consistent with simulations used in [44]. The relationship between the initial development of a dominant azimuthal bunching mode n (within bunching term B_n) and field azimuthal mode number ℓ shown in figures 4.2 through to 4.9 results have been reproduced for multiple field modes from l=-10 to l=+10. The apparent distinctive behaviour is that the first azimuthal bunching term to emerge, B_n corresponds to $n = |\ell|$ where ℓ is the azimuthal mode number of our counterpropagating pump field. The cut-off value based on the small parameter ϵ defined in equation 2.19 corresponds to around 0.2 of a wavelength which is consistent with the assumptions made in using the scalar model. There may be options to investigate further with model development to accommodate more atoms, adjustment of size and shape of the atomic distribution and variation within limits of the cut-off value.

This collaborative research and resulting paper [44] consisting of results from a CARL based model confirmed by results from our fully cooperative model presented here show superradiant scattering of an optical field possessing OAM. The cold atom

distribution has been a trapped ring transverse to the pump field direction such that only azimuthal motion is permitted. The evolution of the scattered field has a dependency on the emergence of azimuthal modes. This was explained further in our paper where the established relationship between directional scattered field intensity in the plane of the trapped atomic ring and OM, M is derived further to show the relationship with azimuthal bunching modes, Φ_{m}.

We observe that, if $\rho = w/\sqrt{2} = 1/k_\theta$, the torque on the j-atom is proportional to the angular recoil frequency $\omega_\theta = \hbar k_\theta^2/2m$ rather than to the recoil frequency ω_r. When ρ_j is constant OM can be written as

$$M(\theta) = \frac{R(\rho)}{N}\sum_{j=1}^{N} e^{-ik_0\rho\cos(\theta-\phi_j)+i\ell\phi_j} = R(\rho)\sum_{m}(-i)^m J_m(k_0\rho)\Phi_{m-\ell}e^{im\theta}, \tag{4.13}$$

where

$$\Phi_n = \frac{1}{N}\sum_{j=1}^{N} e^{-in\phi_j} \tag{4.14}$$

It was shown that a regular distribution of atoms throughout the ring becomes unstable when illuminated with a far-detuned optical pump field. This instability evolves exponentially typical of superradiant mode development [44]. The resulting rotation of the gas can be seen to favour particular bunching modes dependent on the pump OAM index, ℓ, and the fixed ring radius, ρ. An extension to the work here is a relaxation of some of the assumptions used, e.g., the restriction to solely azimuthal dynamics to include also radial and even longitudinal dynamics to describe more complex spatial structures, and the extension to include polarization effects, as was done for CARL in [73]. This would allow study of interactions involving exchange of

both OAM and SAM. Additionally, extension from cold, thermal gases to quantum degenerate gases opens up possibilities for new methods for creation of vortices and persistent currents in BECs, in addition to those described in [74, 75].

4.2.2 Collective Rotation of an Atomic Ring

Further to results from 4.2.1 which indicate some variation in resultant azimuthal forces with the cooperative term as evident from equation 4.10 accounting for the differences. In the course of running few atom simulations generally considering rotationally symmetric two dimensional distributions it was observed that the resultant force on the component atoms of the distribution would be consistent in size and direction corresponding to either clockwise or anti-clockwise torque, attractive or repulsive forces from the centre or a combination of tangential and radial components. Specifically measuring the resultant collective interatomic dipole forces, given by the second term in equation 3.18, for regular ring distributions gives examples of this effect. Figures 4.10 to 4.13 demonstrate this in the three atom case where the radius of the ring is varied. This is consistent with figure 4.1 however, in these cases we will not apply an annular trap and atoms will have free motion in the XY plane.

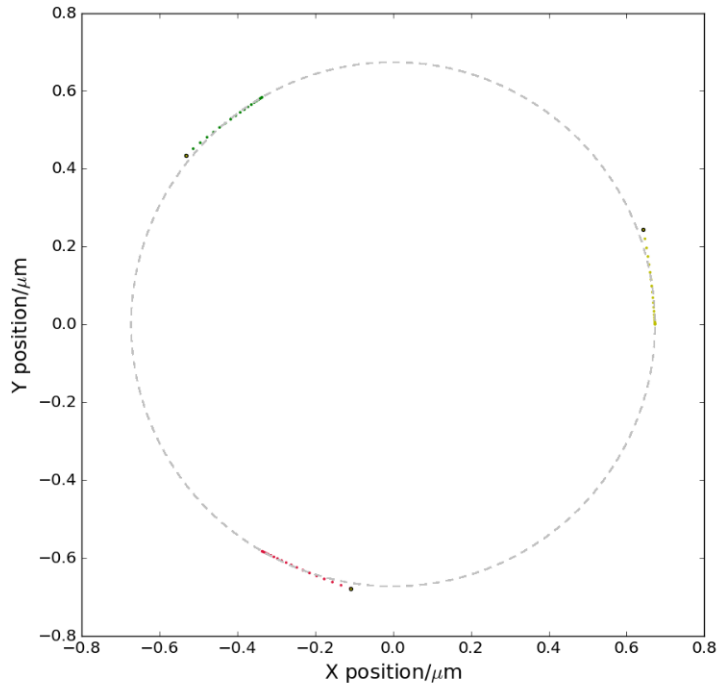

Figure 4.10: Δ/Γ=-200, Ω_0/ω_r=0.8, initial adjacent separation $\approxeq 1.49\lambda$.

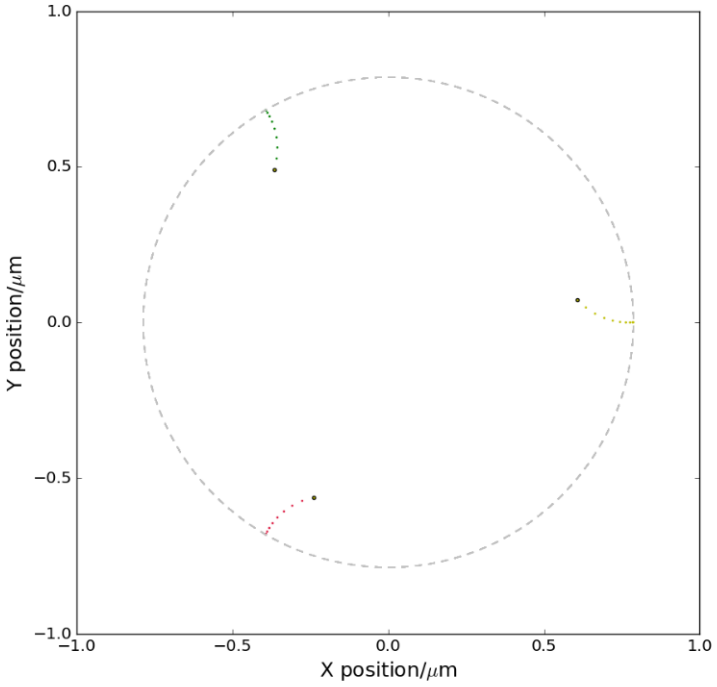

Figure 4.11: Δ/Γ=-200, Ω_0/ω_r=0.8, initial adjacent separation $\approxeq 1.75\lambda$.

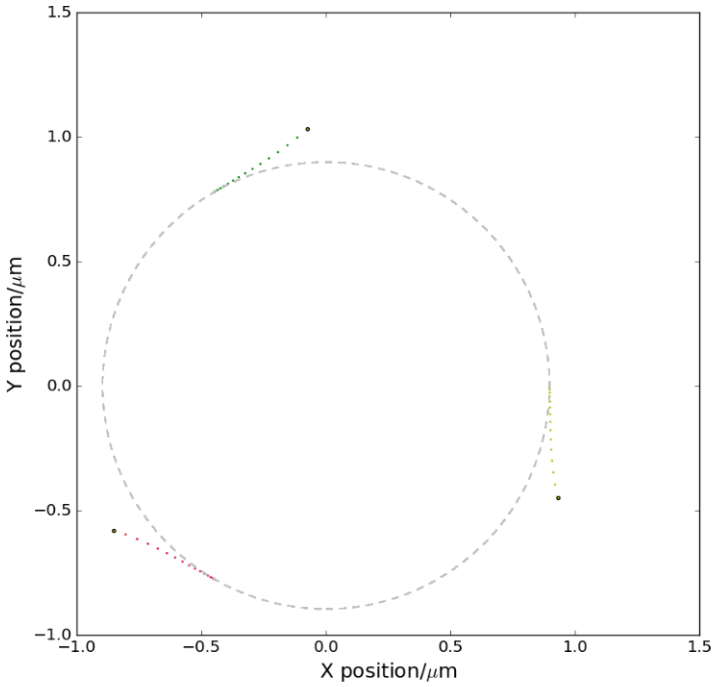

Figure 4.12: Δ/Γ=-200, Ω_0/ω_r=0.8, initial adjacent separation $\approxeq 1.99\lambda$.

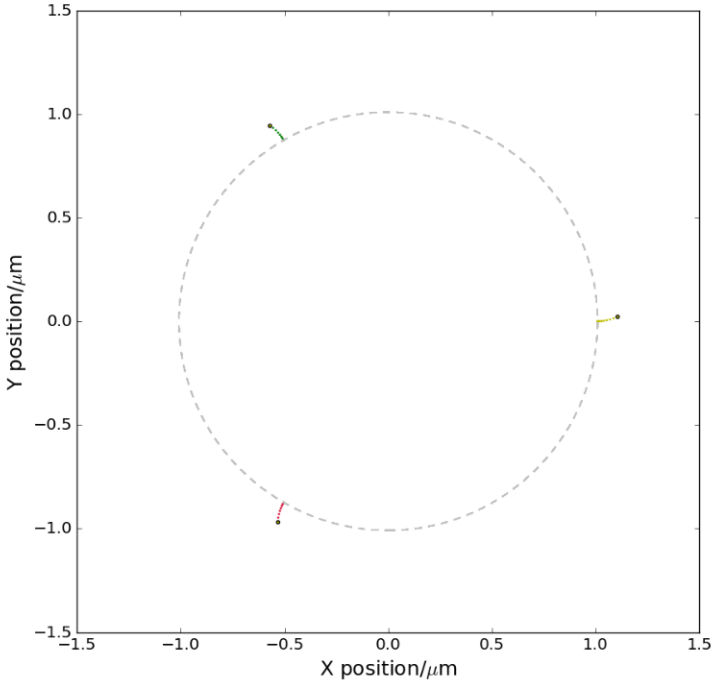

Figure 4.13: Δ/Γ=-200, Ω_0/ω_r=0.8, initial adjacent separation $\approxeq 2.24\lambda$.

This series of figures 4.10 to 4.13 show the evolution of position in the XY plane of 3 atom ring distribution in a weak pump field with OAM of LG0l applied with l =-1. The dashed ring shows the transverse ring intensity peak of the pump field. Position evolution of atoms is shown in a dimensionless time period based on the recoil frequency of $t\omega_r = 0.12$ with the path of atoms shown and the final positions highlighted. Adjacent atomic separation is increased by approximately a quarter wavelength from 4.10 through 4.13. As described we are interested in any patterns of behaviour due to the cooperative second term in 3.18.

Figures 4.10 to 4.13 reference results based on the resultant value of the collective dipole force term (which is much larger than the single atom term in these cases). This is the only force term in equations 4.6 and 3.18 which has a variable response in direction depending on atomic separation. In our case for regularly spaced distributions this results in a consistent torque or radially attractive or repulsive force across the distribution.

In most cases in the absence of cooperative terms it would be expected that rotation of a distribution resulting from OAM in an applied field would be consistent with expected direction of radiation pressure due to the phase gradient in correspondence with the azimuthal mode number [76] (clockwise for a positive value of l) as is evident from equations 4.4 and 4.9. Figure 4.14 demonstrates full simulation results with the same initial conditions apart from atomic separation and shows that resultant rotation can be clockwise or anti-clockwise in cases where the azimuthal mode number of the pump field remains the same.

It should be noted in the case of figure 4.14 the radial oscillation around the circular

dotted line indicating the intensity maximum of the pump field is not necessary. This serves to show we are still in the region of stable optical binding parameters and makes it easier to see the difference in rotation. The effect will still occur with atoms located exactly on ring situated on the intensity maximum.

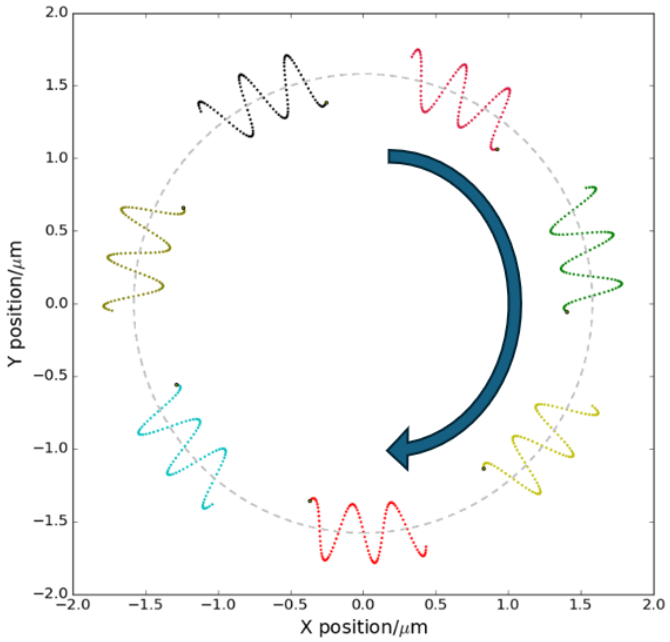

(a) Δ/Γ=-200, Ω_0/ω_r=0.8, initial adjacent separation $\approxeq 1.99\lambda$.

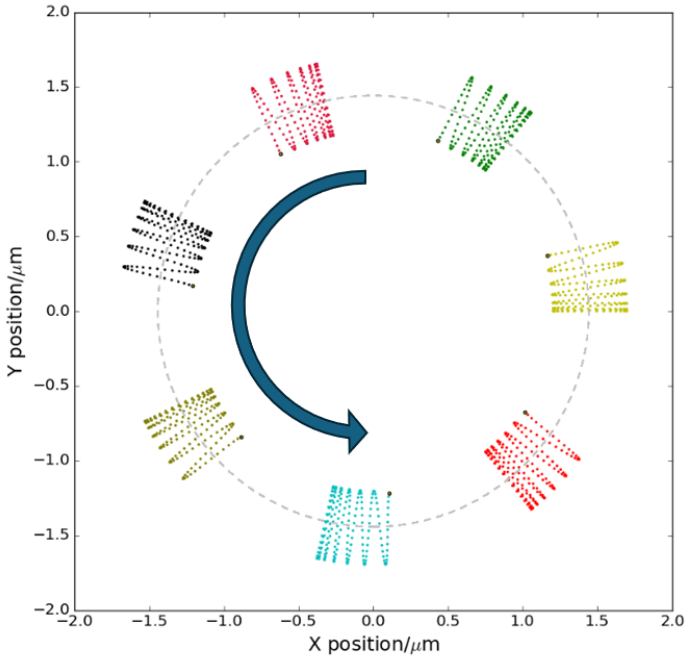

(b) Δ/Γ=-200, Ω_0/ω_r=0.8, initial adjacent separation $\approxeq 1.89\lambda$.

Figure 4.14: Evolution of position in XY plane of 7 atom ring distribution in weak pump field with OAM of LG0l applied with l =-1 in both cases. Dashed ring shows transverse ring intensity peak of the pump field. Position evolution of atoms is shown in excerpts from full simulations for periods of 0.05-0.075ms which equates to around 2 atomic recoil frequency time periods with a highlighted border on final positions. Adjacent atomic separation is larger in (a) other initial conditions are the same. Resultant force is calculated based on all identified interaction forces.

We investigated the scenario when the full force equation 3.18 is applied that we might see rotation due to the OAM carried by the pump field resulting in rotation of the atomic distribution in direction opposite as to what would be expected due to the helical phase profile of the OAM phase front. This would be the simple single atom response to a field with a phase gradient which can be seen in the second term of equation 4.6. This simulation runs within the boundaries of our assumptions but with a much weaker pump field than has been used in other OAM simulations for which we apply a annular trap condition to maintain atoms in their ring formation. We can see that under certain conditions principally dependent on the radius of the ring distribution the cooperative term of the resultant force can be tangential or radial and can result in distribution rotating against the expected direction corresponding to the radiation pressure force due to the phase profile of the wavefront evident from equation 4.6.

4.3 Cooperative Transfer of Angular Momentum Between Two Atomic Rings

The model developed here allows for study of opto-mechanical effects in cold atomic systems including the transfer of momentum between light fields and atomic distributions following particular ordered patterns where the interaction is coherent. We postulate that OAM possessed by one trapped ring of atoms may be transferred to a second ring of trapped atoms by optically mediated forces where the pump light field is a plane wave with no OAM.

We use approximations previously described in section 2.1 for the CDM and 3.1 for

conditions favourable to optical binding.

The simulation in principle follows the initial description of the environment used to demonstrate optical binding shown in 3.1 extended with an additional concentric ring of atoms and for the purposes of this investigation rings would be trapped radially in the XY plane so free to move azimuthally.

In order to investigate if this transfer of OAM is possible between one atomic ring and a second ring purely by optically mediated forces with a plane pump field we investigate optimal ring locations using our model. We find a stable arrangement with evidence of OAM transfer for rings with a radius of a wavelength and around 15 atoms per ring.

The following results will show the dynamic evolution of the position of both rings the inner ring having initial uniform angular velocity for each atom in the ring and the outer ring being stationary relative to the inner ring. We have chosen fixed radius distributions at a radius similar to that used in optical binding simulations and with a seperation distance over which we can see momentum transfer in a timescale in the order of ω_r^{-1} similar to previous simulations.

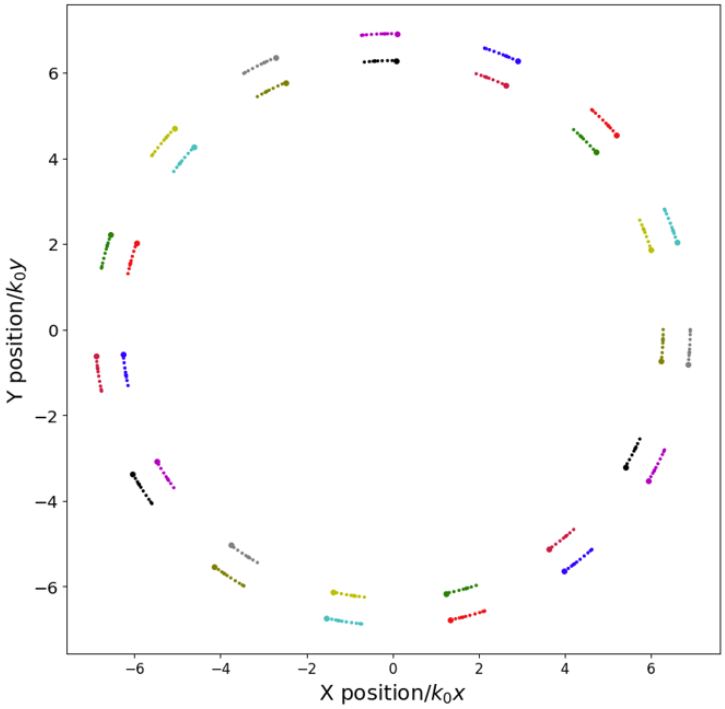

(a) Radius1 = λ, Radius2 = 1.1 λ. The outer ring is initially stationary. OAM is transferred back and forward between rings. Atom positions with paths showing clockwise motion are shown after $\omega_r t = 0.25$ where both rings have shared clockwise OAM.

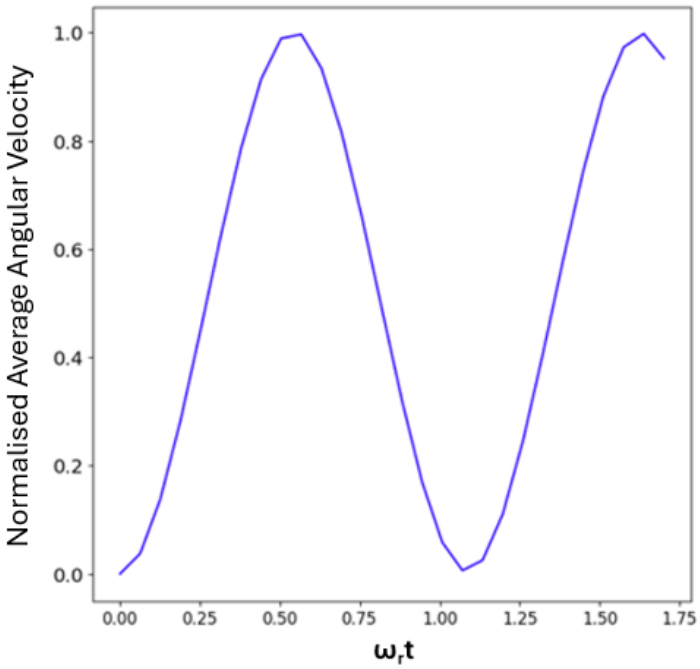

(b) Radius1 = λ, Radius2 = 1.1 λ

Figure 4.15: OAM transfer results showing position and average OAM transfer to initially stationary outer ring normalised to initial OAM of moving inner ring.

This has purposefully been a relatively focused investigation to particularly look at the feasibility and nature of OAM transfer between two rings of atoms trapped in a concentric ring formation with free azimuthal motion on their fixed radii.

In all cases we have shown results for the evolution of the average angular velocity of the outer ring which was initially stationary. This average angular velocity is normalised against the initial average angular velocity of the inner ring. We can see in figure 4.15 that angular momentum is transferred fully between rings in a continuing cycle back and forward.

There is a dependency on the relative radii of the rings for the rate of the transfer as would be expected illustrated by the dependency of the resultant force equation 3.19 on interatomic distances.

This was an area of interest rather than a focus of this research so was not investigated in further detail than confirming the possibility of this momentum transfer.

5 Cooperative Scattering of Amplitude Modulated Light by Cold Atoms

In this chapter we explore the application of partial coherence to the pump field [77]. We look for the emergence of new effects which can be specifically identified as a result of pump modulation.

5.1 Inclusion of Pump Amplitude Modulation

As a stepping stone towards investigating cooperative scattering involving partially coherent or incoherent i.e. thermal/blackbody radiation, we introduce modulation to the pump field in our simulations of cooperative phenomena looking to extend understanding or for opportunities to emulate effects or scenarios seen elsewhere in other fields of physics or the natural world. Specifically we would like to investigate new behaviours in the case of optical binding and CARL further to chapter 3.

We apply a temporal modulation to the pump which will then apply to the Rabi term, Ω, we again use the adiabatic approximation assuming a steady state of the internal degree of freedom setting $\dot{\beta}_j = 0$ in our set of resultant N coupled equations. In the case of amplitude modulation we would have,

$$\Omega_{0(AM)} = \Omega_0(1 + \varepsilon_{AM}(cos(\Phi_{AM}t))), \tag{5.1}$$

where ε_{AM} is the size of the modulation relative to the original pump field amplitude,

Φ_{AM} is the frequency of the sinusoidal amplitude modulation. The sinusoidal intensity modulation defined in 5.1 corresponds in the frequency domain to the presence of two frequency sidebands at frequencies $\omega_0 + \Phi_{AM}$ and $\omega_0 - \Phi_{AM}$.

It was observed and is not unexpected that if simulations are run for times 5-10 times larger of the recoil timeframe period, $\omega_{\mathbf{r}}^{-\mathbf{1}}$ there is evidence of some edge effects involving distortion of pattern formation and increased density at the boundaries of an elliptical distribution where the dimension is in the order of a few wavelengths. Also some particle loss is observed at the end points of the main axis consistent with [36].

It is useful in view of previous results to confirm the parameters which will be used for the investigation of a partially coherent pump field in this section. We decided to use a one dimensional distribution trapped along the Z axis of the pump direction in the order of tens of wavelengths to simplify the model and ensure a consistent cooperative response. This means that almost all atoms have neighbouring atoms on both sides. We use an atomic density similar to that used in section 3.2.1. The set up for this configuration is shown in figure 5.1.

We choose the size of the rear facing optical magnetisation lobe of a type which can be seen in figure 3.12 which emerges during CARL simulations for XY or XZ ellipse distributions and also for 1D distributions along the Y or Z axis as a measure of the strength of the preferred scattering mode associated with CARL. We take a normalised measure of the area of the backscattered lobe for a distribution with an axis along Z.

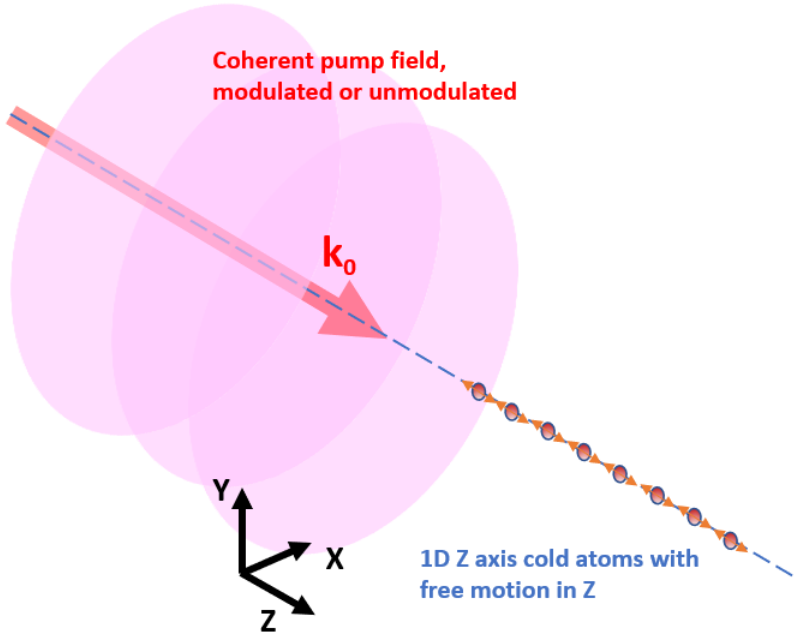

Figure 5.1: Simplified diagram of pump field aligned along Z axis interacting with a cold atom distribution with fixed motion along the Z axis.

5.2 Enhancement of Collective Scattering Due to Amplitude Modulation of Pump Field

We want to be consistent with models used for multi-mode CARL findings where our model has proven to agree with published results [36] as demonstrated in section 3.2.1 so we choose a 1D Z axis distribution shown in figure 5.1 with inter atomic distances and dimensions on an equivalent scale. Therefore for these simulations we have 200 atoms regularly distributed along a distance corresponding to 20 wavelengths of the pump field such that CARL type banding patterns could occur over multiple iterations well within the ends of the distribution. This results in an interatomic

distance of 0.1 of a wavelength. We apply a Rabi term, Ω_0, of 20Γ to the pump field, a detuning value, Δ_0, of -400Γ and a cutoff parameter $k_0\epsilon = 0.05$ corresponding to less than 0.01 of a wavelength.

Simulations were run using different values of the pump modulation frequency Φ_{AM}. The value of the relative amplitude of the modulation, ε_{AM}, is found to be optimal at a value of 0.35 for which we have observed significant changes in the relative size of the normalised rear facing optical magnetisation lobe which can be seen in figure 5.2 where the optimal Φ_{AM} in our simulations can be seen to be $\Phi_{AM} \approxeq 4.0\omega_r$ (where ω_r is the single atom recoil frequency). For context we also show a figure 5.3 using values of Φ_{AM} above and below the value found to be optimal. We will use these stated optimal values and results in assessing pump amplitude modulation impact on the size of the cooperative effect measured using the rear facing optical magnetisation lobe .

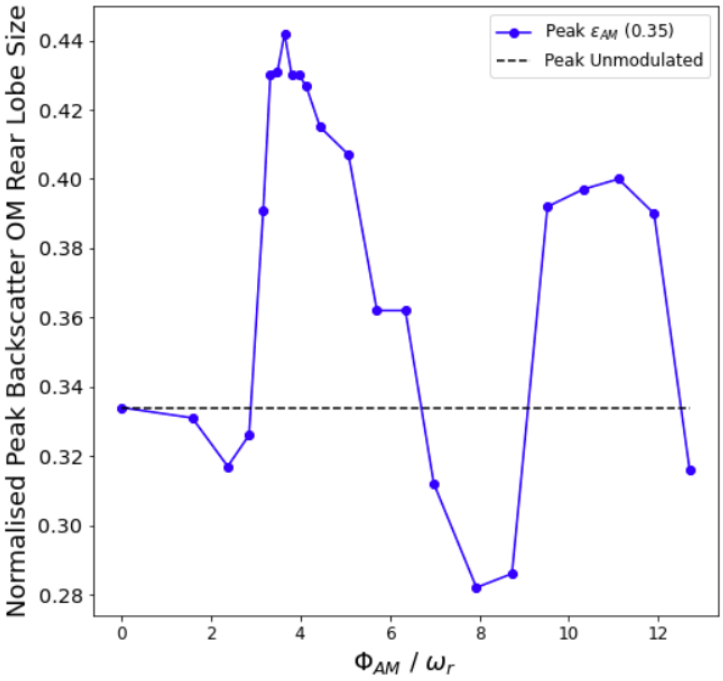

Figure 5.2: Effect of pump AM frequency, Φ_{AM}, variation showing plot of the normalised rear facing OM lobe size for a modulation amplitude, ε_{AM} at an optimal value of 0.35 against a range of modulation frequencies.

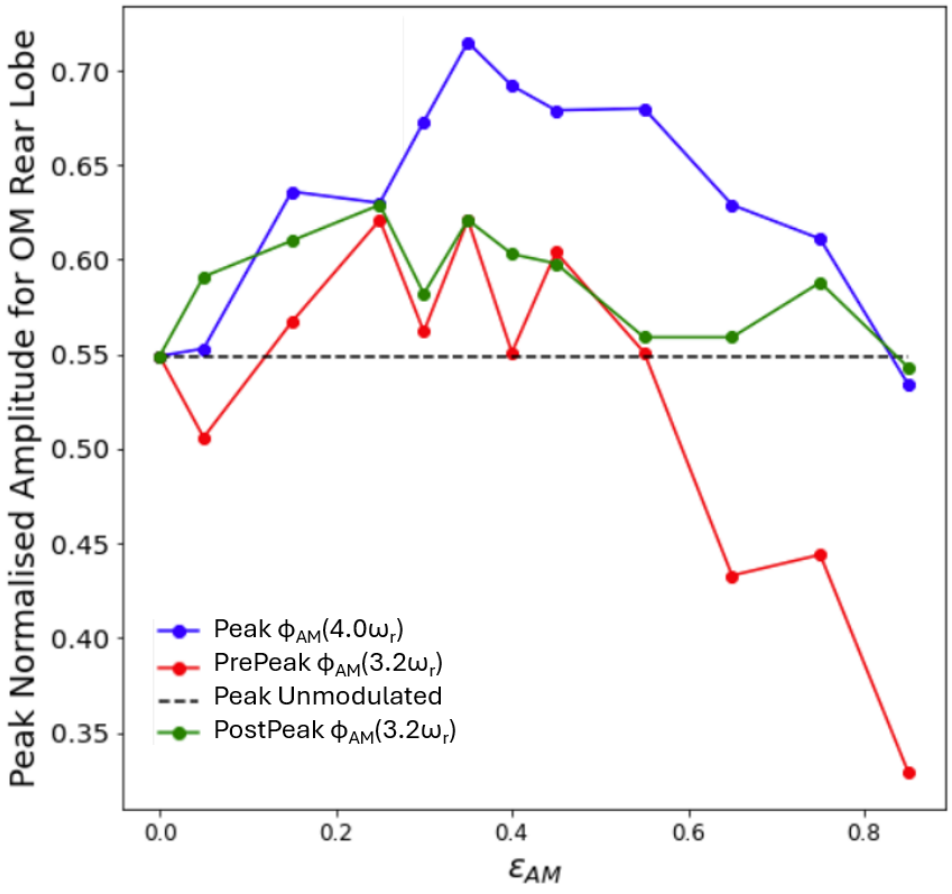

Results with these parameters show consistency with earlier simulations comparing our model with results for a 2D ellipse of atoms shown in 3.12 where lobe size peaks in the region of 1 atomic recoil timescale ($\omega_r t \approxeq 1$). Typically in a single run of results for a single pump frequency as shown in figure 5.4 we will see the lobe size growing exponentially consistent with similar cooperative self-organisation phenomena [78, 79], then declining from an initial peak based on optimal pattern formation to enhance the backscattered field and then varying around a value somewhere below the peak as shown in figure 5.4. This would indicate strong initial pattern formation then some loss of optimal positioning potentially due to many atoms in close proximity, more atoms with momenta outside of the range for optimal interaction with optical potential resonances which will be described further in this section.

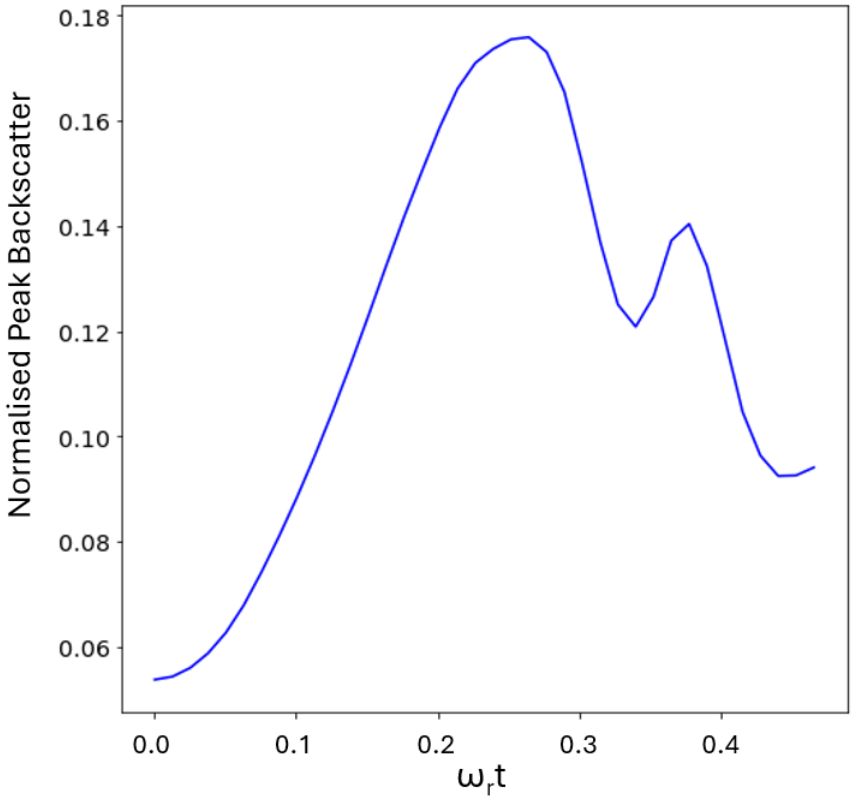

Figure 5.4: Example of the evolution of the amplitude of the rear facing OM lobe size normalised to the forward lobe for an unmodulated pump field consistent with parameters described in this section. We have used Δ /Γ=-400, Ω_0 /Γ=20, $k_0\epsilon$=0.05 for 200 atoms regularly spaced over 20 wavelengths along the Z axis as described by figure 5.1.

The graph shown in figure 5.2 provides a series of results which are consistent in terms of there being a significant increase in the region of around 30% in the size of the rear facing optical magnetisation lobe which we are using as a measure of the size of the cooperative interaction between the pump and the atomic distribution. This variation in the size of the cooperative effect could be consistently observed

with regular or randomly spaced distributions and could also be reproduced with a similarly spaced 2D elliptical XZ atomic cloud. The black dotted line in the graph shows the peak size of the backscattered rear lobe with zero modulation and the blue line plots results for 15 different values of modulation frequencies used for amplitude modulation in our simulations as described in equation 5.1.

Further work is required to determine the nature of the relationship between the frequency used for the amplitude modulation of the pump field and the apparent enhancement of the cooperative backscattered lobe. In the case of the cited example [77] a phase modulated pump produces enhancement of the cooperative effect with a dependency on the relative size of the pump modulation frequency, Φ_{AM} in our amplitude modulation case, compared with a factor known as the collective recoil frequency which we will label, ω_{r-coll}. This is equivalent to atomic recoil frequency, ω_r multiplied by a factor called the CARL parameter, ϱ shown in equation 5.2. The CARL parameter has a dependency on the atomic density, N, the pump Rabi frequency, pump detuning from the atomic transition and the atomic recoil frequency as previously defined in 1.4 and 3.2.1. In the case of the cited work [77] this results in a collective recoil frequency about 40 times larger than the atomic recoil frequency. The CARL parameter is a useful way of demonstrating the potential for cooperative effects to affect an intensive property such as atomic recoil frequency. This particular example has been used in the case where CARL is demonstrated in a cavity environment rather than in an open multimode model such as the one used in the simulations here, however the concept of a collective recoil frequency is useful in hypothesising on these results.

$$\varrho = \left(\frac{\Omega_0 g \sqrt{\mathrm{N}}}{2\Delta_0 \omega_r} \right)^{\frac{2}{3}}, \tag{5.2}$$

where, $g = \sqrt{\frac{\omega_0 d^2}{2\epsilon_0 \hbar}}$ is the atom mode coupling constant.

The finding in relation to enhancement of the cooperative effects in works using phase modulation [77] leading to CARL enhancement makes use of the ratio of modulation frequency to the collective recoil frequency which we will label Ω_m. We will use amplitude modulation show optical potentials due to modulation each of which move with a phase velocity which is proportional to a multiple of the modulation frequency i.e. Ω_m. Therefore there can be resonance with an atom when the atomic momentum meets the condition $p_j \cong \Omega_m$, where we take p_j to represent atomic momenta. For clarity resonances are shown in figure 5.5. This potentially could lead to enhanced momentum diffusion amplifying the response of the distribution again measured by the amplitude of the scattered or probe field.

Our results in terms of a clear amplification of the CARL response using our chosen measure of the size of the rear facing OM lobe indicate an optimal value for the modulation frequency of 4 times the recoil frequency. We can see that values either side of this result in amplification, but the amplification is about three times larger at the optimal value. We would hypothesise a similar relationship as was established in [77] between the modulation frequency and a collective recoil frequency stimulating enhanced interaction between optical potentials with atoms possessing particular momenta represented in figure 5.5. This requires further work as the collective recoil frequency has previously been defined for interactions within a cavity.

it would be useful to present the results shown in 5.2 demonstrating the optimal enhancement of cooperative effects for an amplitude modulated pump in more familiar terms. Our simulation generates position and velocity data for atoms in the distribution throughout the course of the simulations by generating a state vector containing momentum and position 3.18 for a Runge-Kutta 4th order integration method.

If we take the momentum data for the atomic distribution we can calculate the variance of the Z axis momenta for the distribution. This has been plotted for both simulations with no pump modulation and with the optimal pump amplitude modulation shown in figure 5.2 where $\varepsilon_{AM} = 0.35$ and $\Phi_{AM} = 4.0\omega_r$ and the baseline parameters for the pump field are kept the same as described in 5.4. Since the variance measures the spread of the square of the distribution momenta from the mean this gives a value which represents a spread of the square of the atomic velocities which gives us a measurement we can use to be representative of temperature. This is based on the equipartation of energy theory [80] for atoms or molecules in thermal equilibrium in our case considering only the translational degrees of freedom in one dimension along the Z axis,

$$\overline{\mathrm{E}}_K = \frac{1}{2} m \overline{v}_z^2 = \frac{1}{2} \mathrm{kT}, \tag{5.3}$$

where, $\overline{\mathrm{E}}_K$ is the average kinetic energy per atom in the distribution, k is the Boltzmann constant and T is the distribution temperature.

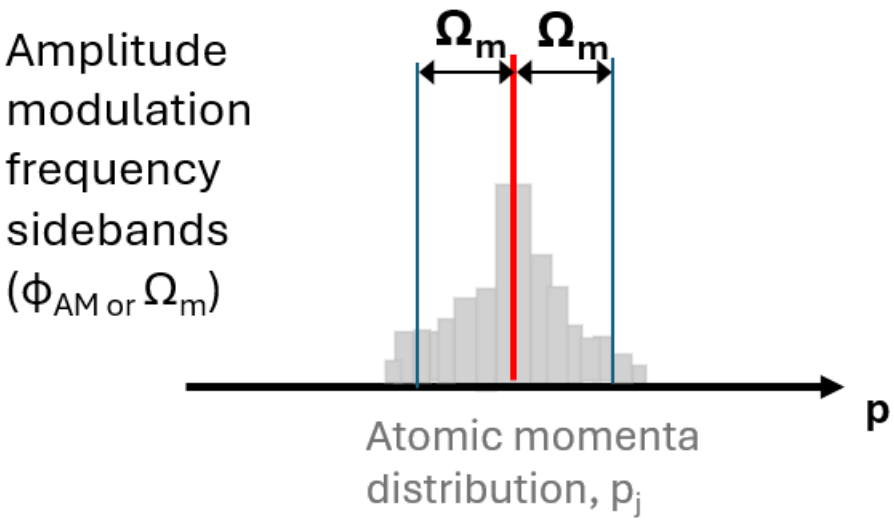

Figure 5.5: Interaction resonance frequency schematic using the same theory as [77] due to optical potentials in this case for amplitude modulation relative to cooperative recoil frequency. This is intended to show the likelihood of resonant interation with atomic momenta under system evolution. An example spread of positive and negative atomic momenta is shown in the initial stages of interaction with the pump field indicating how additional resonant interaction would occur.

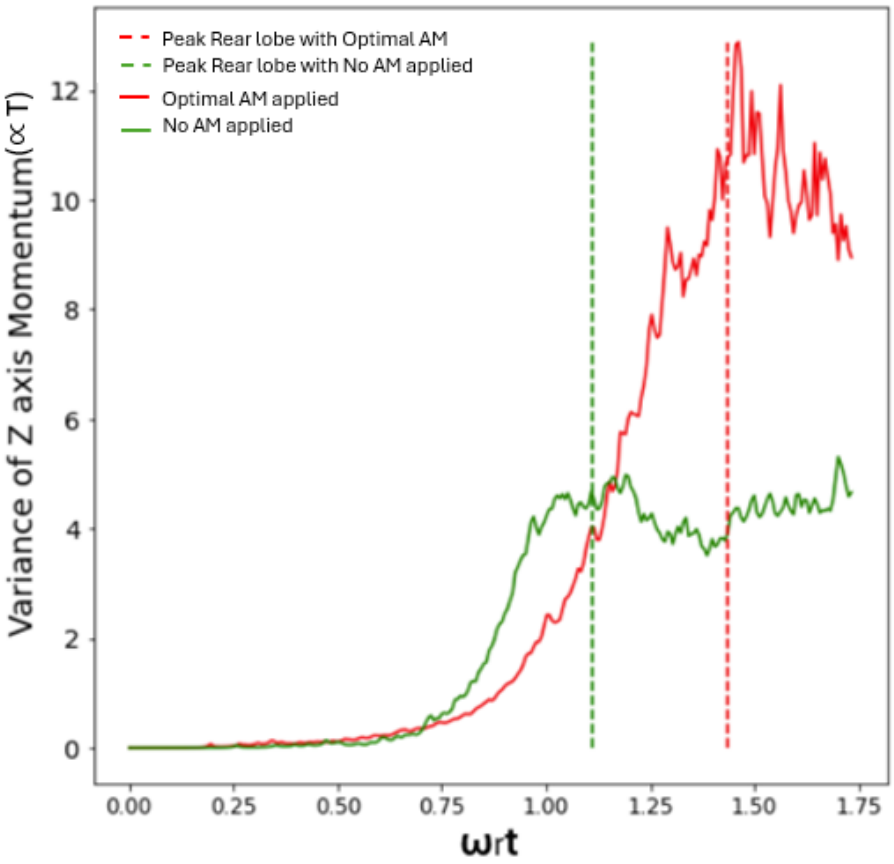

Figure 5.6: Variance of Z axis momentum with and without AM. The dotted lines represent the point in time where our measure of cooperative behaviour the rear OM lobe size reaches its peak. The red line shows Z momenta variance for an amplitude modulated pump and the green line an unmodulated pump with the same parameters described earlier in this section.

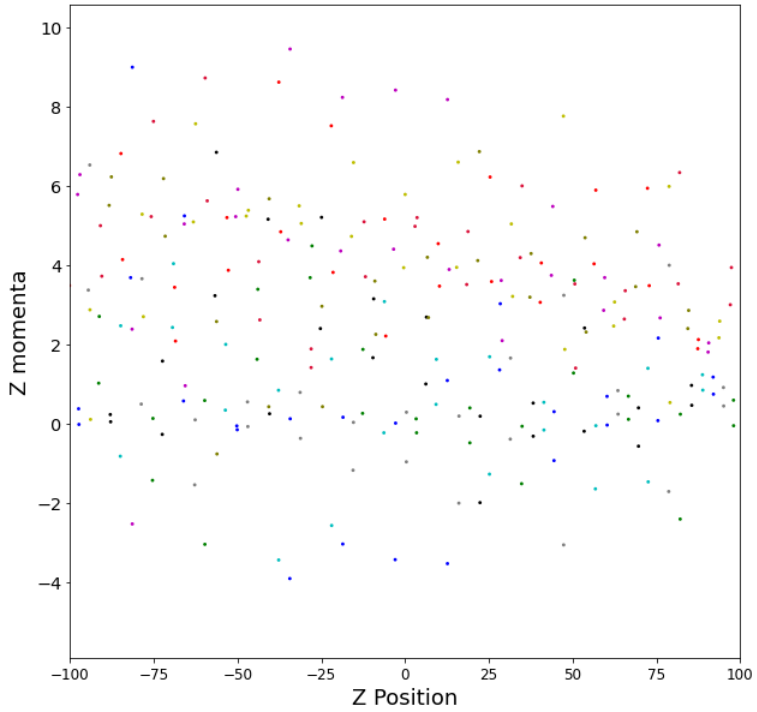

Figure 5.7: Graph showing spread of Z axis momenta against Z axis position for all the atoms in the distribution for optimal amplitude modulation at time of $\omega_r t = 1.29$ close to peak rear lobe with Optimal AM shown in fig 5.6.

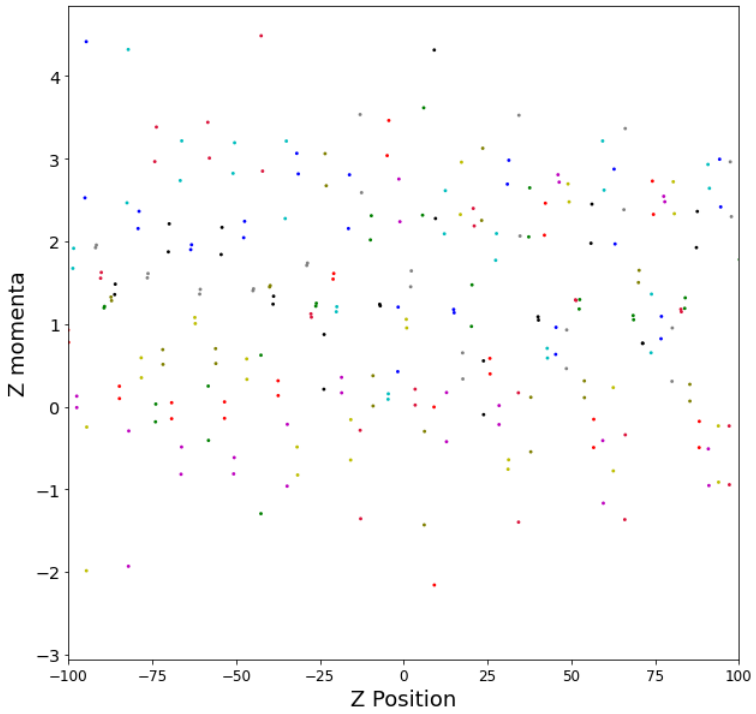

Figure 5.8: Graph showing spread of Z axis momenta against Z axis position for all the atoms in the distribution for optimal amplitude modulation at time of $\omega_r t = 0.99$ close to peak rear lobe with no AM shown in fig 5.6.

The results shown in 5.6 provide a comparison between an unmodulated pump field and an amplitude modulated pump field which we postulate is responsible for an enhancement of the cooperative effect. One of the factors which demonstrates the enhanced effect is the temperature which we represent by using the variance of the Z axis momentum throughout the simulation. We can see there is an increase of 250-300% in this measure corresponding to the point in the simulation where the peak rear facing optical magnetisation lobe is recorded which we have identified as an effective measure of the size of the cooperative effect. The dotted lines indicate the point in both the modulated and unmodulated pump simulations where the peak rear facing optical magnetisation lobe occurs which also seems to indicate that our variance of momenta measurement tends to correspond with the size of the cooperative effect as suggested.

It is helpful to consider the results graph 5.6 in tandem with the corresponding graphs 5.7 and 5.8 which show all the atoms in the distribution with their Z axis momenta plotted against their Z axis position which provides a clearer picture of what is happening to individual atoms during these simulations. A physical representation of the initial environment is given in figure 5.1.

As expected there are momentum shifts due to cooperative effects in both positive and backward directions compared to the pump direction as the cooperative forces are dominant compared to the single atom forces consistent with the regimes chosen for optimal cooperative action demonstrated in 3.2.1. The following graphs help to demonstrate the banding nature consistent with cooperative CARL pattern formation showing the spread of atomic momenta along the Z axis.

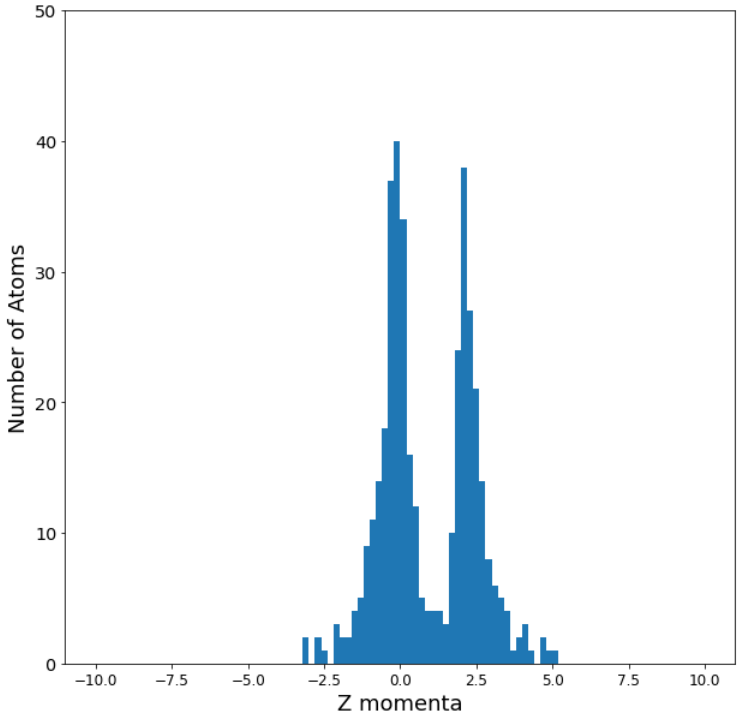

Figure 5.9: Graph showing distribution of Z atomic momenta for all the atoms in the distribution for optimal amplitude modulation at time of $\omega_r t = 0.5$ where momenta spread and banding can be seen.

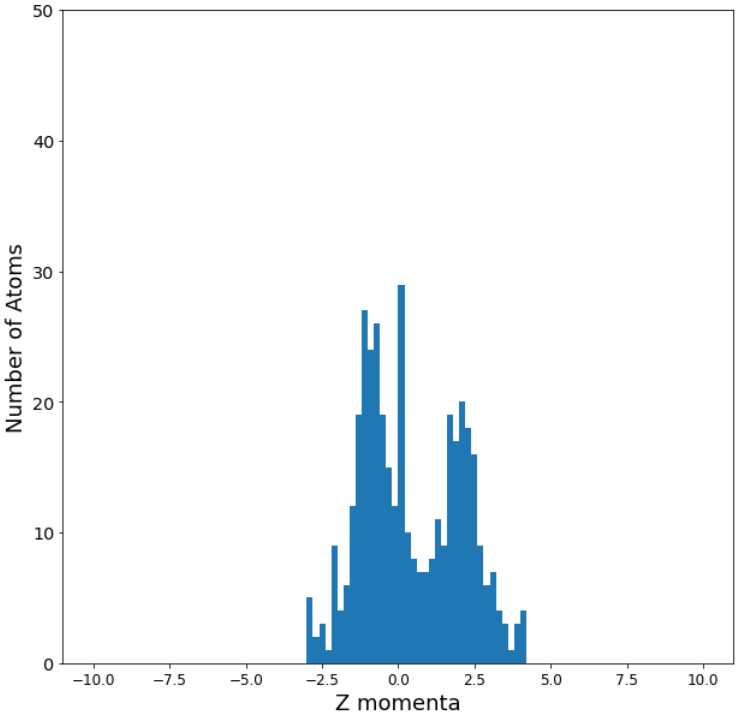

Figure 5.10: Graph showing distribution of Z atomic momenta for all the atoms in the distribution for an unmodulated pump field at time of $\omega_r t = 0.5$ where momenta spread and banding can be seen.

Due to the cumulative nature of the cooperative momentum exchange term applicable in the CARL model here given in equation 3.25 and some variation in cumulative effects approaching the edge of the distribution there is a spread in atomic momenta bandings and therefore the pattern formation which is evident in figures 5.7 and 5.8 which are intended to demonstrate the relative size of the cooperative effect.

We can however give a clearer picture of the momenta evolution of atoms showing the favoured momenta states in this simulation corresponding to the pattern formation and cooperative nature of CARL using the following graphs, figures 5.9 and 5.10 of momenta distribution for both modulated and unmodulated pump fields consistent with the theory described in section 1.7.

6 Conclusions and Further Work

The aim of this work was to extend our understanding of cooperative effects using the CDM theory of interactions between light and atomic distributions. We also wanted to extend our model outside the normal boundaries of cold atom research to include consideration of non-monochromatic light including modulated pump fields seeking evidence of effects which may become apparent for a broadband pump field where research into or comparison with naturally occurring phenomena is more likely.

Our coupled dipole theory based model is semi-classical using a scalar light field working within appropriate approximations which are detailed in section 2.1. After confirming signature results for cooperative phenomena such as superradiance from our model against published research, a subset of our results are provided in section 2.3.1. We then looked to extend work to include centre of mass motion. This allows simulations to develop into the areas of CARL and optical binding [42] extending the number of atoms included in optical binding and varying the parameters of the pump field in CARL.

A theoretical investigation of optical binding of multiple cold atoms using a coupled dipole model was performed. We found that the identifiable behaviours of optical binding in terms of the patterns of stable and meta-stable distributions were evident consistent with the application of near resonant positive and negative detuning in the pump field. We extended this work to see if stable, bound, rotationally symmetric distributions would be possible. It was successfully demonstrated in the simulations that a 13 atom bound configuration was possible showing a regular ‘breathing’ pattern in a 2D atomic lattice 3.1.

Optical manipulation of atoms and nanoparticles is an active field of research. The capacity to maintain multiple particles or atoms in a non-contact stable pattern within the pump field is subject of studies within optical manipulation, light induced trapping and assembly of nanoscale structures [61] [81] [82]

In a collaboration with the research group in Milan under Dr Nicola Piovella we took the opportunity to research with a pump field with OAM using their multimode CARL model and our fully cooperative model as detailed in 4.2.2. This follows our intention to explore cooperative effects in the interaction of cold atoms and non-uniform pump beams e.g. beams with non-uniform spatial phase profiles or partially coherent light fields. This was a natural progression from previous work from both groups concerning CARL and the emergence of superradiant modes based on linear momentum transfer. This time exploring the relationship between distribution, pump field properties, LG mode of the pump and bunching of the atoms measured in terms of optical magnetisation, M, indicating preferred modes of the scattered field due to emerging instabilities enhanced by cooperative interaction.

The multimode CARL model and the fully cooperative model described in 3.1 and 3.2.1 observed certain assumptions consistently as follows. No initial assumption about the spatial structure of the scattered field was made. Atoms in a uniform angular distribution were observed to be unstable when interacting with a far detuned optical pump field. These instabilities were superradiant in character, resulting in emerging rotation of the atomic ring and formation of atomic bunches around the ring and scattered light whose phase profile is dependent on the pump OAM azimuthal mode number and the atomic ring radius.

This resulted in the paper [44]. The preferred modes of the scattered field are found

to have a dependency on the azimuthal mode of the OAM characteristic of the pump field and the radius of the fixed cold atomic ring distribution.

There are opportunities to progress this research by developing the model further. This could include radial and even longitudinal dynamics to describe evolution and characteristics in three dimensions. There is also an opportunity of extension to include polarization effects, as for CARL in [73]. This would allow study of interactions involving exchange of both OAM and SAM. Another area for further research is substituting cold, thermal gases for quantum degenerate gases opening up possibilities for new methods for creation of vortices and persistent currents in BECs, in addition to those described in [74, 75].

Our next area of investigation involved extending the model to include the effect of pump amplitude modulation specifically the collective scattering of an amplitude modulated (AM) pump field. Our results show that pump amplitude modulation can enhance the backscattered light and increase the temperature of the atomic cloud. We postulate that these effects may be due to chaotic momentum diffusion. This effect has been demonstrated previously in the case of a phase modulated pump [77]. In the cited work there is an experimental set up similar to 1.4 where we have counter-propagating pump and probe (backscattered) fields. The slight difference from our description being that there is a slight detuning between the two fields and phase modulation is applied to the pump field. A key parameter in the theory and results of this work is the size of the modulation frequency applied to the pump in comparison to the collective recoil bandwidth.

An interesting recent field of research which has several areas of crossover with work carried out in the research presented here is the area of discrete and continuous time

crystals [83] [84]. In these cases we have a cold atomic cloud or BEC in a high finesse cavity subjected to a perpendicular pump field with a scattered probe field developing in a coupled cooperative response with the atomic distribution in this case focusing on the occupation of available momentum modes in the cavity. There is an inherent property of the interaction known as the limit cycle phase and in a similar fashion to the effects noted by phase modulation in [77] in the case of the time crystal where the pump is amplitude modulated in the region of the limit cycle phase frequencies having a stabilising effect. The evidence for this effect is the intracavity photon number showing consistent oscillation favouring particular modes consistent with a stable limit cycle phase frequency. There are clear parallels with the work carried out here and an opportunity to take the models and simulations developed to investigate in line with our approximations the extent of these responses varying the limits of density, cavity, relative fields and modulation.

References

[1] E. F. Nichols and G. F. Hul. “The Pressure Due to Radiation”. *Proceedings of the American Academy of Arts and Sciences* 38 (1903). Also published by (IOP) in The Astrophysical Journal 17(5) - June 1903 and by the American Physical Society (APS), in Physical Review 17(2):91–104, August 1903, pp. 559–599.

[2] P. Lebedew. “Untersuchungen über die Druckkräfte des Lichtes (”Studies on the pressure forces of light”)”. *Annalen der Physik* 311 (1901), pp. 433–458.

[3] A. Ashkin. “Acceleration and Trapping of Particles by Radiation Pressure”. *Physical Review Letters* 24 (1970), pp. 156–159.

[4] J. W. Ryde and R. H. Fowler. “The scattering of light by turbid media.–Part I”. *Proceedings of the Royal Society of London. Series A, Containing Papers of a Mathematical and Physical Character* 131 (1931), pp. 451–464.

[5] F. Yao et al. “Measurement of complex optical susceptibility for individual carbon nanotubes by elliptically polarized light excitation”. *Nature Communications* 9 (2018), p. 3387.

[6] W. Guerin, M. Rouabah, and R. Kaiser. “Light interacting with atomic ensembles: collective, cooperative and mesoscopic effects”. *Journal of Modern Optics* (2016), pp. 1–13.

[7] Q. Baudouin, W. Guerin, and R. Kaiser. “Cold and hot atomic vapors: a testbed for astrophysics?” *Annual Review of Cold Atoms and Molecules* 2 (2014), pp. 251–311.

[8] J. Strutt. “XXXVI. On the light from the sky, its polarization and colour”. *The London, Edinburgh, and Dublin Philosophical Magazine and Journal of Science* 41 (1871), pp. 274–279.

[9] G. Mie. “Beiträge zur Optik trüber Medien, speziell kolloidaler Metallösungen”. *Annalen der Physik* 25 (1908), pp. 377–445.

[10] G. Asimellis. *Geometrical Optics*. Lectures in optics. SPIE Press, 2020.

[11] A. Hooker, C. H. Greene, and W. Clark. “Classical examination of the Stark effect in hydrogen”. *Phys. Rev. A* 55 (6 1997), pp. 4609–4612.

[12] C. Adams and E. Riis. “Laser cooling and trapping of neutral atoms”. *Progress in Quantum Electronics* 21 (1997), pp. 1–79.

[13] C. Foot. *Atomic physics*. Oxford University Press, USA, 2005.

[14] G. Parisi. “Brownian motion”. *Nature* 433 (2005), pp. 221–221.

[15] J. Buck and E. Buck. “Mechanism of Rhythmic Synchronous Flashing of Fireflies”. *Science* 159 (1968), pp. 1319–1327.

[16] J. Javanainen and J. Ruostekoski. “Light propagation beyond the mean-field theory of standard optics”. *Optics Express* 24 (2016), pp. 993–1001.

[17] M. O. Araujo et al. “Superradiance in a Large and Dilute Cloud of Cold Atoms in the Linear-Optics Regime”. *Physical Review Letters* 117 (7 2016), pp. 1–6.

[18] R. Bonifacio and L. A. Lugiato. “Cooperative radiation processes in two-level systems: Superfluorescence”. *Physical Review A* 11 (1975), pp. 1507–1521.

[19] M. Schuurmans. “Superfluorescence and amplified spontaneous emission in an inhomogeneously broadened medium”. *Optics Communications* 34 (1980), pp. 185–189.

[20] W. Guerin, M. O. Araújo, and R. Kaiser. “Subradiance in a Large Cloud of Cold Atoms”. *Physical Review Letters* 116 (2016), p. 083601.

[21] S. Roof et al. “Observation of Single-Photon Superradiance and the Cooperative Lamb Shift in an Extended Sample of Cold Atoms”. *Physical Review Letters* 117 (2016).

[22] M. O. Scully. “Single Photon Subradiance: Quantum Control of Spontaneous Emission and Ultrafast Readout”. *Physical Review Letters* 115 (24 2015), pp. 1–5.

[23] R. Dicke. “Coherence in Radiation Processes”. *Physical Review* 93 (1 1953).

[24] T. Bienaime et al. “Interplay between radiation pressure force and scattered light intensity in the cooperative scattering by cold atoms”. *Journal of Modern Optics* 61 (1 2013), pp. 18–24.

[25] P. W. Courteille et al. “Modification of radiation pressure due to cooperative scattering of light”. *he European Physical Journal D* 58 (2010), pp. 69–73.

[26] M. O. Araújo, W. Guerin, and R. Kaiser. “Decay dynamics in the coupled-dipole model”. *Journal of Modern Optics* (2017), pp. 1–10.

[27] R. H. Dicke. “Coherence in Spontaneous Radiation Processes”. *Physical Reveiw* 93 (1954), pp. 99–100.

[28] R. G. DeVoe and R. G. Brewer. “Observation of Superradiant and Subradiant Spontaneous Emission of Two Trapped Ions”. *Physical Review Letters* 76 (1996), pp. 2049–2052.

[29] D. Pavolini et al. “Experimental Evidence for Subradiance”. *Physical Review Letters* 54 (17 1985), pp. 1917–1920.

[30] M. Gross and S. Haroche. “Superradiance: An essay on the theory of collective spontaneous emission”. *Physics Reports* 93 (1982), pp. 301–396.

[31] W. E. Lamb and R. C. Retherford. “Fine Structure of the Hydrogen Atom by a Microwave Method”. *Physical Review* 72 (3 1947), pp. 241–243.

[32] A. A. Svidzinsky, J. T. Chang, and M. O. Scully. “Cooperative spontaneous emission of N atoms: Many-body eigenstates, the effect of virtual lamb shift processes, and analogy with radiation of N classical oscillators”. *Physical Review A - Atomic, Molecular, and Optical Physics* 81 (5 2010), pp. 1–15.

[33] R. Bonifacio and L. D. S. Souza. “Collective atomic recoil laser (CARL) optical gain without inversion by collective atomic recoil and self-bunching of two-level atoms”. *Nuclear Instruments and Methods in Physics Research* 341 (1994), pp. 360–362.

[34] S. Inouye et al. “Superradiant Rayleigh Scattering from a Bose-Einstein Condensate”. *Science* 285 (1999), pp. 571–574.

[35] S. Slama et al. “Superradiant Rayleigh Scattering and Collective Atomic Recoil Lasing in a Ring Cavity”. *Physical Review Letters* 98 (2007).

[36] R. Ayllon et al. “Multimode collective scattering of light in free space by a cold atomic gas”. *Physical Review A* 100 (2 2019).

[37] J. T. Mendonça and R. Kaiser. “Photon Bubbles in Ultracold Matter”. *Physical Review Letters* 108 (2012), pp. 1–5.

[38] R. Giampaoli et al. “Photon bubble turbulence in cold atom gases”. *Nature Communications* 12 (2021), p. 3240.

[39] M. Sonnleitner, M. Ritsch-Marte, and H. Ritsch. “Attractive optical forces from blackbody radiation”. *Physical Review Letters* 111 (2 2013). NULL, pp. 1–5.

[40] P. Haslinger et al. “Attractive force on atoms due to blackbody radiation”. *Nature Physics* 14 (2018), pp. 257–260.

[41] L. Pruvost et al. “Expansion and cooling of a bright rubidium three-dimensional optical molasses”. *Phys. Rev. A* 61 (5 2000), p. 053408.

[42] C. E. Máximo, R. Bachelard, and R. Kaiser. “Optical binding with cold atoms”. *Physical Review A* 97 (4 2018).

[43] D. McLellan. *PhD- Thesis-2024-Code https://doi.org/10.5281/zenodo.14392649*. Version v1.0. 2024.

[44] A. T. Gisbert et al. “Superradiant atomic recoil lasing with orbital angular momentum light”. 023526 (2021), pp. 1–13.

[45] J. Chabé et al. “Coherent and incoherent multiple scattering”. *Physical Review A* 89 (2014), p. 043833.

[46] J. Weiner and F. Nunes. “301Atom-Light Forces”. *Light-Matter Interaction: Physics and Engineering at the Nanoscale, Second Edition*. Oxford University Press, 2017.

[47] M. Mansuripur. “A Tutorial on the Classical Theories of Electromagnetic Scattering and Diffraction”. *Nanophotonics* 10 (2021), pp. 315–342.

[48] T. Bienaimé et al. “Atom and photon measurement in cooperative scattering by cold atoms”. *Journal of Modern Optics* 58 (21 2011), pp. 1942–1950.

[49] N. Piovella et al. “Superradiant light scattering and grating formation in cold atomic vapours”. *Optics Communications* 187 (2001), pp. 165–170.

[50] Y. Li et al. “Elliptical polarization of near-resonant linearly polarized probe light in optically pumped alkali metal vapor”. *Scientific Reports* 7 (2017), p. 43066.

[51] D. Steck. “Rubidium 87 D Line Data” (2003).

[52] S. Jennewein et al. “Coherent Scattering of Near-Resonant Light by a Dense Microscopic Cold Atomic Cloud”. *Physical Review Letters* 116 (2016).

[53] A. Dunning et al. “Interferometric Laser Cooling of Atomic Rubidium”. *Phys. Rev. Lett.* 115 (7 2015), p. 073004.

[54] T. Bienaimé. “Effets coopératifs dans les nuages d’atomes froids”. Theses. Université Nice Sophia Antipolis, 2011.

[55] C. J. et al. “Coherent and Incoherent Multiple Scattering”. *Physical Review A* 89 (2014), p. 043833.

[56] B. Zhu et al. “Light scattering from dense cold atomic media”. *Physical Review A - Atomic, Molecular, and Optical Physics* 94 (2 2016). NULL.

[57] H. C. Plummer. “On the Problem of Distribution in Globular Star Clusters: (Plate 8.)” *Monthly Notices of the Royal Astronomical Society* 71 (1911), pp. 460–470.

[58] T. Bienaimé et al. “Cooperativity in light scattering by cold atoms”. *Fortschritte der Physik* 61 (2013), pp. 377–392.

[59] S. Chu and C. Wieman. “Laser Cooling and Trapping of Atoms”. *Journal of the Optical Society of America B* 6 (1989), pp. 2020–2022.

[60] C. Cohen-Tannoudji, J. Dupont-Roc, and G. Grynberg. *Atom-photon interactions: basic processes and applications*. Wiley-VCH, 1998.

[61] K. Dholakia and P. Zemánek. “Colloquium: Gripped by light: Optical binding”. *Reviews of Modern Physics* 82 (2010), pp. 1767–1791.

[62] M. I. Mishchenko, L. D. Travis, and A. A. Lacis. *Multiple Scattering of Light by Particles: Radiative Transfer and Coherent Backscattering*. Cambridge University Press, Cambridge, UK, 2006.

[63] A. A. Svidzinsky, X. Zhang, and M. O. Scully. “Quantum versus semiclassical description of light interaction with atomic ensembles: Revision of the Maxwell-Bloch equations and single-photon superradiance”. *Phys. Rev. A* 92 (1 2015), p. 013801.

[64] D. Braak et al. “Semi-classical and quantum Rabi models: in celebration of 80 years”. *Journal of Physics A: Mathematical and Theoretical* 49 (2016), p. 300301.

[65] R. Bachelard, N. Piovella, and P. W. Courteille. “Cooperative scattering and radiation pressure force in dense atomic clouds”. *Physical Review A* 84 (2011), p. 013821.

[66] A. T. Gisbert, N. Piovella, and R. Bachelard. “Stochastic heating and self-induced cooling in optically bound pairs of atoms”. *Physical Review A* 99 (2019), p. 013619.

[67] R. A. Beth. “Direct Detection of the Angular Momentum of Light”. *Phys. Rev.* 48 (5 1935), pp. 471–471.

[68] L. Allen et al. “Orbital angular momentum of light and the transformation of Laguerre-Gaussian laser modes”. *Phys. Rev. A* 45 (11 1992), pp. 8185–8189.

[69] S. Franke-Arnold. “Optical angular momentum and atoms”. *Philosophical Transactions of the Royal Society A: Mathematical, Physical and Engineering Sciences* 375 (2017), p. 20150435.

[70] G. Robb. “Superradiant exchange of orbital angular momentum between light and cold atoms”. *Physical Review A* 85 (2012), p. 023426.

[71] G. Robb. “Collective exchange of orbital angular momentum between cold atoms and light”. *AIP Conference Proceedings*. Vol. 1421. 1. American Institute of Physics. 2012, pp. 93–99.

[72] A. M. Yao and M. J. Padgett. “Orbital angular momentum: origins, behavior and applications”. *Advances in Optics and Photonics* 3 (2011), pp. 161–204.

[73] A. T. Gisbert and N. Piovella. “Multimode Collective Atomic Recoil Lasing in Free Space”. *Atoms* 8 (2020), p. 93.

[74] M. E. Tasgın, Ö. E. Müstecaplıoğlu, and L. You. “Creation of a vortex in a Bose-Einstein condensate by superradiant scattering”. *Physical Review A* 84 (2011).

[75] P. Das, M. E. Tasgin, and Ö. E. Müstecaplıoğlu. “Collectively induced many-vortices topology via rotatory Dicke quantum phase transition”. *New Journal of Physics* 18 (2016), p. 093022.

[76] M. Babiker, W. Power, and L. Allen. “Light-induced torque on moving atoms”. *Physical review letters* 73 (1994), p. 1239.

[77] G. R. Robb, R. T. Burgess, and W. J. Firth. “Enhancement of collective atomic recoil lasing due to pump phase modulation”. *Physical Review A - Atomic, Molecular, and Optical Physics* 78 (4 2008).

[78] R. Bonifacio et al. “Exponential gain and self-bunching in a collective atomic recoil laser”. *Physical Review A* 50 (1994), pp. 1716–1724.

[79] E. Tesio et al. “Self-organization in cold atomic gases: a synchronization perspective”. *Philosophical transactions of the royal society A* 372 (2014), p. 20140002.

[80] L. Peliti. “On the equipartition of kinetic energy in an ideal gas mixture”. *European Journal of Physics* 28 (2007), p. 249.

[81] R. W. Bowman and M. J. Padgett. “Optical trapping and binding”. *Reports on Progress in Physics* 76 (2013), p. 026401.

[82] T. Čižmár et al. “Multiple optical trapping and binding: New routes to self-assembly”. *Journal of Physics B: Atomic, Molecular and Optical Physics* 43 (2010), p. 102001.

[83] P. Kongkhambut et al. “Observation of a continuous time crystal”. *Science* 377 (2022), pp. 670–673.

[84] H. Keßler et al. “From a continuous to a discrete time crystal in a dissipative atom-cavity system”. *New Journal of Physics* 22 (2020), p. 085002.